Localised Solutions of the Parametrically Driven Ginzburg-Landau and Nonlinear Schrödinger Equations

Simon Cross

A thesis submitted in fulfillment of the requirements of the degree of Master of Science at the University of Cape Town

Abstract

This thesis deals with localised solutions of the parametrically driven Ginzburg-Landau equation and its nonlinear Schrödinger limit. We begin with a detailed analysis of the Faraday Resonance experiment, in which the driven complex Ginzburg-Landau equation (CGLE) arises, and an examination of how the CGLE appears as the amplitude equation for the modes excited near a Hopf bifurcation. We then move on to investigate how known analytic stationary solutions of the damped-driven nonlinear Schrödinger (NLS) equation may be numerically continued to solutions of the parametrically driven CGLE. First we examine two pulse solutions. After checking analytically that these persist when the diffusion is turned on, an adiabatic analysis (valid for small diffusivity) of the pulses is performed. The pulses are then continued numerically and the stability of the resulting solutions is examined using a numerical spectral method. In the diffusion-free case, the pulse solutions merge at a saddle-node bifurcation when the driving strength drops to a critical value. This phenomenon persists when the diffusivity is turned on and we map out the region of existence of the pulses on the two-dimensional (driving strength vs diffusion) parameter plane. When the diffusivity is non-zero, the region of existence of the stable pulse is also found to be bounded above: as the driving strength rises to a critical value, the pulse broadens eventually forming a bound state of two widely separated fronts. The broadening occurs by the addition of new humps to the centre of the pulse. For parameter values close to the point where the bound fronts form we found many coexisting multistable pulses, each having a different number of humps. We then separate out one of the bound fronts and continue it further, obtaining solutions over both flat and oscillatory backgrounds. The stability of these solutions is also analysed. Next, a new stationary analytic kink solution of the parametrically driven undamped NLS equation is presented. We show that this kink solution is not continuable to non-zero damping but may persist if the damping and diffusion are allowed to vary simultaneously. We continue the kink in these two parameters and again find solutions over oscillatory backgrounds. These backgrounds are studied analytically for small values of the damping and diffusion. Finally, the analytic kink is continued in velocity, producing a uniformly translating solution of the driven undamped nonlinear Schrödinger equation.

Acknowledgements

After submitting one of the later drafts of this thesis to my supervisor, he advised me not to thank anyone in order to not to waste time writing acknowledgements. Since the thesis seems mostly complete now, I'm going to write some acknowledgements anyway.

Firstly, thank you to my supervisor, Igor Barashenkov, for providing me with grantholder funding, for suggesting and helping arrange the trip to the Dynamics Days 2001 conference in Dresden, for explaining countless pieces of mathematics, for forcing me to keep working when I wanted to give up, and, above all, having a good sense of humour. I also want to congratulate my supervisor and his wife, Nora, on the arrival of their new baby daughter, Mia-Lucia.

Which brings me to the second thank you. Thank you, Nora, for helping me during my first tentative steps with AUTO.

The next thank you is to all those who have provided me with funding in one way or another. This includes Prof. I.V. Barashenkov, the NRF, the Harry Crossley Foundation, the Mathematics and Applied Mathematics Department of UCT and my parents.

Thank you again to my parents for helping support me even though at times I did everything but work on my thesis and despite not really understanding what I was working on.

The penultimate thank you goes to the Jeff and Rory. Thank you for being wonderful office mates, for many late night discussions and for generally making office life much more entertaining than it might otherwise have been.

Last, but by no means least, thank you to Adrianna. Thank you for all the times you've brought iced-tea to my office, or stayed up on campus so that I could work late. Thank you for helping me painstakingly edit my poster in The GIMP the night before leaving for Dresden. Thank you for putting up with my self-doubt and lack of confidence. Most of all, thank you for existing.

Contents

Chapter 1

Introduction

1.1 Overview

The complex Ginzburg-Landau and nonlinear Schrödinger (NLS) equations both arise in numerous applications. Both are also of great mathematical interest - the complex Ginzburg-Landau as the normal form of a field near a Hopf bifurcation and the NLS as a completely-integrable, soliton-bearing equation.

The cubic complex Ginzburg-Landau equation (CGLE) has the form

$$\psi_t + c_1\psi_{xx} + c_2|\psi|^2\psi + c_3\psi = 0\,. \tag{1.1}$$

The coefficients c_1, c_2 and c_3 may be complex. The case of real coefficients is usually referred to as the real Ginzburg-Landau equation. The real Ginzburg-Landau equation derives its name from the theory of superconductors developed by Ginzburg and Landau [1] in which it arises when there is no applied magnetic field. The equation with real coefficients also occurs in the context of particle physics as a stationary limit of the Abelian-Higgs model pioneered by Nielsen and Olesen [2]. The dynamics of the real Ginzburg-Landau equation are purely relaxational owing to the existence of a potential for the system.

The opposite case, when the coefficients c_1, c_2 and c_3 are all purely imaginary, is the nonlinear Schrödinger equation. This equation was shown to be completely integrable when Zakharov and Shabat [3] applied the inverse scattering method to it in 1971. The method had been developed three years earlier by Lax [4] and was an extension of that employed by Gardner, Greene, Kruskal and Miura [5] to solve the Korteweg-deVries equation in 1967. The NLS equation also has a Hamiltonian structure and may be derived from a principle of least action.

In chapter 3 (chapter 2 covers the Faraday Resonance experiment, a system in which the driven CGLE arises) we derive the CGLE as the amplitude equation for a real vector field. Many physical systems may be described by a real vector field which is a function of space and time variables. It is often the case that this field is invariant under translations in space and time. That is, the physical

system described by the field remains unchanged if we change the origin of our space or time axes. It is at the Hopf bifurcation of such a field that the complex Ginzburg-Landau appears as the amplitude equation for the excited modes.

The addition of time-periodic forcing to the system breaks the invariance of the physical system under time translations. The effect of a forcing with magnitude h on the amplitude equation is to add the term $h\overline{\psi}^{s-1}$ to the right-hand side of (1.1) giving

$$\psi_t - c_1\psi_{xx} + c_2|\psi|^2\psi + c_3\psi = h\overline{\psi}^{s-1} \quad . \tag{1.2}$$

We call (1.2) the (parametrically) driven CGLE. The sign of h is arbitrary and, for definiteness, we consider it to be positive unless otherwise specified.

The constant s is an integer which depends on the ratio between the frequency of the forcing, ω_f, and the frequency of the mode excited at the Hopf bifurcation, ω_0. If $\frac{\omega_0}{\omega_f} = \frac{m}{n}$ where n and m are integers with $\gcd(\mathrm{m},\mathrm{n}) = 1$, then $s = n$. If $\frac{\omega_0}{\omega_f}$ cannot be expressed as the ratio of two integers, then any two integers with $\gcd(\mathrm{m},\mathrm{n}) = 1$ which yield a ratio close to $\frac{\omega_0}{\omega_f}$ may be chosen but an additional term proportional to $\frac{\omega_0}{\omega_f} - \frac{n}{m}$ must be added to the amplitude equation. The case where $\omega_f = 2\omega_0$ and $s = 2$ is easily accessible experimentally and the most tractable theoretically. For this reason it is the case we focus on in this work.

The first three chapters review known results while in the latter half of this thesis, Chapters 4 and 5, we find localised solutions of the driven CGLE by continuing known analytic solutions of the damped-driven NLS equation. The driving term we consider is $h\overline{\psi}$ which is the ($s = 2$)-case of equation (1.2) that was mentioned in the previous paragraph.

The process of continuation we employ starts with a known solution of the damped-driven NLS equation. In the NLS limit, some of the coefficients of the driven CGLE are zero. (Here we count the real and imaginary parts of the coefficients c_1, c_2 and c_3 in equation (1.2) as separate coeffients.) If we modify one (or more) of these zero-valued coefficients and give it a small non-zero value, then the original solution to the damped-driven NLS equation will be an approximate solution of the equation with the modified coefficients. This approximate solution may then be used as an initial guess for attempting to find an exact solution to the equation with modified coefficients. We use an iterative numerical method to repeatedly modify the approximate solution so that it more and more closely approximates the exact solution.

It is possible that in some cases no such nearby exact solution will exist. In order to avoid this case we introduce the concept of continuability. A solution $\psi(\vec{x}, \vec{\mu} = \vec{\mu}_0)$, which depends on a set of parameters $\vec{\mu}$ from the differential equation, is said to be continuable in $\vec{\mu}$ if there exists a solution $\psi(\vec{x}, \vec{\mu})$ for all $\vec{\mu}$ in some neighbourhood $|\vec{\mu} - \vec{\mu}_0| < \epsilon$ of $\vec{\mu}_0$ and $\psi(\vec{x}, \vec{\mu})$ is continuous in $\vec{\mu}$ at $\vec{\mu} = \vec{\mu}_0$. Provided the solution to the unmodified equation from which we start is continuable, we will be able locate a nearby exact solution if the changes in the parameters $\vec{\mu}$ are small enough.

In our work, we check analytically the continuability of starting solutions which can be written in closed form. The actual continuation of the starting solutions is performed numerically using the software AUTO97 [6].

Chapter 4 focuses on stationary pulse solutions of the driven complex Ginzburg-Landau equation. We discover that stationary pulse solutions of the damped-driven NLS equation may be continued to stationary pulse solutions of the CGLE. After further continuation these pulses are transformed into a solution consisting of a bound state of two kinks. The stability of the solutions which result from the continuation is analysed numerically using the Fourier method. In addition, the behaviour of the solutions found by continuation is analysed using an adiabatic approximation which is valid when the parameters of the driven complex Ginburg-Landau equation are close to those of its damped-driven NLS limit.

Chapter 5 deals with front solutions of the driven complex Ginzburg-Landau and starts with the finding of an analytic kink solution to the driven undamped NLS equation. This analytic kink solution is then continued into the driven complex Ginzburg-Landau parameter regime. The analytic kink is also continued to a kink solution which moves with constant non-zero velocity. This moving solution of the driven undamped NLS is compared to similar moving solutions found in [7]. The final part of Chapter 5 further examines the solution consisting of two kinks which was found in Chapter 4. One of the two kinks is isolated and continued further. The stability of the numerical kinks resulting from this continuation is analysed using the same procedure used in Chapter 4.

Of the many experiments in which the driven CGLE arises, the one with the longest history is assuredly the Faraday Resonance experiment which was first reported on by Michael Faraday in 1831 [8]. The historical background of this experiment and its surrounding theory are discussed in the chapter 2. Some other applications of the driven CGLE are discussed later in this introduction. The section on the Faraday Resonance experiment is separated out into its own chapter because of its length.

By way of ending off this first section of the introduction we mention two works which summarise much of the research done on localised solutions of the (undriven) CGLE. One is the paper published by van Saarloos and Hohenberg [9] in 1992 and the other is the chapter *Solitons of the CGLE* by Akhmediev and Ankiewicz which was published as part of the book *Spatial Solitons* [10] in 2001. The paper by van Saarloos and Hohenberg focuses on coherent structures (localised defects in regular spatial patterns). It examines both the existence of coherent structures and their stability and presents important results on front selection (the problem of which one of a number of co-existing front solutions will manifest itself). The chapter by Akhmediev and Ankiewicz deals with solitary wave solutions (localised solutions which tend to zero as $|x|$ tends to infinity) of the CGLE. The form of the CGLE they use is that common in nonlinear optics (obtained by multiplying equation (1.1) by i) and is the natural one to use when

examining the NLS limit of the complex Ginzburg-Landau. As such, it is the form we use for our work in chapters 4 and 5. Together the two references provide a good background to our research. The standard review paper on *non-localised* solutions (and specifically pattern formation) in the CGLE is the one by Cross and Hohenberg [11].

The remainder of the introduction presents a survey of some of the literature on the complex Ginzburg-Landau and related equations and is divided into three broad sections:

- Firstly, our approach to finding solutions of the driven CGLE is motivated by considering the results of earlier work on the damped-driven NLS equation.
- Secondly, we discuss some of the applications in which the Complex Ginzburg-Landau equation arises. The applications we focus on are optical parametric oscillators and ferromagnets. The description of the Faraday Resonance experiment is left for Chapter 2.
- Thirdly, we examine some interesting theoretical aspects of the Complex Ginbzburg-Landau equation. This begins with a look at the variational limit of the Complex Ginzburg-Landau which, as explained earlier, is in some sense the opposite limit to the one in which the CGLE becomes the NLS equation. We then discuss spatial forcing which has effects akin to the parametric forcing we consider in this work. That is followed by a look at composite pulses which are similar to the pulses we find by continuation in Chapter 4. Finally we mention some known solutions of the zero driving limit of the complex Ginzburg-Landay equation we study in Chapter 4 which could be used as the basis for further continuations.

1.2 Motivation for our approach

Our approach in chapters 4 and 5 is to take known solutions to the damped driven nonlinear Schrödinger limit of (1.2) and use them as starting points for generating solutions of the driven CGLE. Although our approach uses numerical continuation, it is motivated by the success of the damped-driven NLS equation at explaining the existence of solitary waves in physical systems.

The reasoning is as follows: suppose that a physical system is described by the driven CGLE. It might be possible to arrange the experimental setup (by altering physical parameters) so that the system is close to its damped-driven NLS limit. However, it is unlikely that the system can be made to assume its damped-driven NLS limit exactly. If solutions of the damped-driven NLS equation are found to successfully model observed features of a system of this type then similar solutions should be found in the driven CGLE (near its NLS limit) since it more fully describes the physical sytem. Such solutions of the NLS equation are likely

to be continuable and thus may be used as starting points for finding solutions of the driven CGLE by continuation, as we do in chapters 4 and 5.

In one modelling success of this kind, Elphick and Meron [12] performed a theoretical study of localised structures in a narrow channel Faraday resonance experiment. Localised structures (specifically non-propagating, solitary waves) had been observed previously in experiments by Wu, Keolian and Rudnick [13] and earlier theoretical work had been performed by Larraza and Putterman [14] and Miles [15]. As we shall see in Chapters 2 and 3, the Faraday resonance experiment may be described by the driven CGLE.

In all three theoretical works mentioned [12, 14, 15], the known solutions of the nonlinear Schrödinger equation were exploited to find explanations for the experimentally observed solitary waves. Of particular relevance to my study is the mention in [12] that it is the time reversal symmetry ($t \to -t$) of the initial hydrodynamic equations which implies that the coefficients in the derived amplitude equation (see equation 1.3) are real. However, if the hydrodynamic system is dissipative (which it is in this case) then the time reversal symmetry of the hydrodynamic system is broken, allowing the coefficients in the amplitude equation to have small imaginary parts.

Elphick and Meron [12] derive the amplitude equation

$$iA_t = -i\mu A - \delta\sigma\overline{A}e^{i\nu t} + \alpha A_{xx} + \beta|A|^2 A\,, \tag{1.3}$$

for excited modes in a Faraday resonance experiment. Here σ, α and β are all real functions of the transverse wave number, k_y, of the mode being excited in the fluid. The transverse wave number $k_y = \frac{n\pi}{b}$, where b is the width of the rectangular fluid container. Equation (1.3) is a damped-driven NLS equation. However, the damping term ($-i\mu A$) arises as the result of dissipation in the full hydrodynamic system. Thus the time reversal symmetry of the hydrodynamic equations is already broken and the coefficients σ, α and β in the amplitude equation (1.3) may, in principle, be complex. This would make (1.3) the driven CGLE.

In [12], Elphick and Meron specifically examine solutions of the damped unforced nonlinear Schrödinger equation (both pulses and kinks) and extend these to solutions of the damped parametrically forced nonlinear Schrödinger equation. They conclude that large amplitude solitary wave solutions exist only when the bifurcation of the flat solution at the onset of the surface waves is subcritical. In the subcritical case the newly-formed uniform surface wave solutions (of the hydrodynamic system) are unstable near the bifurcation point and the quiescent state (the unexcited state of the hydrodynamic system) is stable where the surface wave solutions exist. In the supercritical case the newly-formed uniform surface wave solutions (of the hydrodynamic system) are stable near the bifurcation point but the quiescent state is unstable where the surface wave solutions exist. As a result we devote much of our work in chapters 4 and 5 to the case where the bifurcation is subcritical.

Elphick and Meron [12] also discuss the topologically stable kink solution to the damped driven nonlinear Schrödinger equation. This kink solution connects two regions whose phases of oscillation differ by π. Such topologically stable kinks are possible since the parametric driving term breaks the phase invariance ($A \rightarrow Ae^{i\phi}$) of the nonlinear Schrödinger equation. Kink solutions may exist in the undriven NLS equation but they are at best marginally stable because of the phase invariance of the equation.

In fact, the effects of the small imaginary parts of the coefficients α and β (see equation 1.3) in the amplitude equation have been observed experimentally and theoretically studied by Douady [16].

1.3 Applications

The parametrically driven CGLE arises in the description of a variety of physical systems. In this section we will discuss two such applications, namely optical parametric oscillators and ferromagnets. As mentioned previously, the Faraday resonance experiment will be left until chapter 2. The chief reason for leaving the section on the Faraday resonance experiment out of the introduction is its length. However, if the reader wishes she may read chapter 2 as if it were part of this section. Other applications (which we will just mention) in which the CGLE arises include optical transmission lines [17], plane Poiseuille flow in fluid dynamics [18] and convection in binary fluid mixtures [19].

The Faraday resonance experiment was selected as an example because of its long history and the simplicity of the experimental apparatus. It is often easier to intuitively grasp the behaviour of a commonly encountered substance such as water than to come to terms with the behaviour of objects only encountered in more specialised settings.

Optical parametric oscillators were chosen as the second example because they are currently the subject of much theoretical and practical interest. On the practical side optical parametric oscillators provide broadly tuneable optical sources and are useful (for example) in high resolution spectroscopy. Optical parametric oscillators are available for sale commercially from companies like EKSPLA [20]. On the theoretical front work has already started [21] on analysing the 3-dimensional structure of the electromagnetic fields within an optical parametric oscillator, in addition to the work mentioned later on the amplitude equations for the fields emerging from the optical parametric oscillator.

The final application, ferromagnets, was chosen in order to make some comparisons between parametric forcing (which we consider) and direct forcing, and to examine the interesting behaviour of domain walls as one moves away from the variational limit of the parametrically driven complex Ginzburg Landau into the non-variational regime. The material on the behaviour of domain walls near the variational limit is in section 1.4.1 which immediately follows the section on

ferromagnets, section 1.3.2.

1.3.1 Optical parametric oscillators

The parametrically driven CGLE arises in the context of optical parametric oscillators (OPO's). Longhi and Geraci in [22] and [23] showed that the pattern formation dynamics of OPO's could be reduced to the complex Ginzburg-Landau equation. Trillo, Haelterman and Sheppard [24] predicted, and then found numerically, stable solitary wave solutions in the parameter range of the OPO's where the non-trivial homogenous solutions are stable.

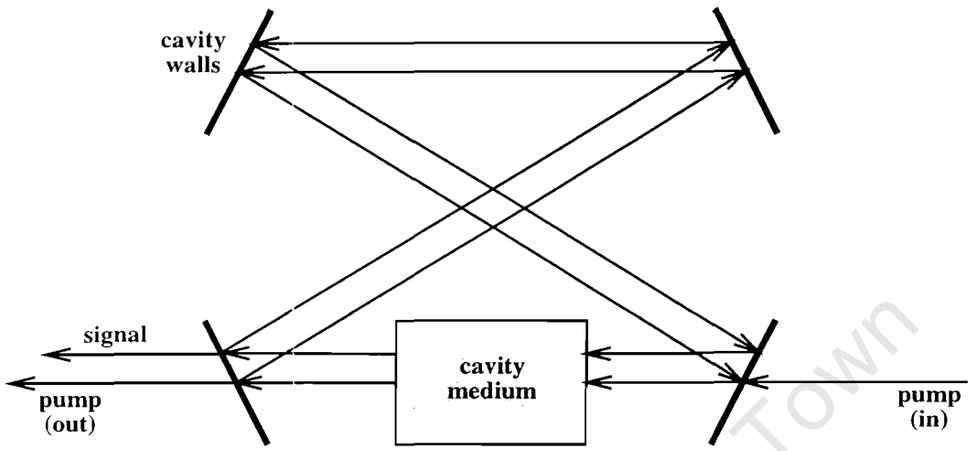

Figure 1.1: *A doubly resonant OPO.*

An OPO, as shown if Fig. 1.1, consists of an optical cavity, a nonlinear optical cavity medium and a laser (the pump) [25]. Photons emitted by the pump laser enter the optical cavity and are trapped there. The length of time for which the photons remain in the cavity (the cavity photon lifetime) provides a natural timescale for the system. While within the cavity, the photons pass through the nonlinear optical medium, causing the medium to emit a response, called the signal. Some of the incoming pump field passes straight through the system. This part of the emitted field is known as the idler.

The cavity lifetime of a photon is frequency dependent. When both the pump and signal fields are close to local maxima of the cavity lifetime (as a function of photon frequency) then the OPO is said to be double resonant. If only the signal field is close to such a maximum, then the OPO is said to be singly resonant.

Trillo, Haelterman and Sheppard [24] begin with the coupled equations for the signal $u(\vec{x},t)$ and pump $v(\vec{x},t)$ field envelopes of a doubly resonant OPO where the cavity medium has $\chi^{(2)}$ (quadratic) optical nonlinearities:

$$u_t = \frac{i}{2}\nabla_\perp^2 u + v\overline{u} - (1+i\Delta_1)u\,,$$

$$v_t = \frac{ip}{2}\nabla_\perp^2 v - u^2 - (\alpha + i\Delta_2)v + S\,. \tag{1.4}$$

Note that the spatial coordinates $\vec{x} = (x, y)$ are the coordinates perpendicular to the pump and signal beams, so the system has two spatial and one temporal dimension. The field envelopes, u and v, are complex. The parameter S represents plane-wave excitation, α the ratio of the pump loss rate to the signal loss rate and p the ratio of k_1 and k_2 which are the wave numbers of the resonant pump and signal modes respectively. Of importance here are the cavity detuning parameters Δ_1 and Δ_2, which quantify how far from resonance the pump and signal fields are. Assuming that Δ_2 is large (i.e. the pump field is far from resonance and the OPO is singly resonant) and that the pump envelope v changes only slowly in space and time, we can solve the second equation of (1.4) to obtain an adiabatic approximation for v:

$$v \approx \frac{(S - u^2)}{i\Delta_2}\,. \tag{1.5}$$

Substituting this approximation into the first equation of (1.4) yields a damped driven nonlinear Schrödinger equation for the signal field envelope, u:

$$u_t = \frac{i}{2}\nabla_\perp^2 u + \frac{i}{\Delta_2}|u|^2 u - (1 + i\Delta_1)u - i\frac{S}{\Delta_2}\overline{u}\,. \tag{1.6}$$

Equation (1.6) also occurs in the context of Kerr-type nonlinear dispersive cavities with parametric driving [26]. It has the homogenous stationary solutions

$$u_s = \pm\left[S + \frac{\Delta_2}{S}(i - \Delta_1)\left(i\Delta_2 \pm \sqrt{S^2 - \Delta_2^2}\right)\right]^{1/2}. \tag{1.7}$$

For certain ranges of Δ_1 and Δ_2 (for example, $\Delta_1 = \Delta_2 = 2$) the non-trivial homogenous solutions exist simulatenously with the stable trivial background solution. This is the parameter region where the system is bistable. In the bistable region one expects the existence of stable kink solutions connecting the non-trivial homogenous backgrounds and indeed the system admits the solution

$$u = A\tanh\left(\frac{x}{x_0}\right)e^{i\phi}\,, \tag{1.8}$$

where $A = \left[\Delta_1\Delta_2 \pm (S^2 - \Delta_2^2)^{1/2}\right]^{1/2}$, $x_0 = \frac{(-\Delta_2)^{1/2}}{A}$ and $\phi = -\frac{1}{2}\arcsin\left(\frac{\Delta_2}{S}\right)$.

This solution connects u_+ and u_- which differ by a phase of π. The solution (1.8) depends only on x and represents a one-dimensional topological defect on the xy-plane with the phase differing by π across the defect. Trillo, Haelterman and Sheppard showed in [24] that these defects develop spontaneously from white noise in numerical simulations provided the intensity of the noise is high enough.

In self-focusing Kerr media stripe solutions similar to (1.8) break up as they are unstable against the formation of vortices [27]. The breaking of the rotational phase invariance by the parametric driving term $-i\frac{S}{\Delta_2}\overline{u}$ in (1.6) means that such vortices cannot form in OPOs. As a result, the stripe solution (1.8) is stable.

1.3.2 Ferromagnets

Ferromagnets are crystals which undergo spontaneous large-scale magnetic polarization. However, the large-scale magnetic polarization ceases at a temperature called the Curie point. Above this temperature (which varies from substance to substance) the spontaneous magnetization does not occur. In uniaxial crystals (these are special hexagonal or tetragonal crystals which have one principal axis of symmetry, sometimes called the optical axis) the magnetic energy is either a minimum or a maximum when the magnetization vector $\vec{M}$ points along the z-axis (the axis of symmetry). If the energy is a minimum then a single direction of the magnetization (namely, parallel or anti-parallel to the z-axis) is preferred. The ferromagnet is then said to be easy-axis [28].

The equations for the magnetization of an easy-axis ferromagnet near the Curie point may be reduced to

$$A_t = A - |A|^2 A + \gamma \overline{A} + A_{xx} \,, \tag{1.9}$$

where $A = M_z + iM_y$ and M_z and M_y are the z and y components of the magnetization, $\vec{M}$. The direction of $\vec{M}$ for which the anistropy energy is least is the direction of easy magnetisation and is aligned with the z-axis for an easy-axis ferromagnet. The problem is made one-dimensional by assuming that $\vec{M}$ varies only with x and is constant in y and z. M_x, the x component of $\vec{M}$, must then be constant. If M_x were not constant then $\vec{\nabla} \cdot \vec{M} = \frac{\partial M_x}{\partial x}$ (since $\vec{M}$ is constant in y and z) would be non-zero. As the divergence of the magnetic induction, $\vec{\nabla} \cdot \vec{B}$, is zero the divergence of the net magnetic field, $\vec{\nabla} \cdot \vec{H} = \vec{\nabla} \cdot \vec{B} - 4\pi \vec{\nabla} \cdot \vec{M}$ would have to be non-zero. Thus the net magnetic field $\vec{H}$ would itself be non-zero. This would increase the energy of the system, making a non-constant M_x energetically unfavourable. So M_x must be a constant. In addition, this constant must be zero since $\vec{M}$ is assumed to be parallel or anti-parallel to the z-axis when $|x| \to \infty$ [28].

Note that (1.9) contains a parametric driving term $\gamma \overline{A}$. This term is not a result of any external forcing of the system, but rather arises from the microscopic anisotropy of the magnetic properties of the ferromagnet. The anisotropy may be considered a form of spatial forcing and stems from relativistic interactions between the individual atoms of the ferromagnet. Spatial forcing is discussed later in section 1.4.2. In addition, the cubic nonlinearity in (1.9) is defocusing so that the bifurcation at the Curie point is supercritical. Consequently kink solutions (domain walls) exist but not solitary wave solutions on a zero background (here the zero background corresponds to an absence of magnetization).

Coullet, Lega and Pomeau [29] examine the behaviour of Bloch walls under the influence of a rotating magnetic field. The rotating external magnetic field directly forces the magnetization of the ferromagnet with the effect of adding a driving constant h to the right-hand side of equation (1.9) and not a term of the form $h\overline{A}$ as would be the case for periodic forcing. Adding the driving constant to

(1.9) gives

$$A_t = A - |A|^2 A + \gamma \overline{A} + A_{xx} + h \,. \tag{1.10}$$

A domain wall joins regions of a ferromagnet in which the magnetization takes on two different stable values. The Bloch wall is a type of domain wall where the magnetization vector rotates as we move from the one region of magnetization to the other. The magnitude of the magnetization does not become zero. See Figure 1.2. Another type of domain wall is the Ising wall, where the magnetization does become zero somewhere between the two regions.

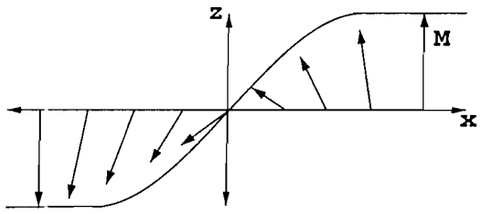

Figure 1.2: *A graph of the M_z, the z component of $\vec{M}$, along a Bloch Wall. The arrows depict the magnetization vector $\vec{M}$. In the right-hand domain the magnetization $\vec{M}$ is parallel to the z-axis. As we move to the left the magnetization rotates in the yz-plane. Once we reach the left-hand domain $\vec{M}$ has rotated π radians and has become anti-parallel to the z-axis. The x component of $\vec{M}$ remains zero throughout.*

The rotating magnetic field considered in [29] lies in the same plane as the magnetization vector in the Bloch wall. One can imagine the Bloch wall being forced to move as the magnetization attempts to both follow the rotation of the applied magnetic field and to maintain the spatial structure of the Bloch wall.

Taking the complex conjugate of A maps $A \to M_z - iM_y$. This is the equivalent of taking the mirror image of the physical system ($x \to -x$). The two types of Bloch walls, both of which join regions of non-trivial magnetization, are complex conjugates of one another:

$$A_\pm = X(x) \pm iY(x) \,. \tag{1.11}$$

Thus they are mirror images of each other in the physical system and are referred to as the left and right-handed Bloch walls. Coullet, Lega and Pomeau find that the action of the direct driving is to impart a non-zero velocity to the Bloch walls, as expected. Left-handed and right-handed Bloch walls have equal speeds but move in opposite directions. Reversing the direction of rotation of the driving magnetic field reverses the velocities of both Bloch walls.

1.4 Theoretical aspects of the CGLE

The four subsections of this discussion of theoretical aspects each deal with a separate topic.

The first is the behaviour of both the undriven and parametrically driven CGLEs near their respective variational limits. In the parametrically driven case, particular attention is paved to the transition from Ising to Bloch walls. Although these structures derive their names from ferromagnets, equivalent structures are found in other physical systems described by the parametrically driven comlex Ginzburg-Landau equation.

The second is the effects of spatial forcing. As mentioned in section 1.3.2, spatial forcing arising from microscopic anisotropy is the origin of the parametric driving term in equation (1.9) which describes the magnetization of easy-axis ferromagnets.

Following the section on spatial forcing is one describing known composite pulse solutions which are similar in appearance to those we find later in Chapter 4. These known composite pulses are solutions of the *undriven* quintic CGLE.

We end off with a look at known soliton solutions of a special case of the *undriven* CGLE. These soliton solutions are not the ones we use for starting our continuations but they could be used as the starting points for further studies similar to those performed in Chapter 4. The localised structures we use to begin our continuations are introduced at the start of Chapters 4 and 5 and are all solutions to limits of the CGLE which have non-zero driving.

1.4.1 The variational limit of the complex Ginzburg-Landau equation

The undriven CGLE

The CGLE

$$W_t = \mu W + \alpha W_{xx} + \beta |W|^2 W \tag{1.12}$$

is a gradient (variational) system when μ, α and β are real. The variational torm of equation (1.12) (when μ, α and β are real) is

$$W_t = -\frac{\delta \mathcal{L}}{\delta \overline{W}} = \frac{\partial V}{\partial (|W|^2)} W + \alpha \frac{\partial^2 W}{\partial x^2} \tag{1.13}$$

where $\mathcal{L}$ is the Liapounov functional,

$$\mathcal{L}\{W\} = \int_0^L \left[\alpha \left| \frac{\partial W}{\partial x} \right|^2 - V(|W|^2) \right] \mathrm{d}x \,. \tag{1.14}$$

Here V is the potential energy density,

$$V(|W|^2) = \mu |W|^2 + \frac{1}{2} \beta |W|^4 \,. \tag{1.15}$$

The coefficients must be real so that the potential energy is a real function. Note that V is a function of $|W|^2$ only. When $|W|^2$ minimises V, so that $\frac{\partial V}{\partial (|W|^2)} =$

0. the variational equation (1.13) reduces to the heat equation which has purely relaxational dynamics.

When the CGLE can be cast in the above variational form, stable stationary pulse solutions do not exist and stable stationary kink solutions exist only on non-generic regions in the parameter space (that is, regions whose dimension is less than the dimension of the full parameter space), for the reasons given in the two paragraphs below.

Kink solutions connect distinct homogenous backgrounds. Since the equation is variational and the potential energy V (given by (1.15)) depends only on $|W|^2$, the background with the lower potential energy is expected to invade the background with the higher potential energy [30]. Thus stationary kinks are only likely to be stable at special parameter values for which the energies of the two homogeneous states are equal.

Pulses are not stable because of the interactions between the pulse sides. The two halves of the pulse either repel each other (causing the pulse to broaden and split into two travelling kinks) or attract each other (so that the pulse shrinks).

Thual and Fauve [31] examined the changes in the dynamics which occur when the variational form does not exist, that is, when one or both of the coefficients α and β have a small nonzero imaginary part. The constant μ is kept real as it is the bifurcation parameter (i.e. it is a measure of the distance of system from its Hopf bifurcation). The equation that Thual and Fauve studied was actually the quintic complex Ginzburg-Landau which has an extra term $\gamma|W|^4W$ added to the right-hand side of equation (1.12) and, as a result, an extra $\frac{1}{3}\gamma|W|^6$ term in the potential energy (1.15). This additional term was necessary since they considered the case where μ and $\mathrm{Re}\,\beta$ are positive. Positive μ results in the growth of small disturbances (the opposite of damping) which can only curbed by the cubic nonlinearity if $\mathrm{Re}\,\beta$ is negative. Since they had assumed $\mathrm{Re}\,\beta > 0$, the quintic nonlinearity was added with $\mathrm{Re}\,\gamma < 0$ in order to ensure that this growth would eventually be halted and that stable solutions could exist.

They show that when β and γ have non-zero imaginary parts the spatial frequency of the travelling wave solutions of equation (1.12) is related to the amplitude of the travelling wave. This sets up a feedback mechanism which adjusts the effective value of μ keeping it close to a critical value μ_p over a range of values of μ. μ_p is the value of μ for which the trivial and non-trivial homogenous stationary backgrounds have the same potential energy, V. Here the potential energy is calculated ignoring the imaginary parts of β and γ.

Thual and Fauve also showed (using numerical methods) that this mechanism can stabilise two-dimensional pulses which evolve according to equation (1.12) with W_{xx} replaced by $\nabla^2 W$, the two dimensional Laplacian of W.

Other mechanisms for the stabilisations of kinks in non-variational systems have been suggested by Pomeau [30]. These mechanisms rely on the effects of the locking of the wave envelope describing the kink to structures in the underlying

physical system. For example, in a hydrodynamic system, the amplitude equation kinks might attached themselves to hexagonal patterns formed on the fluid surface.

The parametrically driven CGLE

Above we have seen that for the *undriven* complex Ginzburg-Landau stable stationary kinks and pulses are uncommon in the variational limit of the equation. We will now see that the situation is markedly different for the variational limit of the *parametrically driven* CGLE. The forcing term, which is proportional to $\overline{W}$, requires that we add a term proportional to $\frac{1}{2}(W^2+\overline{W}^2)$ to the potential energy of the variational system in the parametrically driven case. The result is that V can no longer be considered a function of one variable ($|W|^2$) and must be consider a function of both W and its complex conjugate, $\overline{W}$. Also the representation

$$W_t = \frac{\partial V}{\partial(|W|^2)}W + \alpha\frac{\partial^2 W}{\partial x^2} \tag{1.16}$$

is no longer valid and must be replaced with

$$W_t = \frac{\partial V}{\partial \overline{W}} + \alpha\frac{\partial^2 W}{\partial x^2}\,. \tag{1.17}$$

The minima and maxima of V are no longer the only values of W for which the variational equation (1.17) becomes relaxational since $\frac{\partial V}{\partial W}$ may be non-zero.

As stated in the previous section on ferromagnets, the parametrically driven CGLE with defocusing nonlinearity possesses Ising and Bloch wall solutions. In constrast to this, the equations we study in chapters 4 and 5 have focusing nonlinearity and do not possess Ising or Bloch wall solutions. Ising walls can become unstable and undergo a pitchfork bifurcation to Bloch wall solutions. In [32] Skryabin *et al* examine the nature of the transition from Ising to Bloch wall solutions and compare the variational and non-variational cases. They show that although the point of the Ising to Bloch transition (in the parameter space of the coefficients) varies smoothly as one moves away from the variational limit, the excitation mode responsible for the Ising wall instability undergoes a singular rotation of π radians.

The stability of the Ising wall is determined by an eigenvalue problem

$$\hat{L}\zeta = \lambda\zeta \tag{1.18}$$

and the wall is unstable if the 2×2 matrix differential operator $\hat{L}$ has an eigenvalue whose real part is greater than zero. $\hat{L}$ always has a zero mode which corresponds to the translational symmetry of the CGLE. In the variational limit the operator $\hat{L}$ is self-adjoint and has two orthogonal eigenfunctions. The eigenfunction orthogonal to translational zero mode is the one responsible for the instability of the Ising wall.

As soon as we leave the variational limit the operator $\hat{L}$ ceases to be self-adjoint and the zero eigenvalue becomes degenerate (i.e. has algebraic multiplicity two). In addition, the eigenfunction orthogonal to the translational zero mode ceases to exist. $\hat{L}$ then has one eigenfunction and one generalized eigenfunction. The mode responsible for the instability of the Ising wall is now the translational zero mode. Thus the responsible mode has undergone a singular rotation. In the non-variational case Bloch walls move while in the variational case they are stationary. This is a result of the presence of the generalized eigenfunction.

1.4.2 Spatially forced periodic patterns

We saw in section 1.3.2 that the parametric driving term in the equation for the magnetization of an easy-axis ferromagnet was the result of spatial anisotropy. This phenomenon is referred to as spatially periodic forcing.

In [33], Coullet examines the effects of applying a spatially periodic forcing to a periodic pattern whose formation is governed by the real Ginzburg-Landau equation. Coullet's work was motivated by the experimental results of Lowe and Gollub [35] which showed that a spatially forced convective system undergoing pattern formation could show many different types of phase transitions including commensurate transitions (where the transition to the new state takes place simultaneously throughout the system) to both homogenous and modulated states, incommensurate transitions (where the transition occurs first at isolated points) which are described by sine-Gordon solitons and transitions to lattice structures made up of many solitons.

The amplitude equation Coullet derives is

$$A_t = \mu A - |A|^2 A - \alpha \overline{A}^{\,n-1} e^{inqx} + A_{xx} + \textit{higher order terms}\,, \tag{1.19}$$

which is similar to that for a system experiencing periodic time-dependent forcing near a Hopf bifurcation except that all the coefficients are real and there is the x dependent factor e^{inqx} multiplying $\overline{A}^{\,n-1}$. In the case of time-dependent forcing this factor would be e^{inqt} and could be removed by a rotation of the phase of A and a translation of the parameter μ since (1.19) depends only on the first time derivative of A. The same cannot be done for the x dependent factor since (1.19) depends on the second spatial derivative of A.

The parameters n and q are defined via the wave number of the periodic pattern, k_0, and the wave number of the spatial forcing k_1. If k_1/k_0 is close to a rational number n/m (with n and m being relatively prime) then q is given by $q = mk_1 - nk_0$. The parameter q is the detuning or misfit parameter. When detuning is absent ($q = 0$) the effect of spatially periodic forcing on the resulting amplitude equation is identical to that of time-dependent parametric driving. Setting $q = 0$ and $n = 2$ we obtain from (1.19) the parametrically driven Ginzburg-Landau equation which describes the magnetization of an easy-axis ferromagnet.

The amplitude equation (1.19) has a gradient (variational) structure even when $q \neq 0$ and can be written

$$A_t = -\frac{\delta F}{\delta \overline{A}} \tag{1.20}$$

$$F = \int \left\{ -u|A|^2 - \frac{\alpha}{n}\left[\overline{A}^n e^{inqx} + A^n e^{-inqx}\right] + \frac{1}{2}|A|^4 + |A_x|^2 \right\} \mathrm{d}x \,. \tag{1.21}$$

Coullet shows that in the parameter range

$$\mu - q^2 + \alpha(n-1)Q^{n-2} - 3Q^2 << -n\alpha Q^{n-2} \tag{1.22}$$

(where Q is the amplitude of the non-trivial homogeneous stationary solution) the potential F may be reduced via an adiabatic approximation to the continuous limit of the potential energy of the Frenkel-Kontorova [34] model. (The Frenkel-Kontorova model is an equillibrium model describing the dynamics of a chain of interacting particles subject to a sinusoidal external potential. Its continuum limit is the completely integrable sine-Gordon equation.)

When q is greater than the critical value

$$q_c^2 = 16\alpha Q^{n-2}/n\pi^2 \,, \tag{1.23}$$

the locked non-localised states are no longer the absolute minima of the potential function. Rather, the minimum is given by a localised structure which corresponds to the one-soliton solution of the 1D sine-Gordon equation. Consequently, when $q > q_c$ the phase transition no longer takes place simultaneously throughout the system but occurs through the formation of localised bubbles (the solitons) of the new state. When $q >> q_c$ many bubbles are set up simultaneously at the transition point forming a lattice of localised soliton-like structures.

1.4.3 Composite and moving pulses in the CGLE

Afanasjev, Akhmediev and Soto-Crespo [36] in 1996 discovered two unexpected types of solutions to the CGLE in numerical simulations.

The first unexpected solution was a composite pulse, which is a stationary solution made up of a source with a front (kink) bound on either side. Whereas a pulse is a spatially localised defect joining two homogenous solutions, a source is a localised defect which joins two oscillatory backgrounds. A source derives its name from the fact in the non-stationary case the oscillatory backgrounds may be travelling waves which move outwards from the localised defect. The opposite case, where the waves move towards the localised defect, is called a sink. This composite pulse is of interest to us since it is similar to one we find in chapter 4 although it occurs as the solution of the *undriven* CGLE.

The second unexpected solution was an asymmetric pulse which moves with constant velocity.

The parameter ranges where the normal pulse, composite pulse and moving pulse exist overlap, so all three may coexist (occur simultaneously).

The form of the complex Ginzburg-Landau examined by Afanasjev *et al* is the quintic form commonly used in optics [37] , namely

$$i\psi_z + \frac{c}{2}\psi_{tt} + |\psi|^2\psi + \nu|\psi|^4\psi = i\delta\psi + i\epsilon|\psi|^2\psi + i\beta\psi_{tt} + i\mu|\psi|^4\psi \,. \tag{1.24}$$

The variables and parameters are as follows: z the propagation distance, t the retarded time, ψ the normalized electromagnetic field envelope, δ the linear gain, β the spectral filtering parameter, ϵ the nonlinear gain parameter, μ the saturation of the nonlinear gain (if negative), ν the saturation of the nonlinear refractive index. c is $+1$ if the group velocity is anomalous and -1 if the group velocity is normal. The group velocity is anomalous if it is greater than the phase velocity otherwise it is said to be normal. Afanasjev *et al* deal with the (anomalous) $c = 1$ case.

Afanasjev *et al* begin their simulations with two fronts separated by a wide plateau of the non-zero background. In this situation the fronts either move towards each other eventually forming a stationary pulse or move apart so that the non-trivial background invades the zero background, depending on the values of the parameters c, ν, δ, ϵ, β and μ in equation (1.24). Afanasjev et al discovered that when fronts approach each other they may also form a composite pulse in which a source of oscillatory waves on the non-trivial background is trapped between the two fronts. That such a source is indeed trapped between the two fronts can be seen from the Fourier spectrum of the composite pulse which consists of two peaks. The peaks appear since the waves on the left and right of the source have opposite wave numbers. If the composite pulse is wide then the spectral peaks are narrower (since the region of plane waves surrounding the source is larger). On the other hand, if the composite pulse is narrow then the spectral peaks are broad. The existence of the composite pulse results from a balance between the velocity of the front and a repulsive force between the fronts and the source. If the front velocity is too large the repulsive force is overcome and a normal (non-composite) pulse forms. At the parameter boundary where the front velocity is just unable to overcome the repulsive force, periodic oscillating solutions with complex interactions between the front and source were discovered.

The moving pulses discovered in [36] are asymmetric and appear to be bound states consisting of a normal symmetric pulse and a front. The normal pulse by itself is stationary, but the front bound to it pushes it along. The normal pulse is never pulled by the front as the moving pulse only occurs in the parameter region where the front velocity is towards the nonzero background (i.e. towards the side of the front that is connected to the pulse). The velocity of the moving pulse is always less than that of a front by itself, as the pulse retards the motion of the front.

Moving solutions with constant velocity were also considered by van Saarloos and Hohenberg in [38].

1.4.4 Analytic solitary wave solutions of the damped nonlinear Schrödinger equation

The NLS equation has the form

$$i\psi_t + \psi_{xx} + |\psi|^2\psi = 0\,. \tag{1.25}$$

Introducing a linear growth rate into the dispersion relation for equation (1.25) of the form $\gamma(k) = \gamma_0 - ck^2$ for each Fourier mode (with wave number k) of ψ as was done by Pereira and Stenflo [39] results in the the addition of the terms

$$+i\gamma_0\psi + ic\psi_{xx} \tag{1.26}$$

to the right-hand side of equation (1.25). This gives the equation

$$i\psi_t + (1 - ic)\psi_{xx} + |\psi|^2\psi - i\gamma_0\psi = 0 \tag{1.27}$$

which is the zero driving limit of the equation we study in chapter 4. The parameter c is known as the filtering parameter since it filters the spectrum of ψ by damping modes with large wave number k more strongly.

Pereira and Stenflo also consider the effects of amplitude dependent damping which adds the term $-i\gamma_n|\psi|^2\psi$ to the right-hand side of equation (1.25) and yields:

$$i\psi_t + (1 - ic)\psi_{xx} + |\psi|^2\psi - i\gamma_0\psi + i\gamma_n|\psi|^2\psi = 0\,. \tag{1.28}$$

Pereira in [40] shows that when the damping and growth rates γ_0, c and γ_n are small the pulse

$$\psi = \sqrt{2}K(t)\mathrm{sech}\,(K(t)x)\,e^{i\int_0^t K^2(t')\,\mathrm{d}t'} \tag{1.29}$$

provides an approximate solution to equation (1.28) if $K(t)$ satisfies

$$\frac{1}{2}K_t = \gamma_0 K - (c + 4\gamma_n)\frac{K^3}{3} \quad . \tag{1.30}$$

The time dependence of K is derived by examining the time dependence of $\int |\psi|^2\mathrm{d}x$ which is conserved by (1.25). The magnitude of the pulse grows when $K^2 < K_e^2$ which is given by

$$K_e^2 = \frac{3\gamma_0}{c + 4\gamma_n} \quad , \tag{1.31}$$

and grows exponentially if $K^2 << K_e^2$. The amplitude decreases if $K^2 > K_e^2$ and decreases as $t^{-1/2}$ for K^2 much larger than K_e^2.

If $c + 4\gamma_n < 0$ the magnitude of K may grow explosively and become infinite in a finite time,

$$t_0 = \frac{1}{4\gamma_0} \ln \left[1 - \frac{K_e^2}{K(0)^2} \right] \quad . \tag{1.32}$$

This is the case of dispersive and amplitude dependent growth.

Equation (1.28) also has the exact solution (found by Pereira and Stenflo [39])

$$\psi = \sqrt{2} L \left[\text{sech} \left(Kx \right) \right]^{1+i\alpha} e^{i\Omega t} \tag{1.33}$$

where the constants α, β, K, L and Ω are given by

$$\begin{aligned} L^2 &= K^2 \left(1 + \frac{3}{2}\alpha c - \frac{1}{2}\alpha^2 \right) \\ K^2 &= \frac{\gamma_0}{2\alpha - c + \alpha^2 c} \\ \Omega &= -K^2 \left(1 + 2\alpha c - \alpha^2 \right) \\ \alpha &= -\beta + (2 + \beta^2)^2 \\ \beta &= \frac{3}{2} \left[\frac{1 - c\gamma_n}{c + \gamma_n} \right] \quad . \end{aligned} \tag{1.34}$$

As mentioned previously, solution (1.33) is a promising starting point for further work exploring localised solutions of the parametrically driven CGLE using the same continuation methods employed in chapters 4 and 5. However, in chapters 4 and 5 we restrict ourselves to continuing solutions to driven equations and so do not use solution (1.33) as a starting point in our continuations. The pulse and front solutions that we continue are introduced at the start of chapters 4 and 5 respectively.

1.5 Summary

We began by introducing the complex Ginzburg-Landau and NLS equations and their parametrically driven extensions. We saw that the form of the parametric driving term depends on the ratio between the frequency of the parametric forcing and that of the modes excited at the Hopf bifurcation. We singled out the special case, $s = 2$, for which the frequency of the forcing is twice the frequency of the excited modes and pointed out the simple form of the driving term in this case. The $s = 2$ case has received the most experimental and theoretical attention and is the one we will concern ourselves with for much of this thesis.

We next introduced the concept of the continuation of a solution in a set of parameters and explained how we would use this in chapters 4 and 5 to numerically construct localised solutions to the driven CGLE. In section 1.2 we motivated

this approach on the grounds that the damped-driven NLS equation has been successfully used to model localised structures occurring in physical systems more fully described by the driven CGLE.

Then in section 1.3 we looked at two physical applications of the the driven CGLE, namely optical parametric oscillators and ferromagnets. A third example, the Faraday resonance experiment, will be covered at length in chapter 2.

In section 1.4 we went on to discuss some theoretical aspects of the CGLE. This started with a comparison of the variational limits of the driven and undriven CGLEs. We saw that *stationary* localised structures are uncommon in the variational limit of the undriven CGLE but not in the variational limit of the driven CGLE. In the case of the driven CGLE with defocusing nonlinearity, we also saw that the mode responsible for the loss of stability of one localised structure (the Ising wall) to another localised structure (the Bloch wall) underwent a singular rotation when the driven CGLE reached its variational limit. From there we proceeded to discuss spatial forcing and saw that the additional term which arises in the amplitude equation as a result of spatial forcing is the same as that which results from time-periodic forcing provided there is no detuning. We then mentioned some known composite and moving pulse solutions to the undriven CGLE which were found in numerical simulations by Afanasjev, Akhmediev and Soto-Crespo [36]. The composite pulse solutions are qualitatively similar to some of the solutions to the driven CGLE that we construct in chapters 4 and 5. We ended the chapter by presenting a known analytic solution to the damped, undriven NLS equation which might be used as a starting point for constructing further solutions to the driven complex Ginzburg-Landau using the same continuation techniques we apply in the later part of this thesis.

Chapter 2

The Faraday Resonance Experiment

In chapter 2 we present the Faraday resonance experiment as a detailed example of a physical system for which the driven CGLE may be derived as an amplitude equation. We begin with a description of the physical apparatus and brief summary of the experiment's history in section 2.1. In section 2.2 we derive the hydrodynamic equations governing the fluid surface and discuss the boundary conditions that the fluid surface should satisfy. At the end of the chapter, in section 2.3 we examine the linearised hydrodynamic equations. We do not derive the amplitude equation in this chapter. Instead, a more general discussion of how the amplitude equation arises from a set of linearised equations is left for chapter 3. Much of sections 2.2 and 2.3 are adapted from two papers. The first, by Benjamin and Ursell [41], examines the linear behaviour of the Faraday Resonance system. The second, by Meron and Procaccia [42], extends the analysis of Benjamin and Ursell to the nonlinear case and derives the amplitude equation for the system.

2.1 Historical aspects

The experiment, which was first performed by Michael Faraday in 1831 [8], consists of a fluid filled container which is caused to oscillate vertically by the application of a harmonic driving force with amplitude A and frequency ω. The experimental setup is extremely simple and a qualitative experiment may be performed using only a bowl of water and a loudspeaker. A typical experimental setup is shown in Figure 2.1 below and consists of a container filled with fluid, an oscillator (typically a loudspeaker) and a signal generator which drives the oscillator.

In general the container may be of any shape, but we will consider only containers with flat bottoms and vertical sides. The horizontal cross-section of the container is rectangular in many experiments, as shown in the diagram (Figure 2.1). However, other shapes for the horizontal cross-section are not too difficult to treat

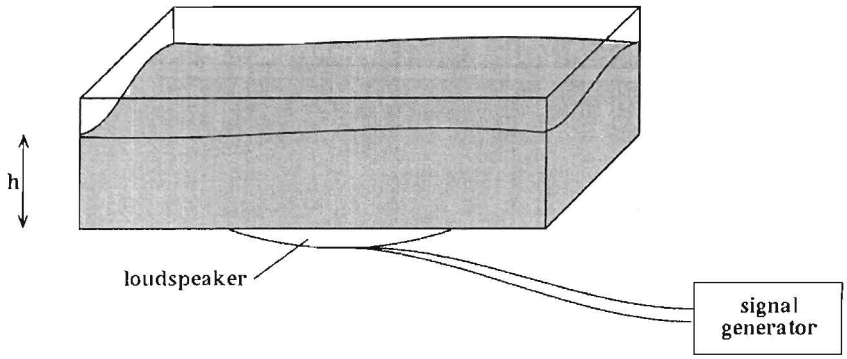

Figure 2 1: *Typical experimental setup for the Faraday resonance experiment.*

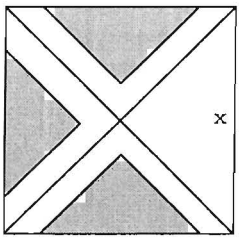

Figure 2.2: *One of Faraday's experimental setups. It consisted of a square metal or glass plate clamped at the centre and covered with water. The "x" marks the spot where the plate was bowed. The grey areas show where the crinkles formed on the water surface. The solid lines along the diagonal of the square mark the nodal lines of the vibration. The plate is clamped in place at the center of the square where the two nodal lines cross. The drawing is a recreation of Fig. 12 in Faraday's paper [8].*

theoretically. The principle effect, as we will see later, is to alter the modes of excitation which satisfy the boundary conditions.

The depth, h, shown in the diagram is the height of the fluid above the bottom of the container when no oscillatory force is applied.

Faraday, of course, did not use the experimental setup shown in Figure 2.1. Much of Faraday's 1831 paper [8] is, in fact, devoted to the forms assumed by light powders upon a vibrating metal surface. The section on the behaviour of fluids is a separate paper attached as an appendix to the [8]. Faraday was also not the first to investigate the behaviour of a fluid upon a vibrating surface. Earlier observations (referenced by Faraday) had been made by Oersted, Wheatstone and Weber. Faraday employed a number of different experimental setups, the first of which consisted of a square plate (either metal or glass) clamped in the middle and with a layer of water on top. The plate was made to vibrate by dragging a bow down the one edge. See Figure 2.2.

Upon bowing, Faraday observed that the water surface became crinkled in three triangular regions adjacent to the three edges of the square plate furthest from the bow. These crinkled regions did not extend over the entire plate as the

lines joining the corners of of the square plate to the centre (which is clamped) are nodal lines. Each crinkled region consisted of small rounded oscillating elevations of the water surface, usually arranged in a regular rectangular pattern. The height of the individual elevations was found to increase as the strength of the vibration was increased. The lateral extent of the elevations was not effected by the strength of the vibration, but rather by its frequency. The extent was smaller for higher frequencies and larger for lower frequencies.

Further investigation by Faraday revealed that when the driving force was small the elevations of the fluid surface oscillated vertically at half the frequency of the applied vibration. However, in 1868 Matthiessen [43], [44] found after performing a similar experiment that the fluid surface oscillated at the same frequency as the driving force. Then in 1883 Rayleigh redid the experiment [45] and obtained results which agreed with Faraday's. In the same year Rayleigh derived Mathieu's equation for the motion of the fluid surface [46].

For a long time the discrepancy between the results of Matthiessen on the one hand, and Faraday and Rayleigh on the other, remained unresolved. It wasn't until 1954 that Benjamin and Ursell [41], after further experimentation, derived a theory for the small amplitude oscillations which could reconcile the conflicting results.

More recent experiments and theoretical works, begun in the early 1980s, have sought to investigate nonlinear effects, that is when the oscillations of the fluid surface may no longer be considered small and higher order terms in the hydrodynamic equations are relevant. Such nonlinear effects include solitons, pattern formation and turbulence. The investigations of localised structures in the Faraday resonance experiment were initially restricted to one dimensional systems but recently the theoretical study of localised two dimensional structures has begun [47].

2.2 The equations governing the fluid surface

The hydrodynamic equations governing the velocity field, $\vec{V}$, of an incompressible fluid with negligible viscosity are Euler's equations,

$$\frac{\partial \vec{V}}{\partial t} + (\vec{V} \cdot \vec{\nabla})\vec{V} = -\frac{1}{\rho}\vec{\nabla}P\,, \tag{2.1}$$

where ρ is the density of the fluid (which is assumed constant) and P the pressure. The right hand side is just minus the force per unit mass which acts on the particles within the fluid. If we include a uniform gravitational field and orientate our system so that the acceleration due to gravity is $-g\hat{z}$ then equations become

$$\frac{\partial \vec{V}}{\partial t} + (\vec{V} \cdot \vec{\nabla})\vec{V} = -\frac{1}{\rho}\vec{\nabla}P + g\hat{z}\,. \tag{2.2}$$

Since we have assumed that the fluid is incompressible the effect of vertically oscillating the container in which the fluid resides is to apply a force $A\cos(\omega t)\hat{z}$ to each particle within the fluid. The relevant hydrodynamic equations are

$$\frac{\partial \vec{V}}{\partial t} + (\vec{V}\cdot\vec{\nabla})\vec{V} = -\frac{1}{\rho}\vec{\nabla}P + [g - A\cos(\omega t)]\hat{z}\ . \tag{2.3}$$

The assumption that the fluid is incompressible is valid when the velocity field is subsonic everywhere. That this is the case for all Faraday resonance experiments may be seen as follows: The speed of the oscillations of the container is less than the speed of sound in air. The speed of sound in air is less than the speed of sound in most liquids, since liquids are typically denser. Thus the magnitudes of the velocities involved are much less than the speed of sound in the liquid.

The conservation of mass equation expressing the incompressibility of the fluid is

$$\vec{\nabla}\cdot\vec{V} = \vec{0}\ . \tag{2.4}$$

By neglecting the viscosity of the fluid and assuming that the motion of the fluid starts from rest, we are able to introduce a velocity potential [48], ϕ, such that

$$\vec{V} = \vec{\nabla}\phi\ . \tag{2.5}$$

Using the potential, ϕ, the incompressibility equation (2.4) and the hydrodynamic equations (2.3) may be written as

$$\nabla^2\phi = 0 \tag{2.6}$$

and

$$\frac{\partial}{\partial t}(\vec{\nabla}\phi) + (\vec{\nabla}\phi\cdot\vec{\nabla})(\vec{\nabla}\phi) = -\frac{1}{\rho}\vec{\nabla}P + [g - A\cos(\omega t)]\hat{z}\ , \tag{2.7}$$

respectively.

The term $(\vec{\nabla}\phi\cdot\vec{\nabla})(\vec{\nabla}\phi)$ in (2.7) may be rewritten $\frac{1}{2}\vec{\nabla}(|\vec{\nabla}\phi|^2)$. This allows us to rewrite (2.7) as

$$\begin{aligned}
& \tfrac{\partial}{\partial t}(\vec{\nabla}\phi) + \tfrac{1}{2}\vec{\nabla}(|\vec{\nabla}\phi|^2) &&= -\tfrac{1}{\rho}\vec{\nabla}P + [g - A\cos(\omega t)]\hat{z}\ , \\
\text{whence}\quad & \vec{\nabla}\left[\phi_t + \tfrac{1}{2}|\vec{\nabla}\phi|^2 + \tfrac{P}{\rho}\right] &&= [g - A\cos(\omega t)]\hat{z} \\
\text{and so}\quad & \tfrac{\partial}{\partial x}\left[\phi_t + \tfrac{1}{2}|\vec{\nabla}\phi|^2 + \tfrac{P}{\rho}\right] &&= 0 \\
& \tfrac{\partial}{\partial y}\left[\phi_t + \tfrac{1}{2}|\vec{\nabla}\phi|^2 + \tfrac{P}{\rho}\right] &&= 0 \\
& \tfrac{\partial}{\partial z}\left[\phi_t + \tfrac{1}{2}|\vec{\nabla}\phi|^2 + \tfrac{P}{\rho}\right] &&= [g - A\cos(\omega t)]\ .
\end{aligned} \tag{2.8}$$

Integrating the three equations (2.8) gives

$$\phi_t + \frac{1}{2}|\vec{\nabla}\phi|^2 + \frac{P}{\rho} = f_1(y,z,t)$$

$$\begin{aligned} \phi_t + \frac{1}{2}|\vec{\nabla}\phi|^2 + \frac{P}{\rho} &= f_2(x,z,t) \\ \phi_t + \frac{1}{2}|\vec{\nabla}\phi|^2 + \frac{P}{\rho} &= f_3(x,y,t) + [g - A\cos(\omega t)]z \ . \end{aligned} \tag{2.9}$$

Equating the right hand sides of (2.9) gives

$$f_1(y,z,t) = f_2(x,z,t) = f_3(x,y,t) + [g - A\cos(\omega t)]z \tag{2.10}$$

which implies that f_3 is a function of t only. Thus

$$\phi_t + \frac{1}{2}|\vec{\nabla}\phi|^2 + \frac{P}{\rho} - [g - A\cos(\omega t)]z = f_3(t) \ . \tag{2.11}$$

Since ϕ is defined by $\vec{V} = \vec{\nabla}\phi$ we may add any function of t to ϕ without altering the velocity field. We use this freedom to add $\int^t f_3(t')\mathrm{d}t'$ to ϕ and eliminate $f_3(t)$ from (2.11). The result is

$$\phi_t + \frac{1}{2}|\vec{\nabla}\phi|^2 + \frac{P}{\rho} - [g - A\cos(\omega t)]z = 0 \ , \tag{2.12}$$

which is an evolution equation for the velocity potential of the fluid.

We now need to derive evolution equations for the fluid surface. The pressure at the surface of the fluid is given by

$$P = -\gamma\left(\frac{1}{R_1} + \frac{1}{R_2}\right) \tag{2.13}$$

where γ is the surface tension of the fluid and R_1 and R_2 are the principal radii of curvature of the surface.

Following the method of Landau and Lifshitz [49] we will derive an approximation for $\frac{1}{R_1} + \frac{1}{R_2}$ for the case where the surface $z = \zeta(x,y,t)$ remains almost flat.

We consider a change δf in surface area induced in a portion of the surface by a small change $\delta\zeta$ in the height of the surface. Initially the surface area element is $\mathrm{d}f = \mathrm{d}l_1\mathrm{d}l_2$ where l_1 and l_2 are the co-ordinates on the principal sections of the surface. After the increment $\delta\zeta$ has been added to the height of the surface the line elements become $\delta l_1'$ and $\delta l_2'$.

From Figure 2.3 we note that $\mathrm{d}l = R\theta$ and $\mathrm{d}l' = (R + \delta\zeta)\theta$. Thus

$$\begin{aligned} \tfrac{\mathrm{d}l}{R} &= \tfrac{\mathrm{d}l'}{R+\delta\zeta} \\ \Rightarrow \ \mathrm{d}l' &= \left(1 + \tfrac{\delta\zeta}{R}\right)\mathrm{d}l \ , \end{aligned} \tag{2.14}$$

and the surface element $\mathrm{d}f = \mathrm{d}l_1\mathrm{d}l_2 \rightarrow \mathrm{d}f' = (1 + \frac{\delta\zeta}{R_1})\,\mathrm{d}l_1\,(1 + \frac{\delta\zeta}{R_2})\,\mathrm{d}l_2$. To first order in $\delta\zeta$ we have

$$\mathrm{d}f' \approx \left(1 + \frac{\delta\zeta}{R_1} + \frac{\delta\zeta}{R_2}\right)\mathrm{d}l_1\,\mathrm{d}l_2 \ . \tag{2.15}$$

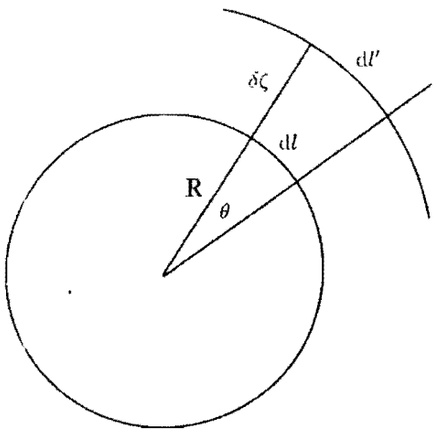

Figure 2.3: *Change in a line element* dl *after a change in height* $\delta\zeta$.

And the change in surface area is

$$\delta f = \int \mathrm{d}f' - \int \mathrm{d}f = \int \delta\zeta \left(\frac{1}{R_1} + \frac{1}{R_2}\right) \mathrm{d}l_1 \, \mathrm{d}l_2 \ . \tag{2.16}$$

where the integral is over the original portion of the surface.

Let us now assume that the fluid surface $z = \zeta(x, y, t)$ deviates only slightly from a plane of constant z so that ζ_x and ζ_y are small everywhere.

The surface area of the fluid is also given by

$$f = \int \sqrt{1 + \zeta_x^2 + \zeta_y^2} \, \mathrm{d}x \, \mathrm{d}y \tag{2.17}$$

and since ζ_x^2 and ζ_y^2 are small we may expand the square root in a Taylor series about $\zeta_x^2 = \zeta_y^2 = 0$. Letting $g(u) = \sqrt{1+u}$ we have

$$g(u) = g(0) + (u\frac{\mathrm{d}}{\mathrm{d}u})g(0) + \frac{1}{2!}(u\frac{\mathrm{d}}{\mathrm{d}u})^2 g(0) + \frac{1}{3!}(u\frac{\mathrm{d}}{\mathrm{d}u})^3 g(0) + \ldots \ . \tag{2.18}$$

The first derivative of g has the value $\frac{1}{2}$ when $u = 0$, the second derivatives has the value $-\frac{1}{4}$, and the n^{th} derivative has the value

$$a_n = \prod_{i=0}^{n-1} (\frac{1}{2} - i) \tag{2.19}$$

$$= \left(\frac{-1}{2}\right)^n \cdot \prod_{i=0}^{n-1} (2i - 1) \tag{2.20}$$

$$= \left(\frac{-1}{2}\right)^n (1)(3)(5)\ldots(2n-3) \tag{2.21}$$

$$= \left(\frac{-1}{2}\right)^n \frac{(2n-3)!}{2 \cdot (n-2)!} \ , \tag{2.22}$$

for $n \geq 2$. Thus

$$g(u) = 1 + \left(\frac{1}{2}\right) u + \frac{1}{2!}\left(\frac{-1}{4}\right) u^2 + \ldots + \frac{1}{n!}\,(a_n)\, u^n + \ldots \quad . \tag{2.23}$$

Substituting $\zeta_x^2 + \zeta_y^2$ for u in the expansion of g results in the expression

$$\begin{aligned} f \;=\; & \int \left[1 + \left(\frac{1}{2}\right)(\zeta_x^2 + \zeta_y^2) + \frac{1}{2!}\left(\frac{-1}{4}\right)(\zeta_x^2 + \zeta_y^2)^2 + \ldots \right. \\ & \left. + \frac{1}{n!}\,(a_n)\,(\zeta_x^2 + \zeta_y^2)^n + \ldots \right] \mathrm{d}x\,\mathrm{d}y \quad . \end{aligned} \tag{2.24}$$

Varying f with respect to ζ we obtain

$$\begin{aligned} \delta f \;=\; & \int \left[\zeta_x \frac{\partial(\delta\zeta)}{\partial x} + \zeta_y \frac{\partial(\delta\zeta)}{\partial y} + \frac{1}{2!}\left(\frac{-1}{4}\right)(2)(\zeta_x^2 + \zeta_y^2)\left\{ 2\zeta_x \frac{\partial(\delta\zeta)}{\partial x} + 2\zeta_y \frac{\partial(\delta\zeta)}{\partial y} \right\} + \right. \\ & \left. \ldots + \frac{n}{n!}\,(a_n)\,(\zeta_x^2 + \zeta_y^2)^{n-1}\left\{ 2\zeta_x \frac{\partial(\delta\zeta)}{\partial x} + 2\zeta_y \frac{\partial(\delta\zeta)}{\partial y} \right\} + \ldots \right] \mathrm{d}x\,\mathrm{d}y \quad . \end{aligned}$$

Now we integrate by parts to get rid of the partial derivatives of $\delta\zeta$. We integrate the terms containing $\frac{\partial(\delta\zeta)}{\partial x}$ by parts with respect to x and those containing $\frac{\partial(\delta\zeta)}{\partial y}$ with respect to y. After integrating by parts we find

$$\begin{aligned} \delta f = & -\int [\zeta_{xx} + \zeta_{yy} \\ & + \frac{1}{2!}\left(\frac{-1}{4}\right)(4)\left(2\left\{\zeta_x^2\zeta_{xx} + 2\zeta_x\zeta_y\zeta_{xy} + \zeta_y^2\zeta_{yy}\right\} + \left\{\zeta_x^2 + \zeta_y^2\right\}\left\{\zeta_{xx} + \zeta_{yy}\right\}\right) + \ldots \\ & + \frac{2n}{n!}\,(a_n)\left(\zeta_x^2 + \zeta_y^2\right)^{n-2}\left\{2(n-1)\left(\zeta_x^2\zeta_{xx} + 2\zeta_x\zeta_y\zeta_{xy} + \zeta_y^2\zeta_{yy}\right)\right. \\ & \left. + \left(\zeta_x^2 + \zeta_y^2\right)(\zeta_{xx} + \zeta_{yy})\right\} + \ldots] \,\delta\zeta\,\mathrm{d}x\,\mathrm{d}y \quad , \end{aligned} \tag{2.25}$$

provided that $\zeta_x\delta\zeta$ and $\zeta_y\delta\zeta$ are zero at the boundaries of the surface.

Since the surface is approximately flat, $\mathrm{d}x\,\mathrm{d}y \approx \mathrm{d}l_1\,\mathrm{d}l_2$. Comparing equation (2.25) with equation (2.16) we conclude that

$$\begin{aligned} \frac{1}{R_1} + \frac{1}{R_2} = & \zeta_{xx} + \zeta_{yy} \\ & + \frac{1}{2!}\left(\frac{-1}{4}\right)(4)\left(2\left\{\zeta_x^2\zeta_{xx} + 2\zeta_x\zeta_y\zeta_{xy} + \zeta_y^2\zeta_{yy}\right\} + \left\{\zeta_x^2 + \zeta_y^2\right\}\left\{\zeta_{xx} + \zeta_{yy}\right\}\right) + \ldots \\ & + \frac{2n}{n!}\,(a_n)\left(\zeta_x^2 + \zeta_y^2\right)^{n-2}\left\{2(n-1)\left(\zeta_x^2\zeta_{xx} + 2\zeta_x\zeta_y\zeta_{xy} + \zeta_y^2\zeta_{yy}\right) + \right. \\ & \left. \left(\zeta_x^2 + \zeta_y^2\right)(\zeta_{xx} + \zeta_{yy})\right\} + \ldots \quad . \end{aligned} \tag{2.26}$$

Now that we have an approximation for the pressure at the surface we can evaluate equation (2.12) at the fluid surface. Assuming that the surface remains flat (and thus close to $z = 0$) we may then expand the equation about $z = 0$. At the surface

$$\phi_t + \frac{1}{2}|\vec{\nabla}\phi|^2 + \frac{\gamma}{\rho}\left(\zeta_{xx} + \zeta_{yy} + N_2\right) - \left(g - A\cos\omega t\right) z = 0 \ . \tag{2.27}$$

N_2 represents the sum of the higher order terms in the approximation for $\frac{1}{R_1} + \frac{1}{R_2}$. We now expand all functions of z in (2.27) about $z = 0$. For small z we have

$$\phi_t = \phi_t|_{z=0} + \frac{\partial}{\partial z}\left(\phi_t\right)\Big|_{z=0} z + \ldots \text{ and} \tag{2.28}$$

$$\frac{1}{2}|\vec{\nabla}\phi|^2 = \left(\frac{1}{2}|\vec{\nabla}\phi|^2\right)\Big|_{z=0} + \left(|\vec{\nabla}\phi|\frac{\partial|\vec{\nabla}\phi|}{\partial z}\right)\Big|_{z=0} z + \ldots \ . \tag{2.29}$$

Substituting the above expansions into (2.27) and using $z = \zeta(x, y)$ we obtain

$$\begin{aligned}\phi_t|_{z=0} + \tfrac{\partial(\phi_t)}{\partial z}\Big|_{z=0}\zeta + \tfrac{1}{2}|\vec{\nabla}\phi|^2\Big|_{z=0} + |\vec{\nabla}\phi|\tfrac{\partial|\vec{\nabla}\phi|}{\partial z}\Big|_{z=0}\zeta \\ + \tfrac{\gamma}{\rho}(\zeta_{xx} + \zeta_{yy} + N_2) - (g - A\cos\omega t)\zeta = 0 \ .\end{aligned} \tag{2.30}$$

Or written differently as

$$\phi_t + \frac{\gamma}{\rho}(\zeta_{xx} + \zeta_{yy}) - (g - A\cos\omega t)\zeta + N_1 = 0 \tag{2.31}$$

$$N_1 = \zeta\phi_{zt} + \frac{1}{2}|\vec{\nabla}\phi|^2 + |\vec{\nabla}\phi|\frac{\partial|\vec{\nabla}\phi|}{\partial z}\zeta + \frac{\gamma}{\rho}N_2 \ , \tag{2.32}$$

where all functions of z are evaluated at $z = 0$ and all the nonlinear terms are contained in N_1.

Equation (2.32) has two unknown functions, namely $\phi(x, y, 0)$ and $\zeta(x, y)$. We need a second equation in order to complete the system. This second equation is the kinematic surface condition. During a small change in time $\mathrm{d}t$ a particle on the surface of the fluid experiences a change in height $\mathrm{d}\zeta$. The small change $\mathrm{d}t$ results in a change in position of $\mathrm{d}\vec{r} = \vec{v}\mathrm{d}t =< \phi_x, \phi_y, \phi_z > \mathrm{d}t$ since $\vec{v} = \vec{\nabla}\phi$. The change in position gives a change in height of $\mathrm{d}\zeta =< -\zeta_x, -\zeta_y, 1 > \cdot < \phi_x, \phi_y, \phi_z > \mathrm{d}t$ as $< -\zeta_x, -\zeta_y, 1 >$ is normal to the tangent plane of the fluid surface. Thus we arrive at the kinematic surface condition

$$\frac{\partial\zeta}{\partial t} = \phi_z - \left(\phi_x\zeta_x + \phi_y\zeta_y\right) \ . \tag{2.33}$$

The kinematic surface condition is also expanded around $z = 0$. Keeping terms up to second order in ζ and its derivatives we obtain

$$\begin{aligned}\zeta_t = \ & \phi_z]_{z=0} + \phi_{zz}]_{z=0}\zeta + \phi_{zzz}]_{z=0}\zeta^2 \\ & - \left\{\phi_x]_{z=0}\zeta_x + \phi_{xz}]_{z=0}\zeta\zeta_x + \phi_y]_{z=0}\zeta_y + \phi_{yz}]_{z=0}\zeta\zeta_y\right\}\end{aligned} \tag{2.34}$$

or

$$\zeta_t = \phi_z + N_3$$

$$N_3 = +\phi_{zz}\zeta + \phi_{zzz}\zeta^2 - \{\phi_x\zeta_x + \phi_{xz}\zeta\zeta_x + \phi_y\zeta_y + \phi_{yz}\zeta\zeta_y\} \tag{2.35}$$

where it is implicit that all functions of z are evaluated at $z = 0$ and all the nonlinear terms are contained in N_3. Using the relationship $\nabla^2\phi = 0$ we may rewrite N_3 as

$$N_3 = -(\phi_{xx} + \phi_{yy})\zeta - (\varphi_{xxz} + \phi_{yyz})\zeta^2 - \{\phi_x\zeta_x + \phi_{xz}\zeta\zeta_x + \phi_y\zeta_y + \phi_{yz}\zeta\zeta_y\} \ . \tag{2.36}$$

The definition of the potential (2.6) and the hydrodynamic equation (2.12) together with the hydrodynamic equation for the surface (2.32) and the kinematic surface condition (2.35) form a closed system of equations for $\zeta(x, y, t)$ and $\phi(x, y, z, t)$. The last piece required to complete the system is the boundary conditions.

In order to obtain these we notice, first, that the fluid cannot leave the container so at the boundaries of the container the component of the fluid velocity perpendicular to the container walls must be zero. This gives the conditions

$$\frac{\partial\phi}{\partial n} = 0 \text{ at the vertical walls,} \tag{2.37}$$

$$\text{and} \quad \frac{\partial\phi}{\partial z} = 0 \text{ on the bottom of the container.} \tag{2.38}$$

In (2.37), the derivative $\frac{\partial}{\partial n}$ is the directional derivative perpendicular to the container walls.

Finally, we assume that the fluid surface is horizontal were it meets the container walls:

$$\frac{\partial\zeta}{\partial n} = 0 \ . \tag{2.39}$$

If we linearise the equation for $\frac{\partial\zeta}{\partial t}$, (2.35), then we can derive the boundary condition (2.39) on $\zeta(t)$ from the boundary conditions (2.37) on ϕ. Initially the fluid surface is flat so $\frac{\partial\zeta}{\partial n} = 0$. Taking the partial derivative of equation (2.35) without the nonlinear term N_3, in the direction normal to the boundary curve of the fluid surface, gives

$$\frac{\partial^2\zeta}{\partial n\partial t} = \frac{\partial\phi}{\partial n\partial z} = 0 \ . \tag{2.40}$$

Thus $\frac{\partial}{\partial t}\left(\frac{\partial\zeta}{\partial n}\right) = 0$ and $\frac{\partial\zeta}{\partial n} = 0$ for all t.

If the nonlinear term N_3 is included then the boundary condition (2.39) becomes one of a large number of boundary conditions which are compatible with the boundary condition (2.37) on ϕ.

2.3 Linearised equations

We now proceed to analyze the linearised system of equations. We start by expanding $\zeta(x,y,t)$ and $\phi(x,y,z,t)$ over a complete set of orthonormal eigenfunctions $\{f_n(x,y)\}$ of the operator $\nabla_\perp^2 = \frac{\partial^2}{\partial x^2} + \frac{\partial^2}{\partial y^2}$.

Since $\nabla_\perp^2 f = -\lambda f$ with the boundary condition $\frac{\partial f}{\partial n} = 0$ is a Sturm-Louiville problem we are guaranteed to be able to find a complete set of eigenfunction f_n for the problem. All of these eigenfunctions will satisfy the boundary conditions and any function which satisfies the boundary conditions may be expanded over the eigenfunctions. In particular, we may expand ζ over the eigenfunctions.

The boundary curve along which $\frac{\partial f}{\partial n} = 0$ must be satisfied depends on the shape of the container. Thus different container shapes will result in different sets of eigenfunctions. In all other respects our treatment of different container shapes (so long as the container has vertical sides) is identical.

For convenience we write the eigenvalue of f_n as $-k_n^2$ so that $\nabla_\perp^2 f_n = -k_n^2 f_n$. The k_n may be complex. The expansions of ζ and ϕ are

$$\zeta(x,y,t) = \sum_n \zeta_n(t) f_n(x,y) \tag{2.41}$$

$$\text{and} \quad \phi(x,y,z,t) = \sum_n \phi_n(z,t) f_n(x,y)\,, \tag{2.42}$$

respectively. Substituting the expansion of ϕ into the equation $\nabla^2\phi = 0$ we find that

$$\nabla^2\phi = \sum_n \left[\frac{\partial^2\phi_n}{\partial z^2} f_n + \phi_n \nabla_\perp^2 f_n\right] \tag{2.43}$$

$$= \sum_n \left[\frac{\partial^2\phi_n}{\partial z^2} - k_n^2\phi_n\right] f_n \tag{2.44}$$

$$= 0\,. \tag{2.45}$$

Since the f_n are linearly independent this implies

$$\frac{\partial^2\phi_n}{\partial z^2} - k_n^2\phi_n = 0\,, \tag{2.46}$$

$$\text{whence} \quad \left[\frac{\partial}{\partial z} - k_n\right]\left[\frac{\partial}{\partial z} + k_n\right]\phi_n = 0\,. \tag{2.47}$$

The general solution to this linear differential equation is

$$\phi_n(z,t) = a_n(t)e^{k_n z} + b_n(t)e^{-k_n z}\,. \tag{2.48}$$

Applying the boundary condition $\frac{\partial\phi}{\partial z} = 0$ at the bottom of the container of fluid ($z = h$) we obtain

$$\left.\frac{\partial\phi}{\partial z}\right|_{z=h} = \sum_n \left.\frac{\partial\phi_n}{\partial z}\right|_{z=h} f_n = 0\,, \tag{2.49}$$

which implies that

$$\left.\frac{\partial \phi_n}{\partial z}\right|_{z=h} = 0\,, \tag{2.50}$$

$$\text{whence} \qquad k_n a_n(t) e^{hk_n} - k_n b(t) e^{-hk_n} = 0 \tag{2.51}$$

$$\text{and so} \qquad b_n(t) = a_n(t) e^{2hk_n}\,. \tag{2.52}$$

Thus $\phi_n(z,t) = a_n(t)\left[e^{k_n z} + e^{(2h-z)k_n}\right]$. Defining

$$\phi_n(t) = \phi_n(0,t) = a_n(t)\left[1 + e^{2hk_n}\right] \tag{2.53}$$

we have

$$\phi_n(z,t) = \phi_n(t)\frac{e^{k_n z} + e^{(2h-z)k_n}}{1 + e^{2hk_n}}\,. \tag{2.54}$$

The linearised equations for the fluid surface are

$$\phi_t + \left[\frac{\gamma}{\rho}\nabla_\perp^2 - g + A\cos\omega t\right]\zeta = 0 \tag{2.55}$$

$$\text{and} \quad \zeta_t = \phi_z\,, \tag{2.56}$$

where all functions of z should be evaluated at $z = 0$.

Substituting the expansions (2.41) and (2.42) into the linearised equations (2.55) and (2.56) we obtain

$$\sum_n \left\{ \frac{\partial \phi_n}{\partial t}\left[\frac{e^{k_n z} + e^{(2h-z)k_n}}{1 + e^{2hk_n}}\right] f_n + \left[-k_n^2\frac{\gamma}{\rho} - g + A\cos\omega t\right]\zeta_n f_n \right\} = 0\,, \tag{2.57}$$

$$\text{whence} \quad \frac{\partial \phi_n}{\partial t}\left[\frac{e^{k_n z} + e^{(2h-z)k_n}}{1 + e^{2hk_n}}\right] + \left[-k_n^2\frac{\gamma}{\rho} - g + A\cos\omega t\right]\zeta_n = 0 \tag{2.58}$$

and

$$\sum_n \frac{\partial \zeta_n}{\partial t} f_n = \sum_n \phi_n(t)\left[\frac{k_n e^{k_n z} - k_n e^{(2h-z)k_n}}{1 + e^{2hk_n}}\right] f_n\,, \tag{2.59}$$

$$\text{whence} \quad \frac{\partial \zeta_n}{\partial t} = \phi_n(t)\left[\frac{k_n e^{k_n z} - k_n e^{(2h-z)k_n}}{1 + e^{2hk_n}}\right]\,. \tag{2.60}$$

Evaluating the expressions (2.58) and (2.60) at $z = 0$ results in

$$\frac{\mathrm{d}\phi_n}{\mathrm{d}t} + \left[-k_n^2\frac{\gamma}{\rho} - g + A\cos\omega t\right]\zeta_n = 0\,, \tag{2.61}$$

$$\frac{\mathrm{d}\zeta_n}{\mathrm{d}t} = -k_n \tanh(hk_n)\phi_n(t)\,. \tag{2.62}$$

Writing this pair of equations for ζ_n and ϕ_n as

$$\vec{x_n}'(t) = \mathrm{A_n}(t)\vec{x_n}(t) \tag{2.63}$$

with

$$\vec{x_n} = \begin{pmatrix} \zeta_n(t) \\ \phi_n(t) \end{pmatrix} \tag{2.64}$$

$$\mathrm{A_n} = \begin{pmatrix} 0 & -k_n \tanh(hk_n) \\ \frac{\gamma}{\rho}k_n^2 + g - A\cos\omega t & 0 \end{pmatrix} \tag{2.65}$$

shows it to be a Floquet problem since the matrix $\mathrm{A}(t)$ is periodic in time. The period of $\mathrm{A}(t)$ is $2\pi/\omega$.

Alternatively, taking the derivative of the second equation and substituting in the first equation results in

$$\frac{\mathrm{d}^2\zeta_n}{\mathrm{d}t^2} = -k_n \tanh(hk_n)\frac{\mathrm{d}\phi_n}{\mathrm{d}t} \tag{2.66}$$

$$= -k_n \tanh(hk_n)\left[\frac{\gamma}{\rho}k_n^2 + g - A\cos\omega t\right]\zeta_n \ , \tag{2.67}$$

which is a Mathieu equation for ζ_n.

Since (2.63) is a Floquet problem, any fundamental matrix, $\mathrm{X_n}(t)$, for equation (2.63) may be written as

$$\mathrm{X_n}(t) = \mathrm{P_n}(t)e^{t\mathrm{R_n}} \ , \tag{2.68}$$

where $\mathrm{P_n}(t)$ has the same periodicity as $\mathrm{A_n}(t)$ and $\mathrm{R_n}$ is an invertible matrix which is independent of t. A fundamental matrix of (2.63) is one whose columns are linearly independent solutions of (2.63). We prove (2.68) as follows:

Let $\mathrm{Y_n}(t) = \mathrm{X_n}(t+\tau)$ where τ is the period of $\mathrm{A_n}(t)$, i.e. $\mathrm{A_n}(t) = \mathrm{A_n}(t+\tau)$. Then

$$\begin{aligned} \mathrm{Y_n}'(t) &= \mathrm{X_n}'(t+\tau) \\ &= \mathrm{A_n}(t+\tau)\mathrm{X_n}(t+\tau) \\ &= \mathrm{A_n}(t)\mathrm{Y_n}(t) \ . \end{aligned} \tag{2.69}$$

Thus $\mathrm{Y_n}(t)$ is also a fundamental matrix of (2.63). The columns of $\mathrm{Y_n}(t)$ are linearly independent for all t since

$$\det \mathrm{Y_n}(t) = \det \mathrm{X_n}(t+\tau) \neq 0 \tag{2.70}$$

for all t. $\mathrm{X_n}(t)$ is invertible so we may define

$$\mathrm{C_n}(t) = \mathrm{X_n}^{-1}(t)\mathrm{Y_n}(t) \ . \tag{2.71}$$

Now

$$\mathrm{Y_n}(t) = \mathrm{X_n}(t)\mathrm{C_n}(t)\,, \tag{2.72}$$

so

$$\mathrm{Y_n}'(t) = \mathrm{X_n}'(t)\mathrm{C_n}(t) + \mathrm{X_n}(t)\mathrm{C_n}'(t)\,. \tag{2.73}$$

However, we also have

$$\begin{aligned} \mathrm{Y_n}'(t) &= \mathrm{A_n}(t)\mathrm{Y_n}(t) \\ &= \mathrm{A_n}(t)\mathrm{X_n}(t)\mathrm{C_n}(t) \\ &= \mathrm{X_n}'(t)\mathrm{C_n}(t)\,. \end{aligned} \tag{2.74}$$

Thus $\mathrm{X_n}(t)\mathrm{C_n}'(t) = 0$. Since $\mathrm{X_n}(t)$ is invertible $\mathrm{C_n}'(t) = 0$. Hence, $\mathrm{C_n}$ is independent of t. $\mathrm{C_n}$ is also invertible since it is the product of two invertible matrices. We have now shown that $\mathrm{X_n}(t+\tau) = \mathrm{X_n}(t)\mathrm{C_n}$. Every $n \times n$ invertible matrix can be written as e^{B} for some $n \times n$ matrix B. Let $\mathrm{C_n} = e^{\tau \mathrm{R_n}}$ and define

$$\mathrm{P_n}(t) = \mathrm{X_n}(t)e^{-t\mathrm{R_n}}\,. \tag{2.75}$$

We now have

$$\mathrm{X_n}(t) = \mathrm{P_n}(t)e^{t\mathrm{R_n}} \tag{2.76}$$

and

$$\begin{aligned} \mathrm{P_n}(t+\tau) &= \mathrm{X_n}(t+\tau)e^{-\tau \mathrm{R_n}}e^{-t\mathrm{R_n}} \\ &= \mathrm{X_n}(t)e^{-t\mathrm{R_n}} \\ &= \mathrm{P_n}(t)\,, \end{aligned} \tag{2.77}$$

completing the proof.

The eigenvalues of the matrix $\mathrm{R_n}$ are the Floquet characteristic exponents. The real parts of the eigenvalues of $\mathrm{R_n}$ determine the stability of the n^{th} mode.

We have now finished our analysis of the linearised hydrodynamic equations. The next step in deriving an amplitude equation for the system is to find at which point (in the parameter space) one or more of the linear modes become unstable. This is done by solving the Floquet problem (2.63), calculating the matrix $\mathrm{R_n}$ and examining how the real parts of the eigenvalues of $\mathrm{R_n}$ change as the parameters are varied. When the real part of one of the eigenvalues becomes positive, the associated mode has lost its stability. The linear equation predicts that these unstable modes will grow exponentially with time but in practice the nonlinearities will curb this exponential growth and the amplitude of the excited modes will, in fact, satisfy some nonlinear amplitude equation. In chapter 3 we examine how such an amplitude equation may be derived by considering the symmetries present in the original nonlinear system.

2.4 Summary

This chapter on the Faraday resonance experiment was separated out from the section in the introduction which covered other applications because of this chapters length. We began it by describing the experimental setup employed in the Faraday resonance experiment and briefly recounting Faraday's original qualitative investigation of the periodic forcing of a fluid and his observations of crinkles on the fluid surface. We also mentioned a number of important milestones in history of the experiment's theoretical analysis.

In section 2.2 we started from the hydrodynamic equations for an incompressible fluid with negligible velocity and proceeded to derive the nonlinear equations governing the surface of a fluid undergoing periodic forcing. During the course of the derivation we had to approximate the pressure at the fluid surface taking into account the dependence of the pressure on the surface shape. We then linearised the equations for the fluid surface and determined suitable boundary conditions.

The final section, section 2.3, dealt with the linearised equations. The linear partial differential was converted into a first-order ordinary differential equation (in time) by expanding the fluid surface and velocity potential over the (spatial) eigenfunctions of the two-dimensional Laplace operator with suitable boundary conditions. The resulting differential matrix equation was shown to be a Floquet problem since the matrix A_n was periodic in time. It was then proved that the long time behaviour of the solutions to the Floquet problem depends only on the real parts of the eigenvalues of a constant (independent of the spatial and temporal variables) matrix, R_n. The driven CGLE will arise as the amplitude equation for linear modes which become unstable - but more on that in chapter 3.

Chapter 3

Deriving the CGLE

In chapter 3 we look at how an amplitude equation, in this case the CGLE, may be derived for modes (of a linearised system) which have become unstable. We keep the discussion general rather than relating it to a particular linear system. However, the nonlinear system from which the linear system is derived must satisfy certain conditions in order that the CGLE arise as the amplitude equation for its unstable linear modes.

In the first section of this chapter we examine the case where the original system is undriven. This does not apply to the Faraday resonance experiment, since that system is parametrically driven, but serves to illustrate how considerations of symmetry may be used to construct the amplitude equation. Our exposition in this first section follows that of Mori and Kuramoto [50].

In the second section of this chapter we examine the case where parametric driving is present in the original system, drawing on the work of Elphick, Iooss and Tirapegui [51]. This is applicable to Faraday resonance experiment. In the second section we consider, in addition to the effect of parametric driving on the CGLE, the effect of parametric driving on the amplitude equation relevant at a saddle-node bifurcation.

3.1 The undriven CGLE

The CGLE arises as the amplitude equation for a real vector field near a Hopf bifurcation in some parameter μ. During such a Hopf bifurcation a fixed point of the vector field (a spatially uniform, stationary solution of the field equations) loses or gains stability through the creation (or annihilation) of a stable or unstable limit cycle (a spatially uniform, temporally oscillating solution).

For convenience we will assume that the Hopf bifurcation occurs at $\mu = 0$ and that for $\mu < 0$ we have just the fixed point and that the limit cycle emerges from the fixed point for $\mu > 0$ since we can always arrange for these conditions to be met by a suitable transformation of the bifurcation parameter μ.

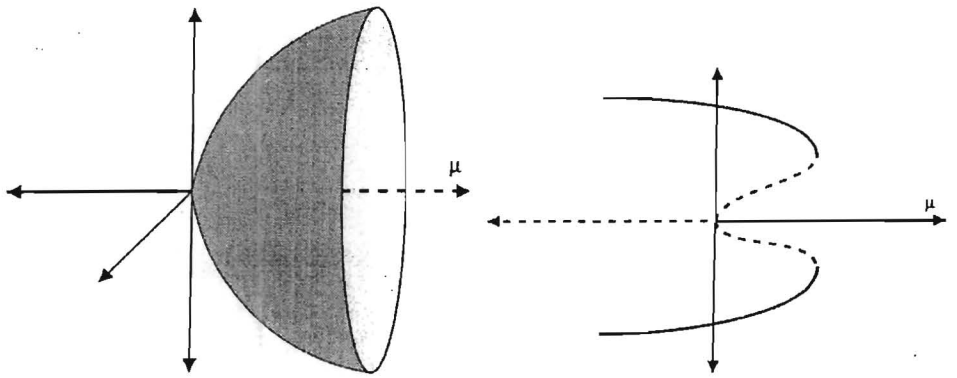

Figure 3.1: *On the left we have the bifurcation diagram for the supercritical Hopf bifurcation. For $\mu < 0$ we have a stable fixed point represented by the solid line. For $\mu > 0$ we have an unstable fixed point represented by the dashed line and a stable limit cycle represented by the shaded bowl. On the right we have the bifurcation diagram for the subcritial Hopf bifurcation. For clarity, only the solution branches lying on the vertical plane are shown. To obtain the actual bifurcation diagram, the graph should be rotated around the μ axis. Stable solution branches are shown as solid lines while unstable solution branches are shown as dashed lines. The outer stable limit cycle does not form part of the subcritical Hopf bifurcation (which occurs at $\mu = 0$), but in practice some mechanism (in this case the stable limit cycle) prevents the fields in the region $\mu < 0$ from blowing up to infinity. In both diagrams μ is the bifurcation parameter. The axes perpendicular to the μ axis form the phase space of the field. In practice the dimension of the phase space is likely to be greater than two.*

A *supercritical* Hopf bifurcation occurs when a stable fixed point becomes unstable through the creation of a stable limit cycle about the fixed point. According to our definition of μ, the fixed point is stable for $\mu < 0$. As μ increases from 0 a stable limit cycle emerges from the fixed point, growing in size as μ increases and leaving the unstable fixed point inside the limit cycle. The amplitude of the stable limit cycle is proportional to $\sqrt{\mu}$.

A *subcritical* Hopf bifurcation occurs when an unstable fixed point gains stability through the creation of an unstable limit cycle about the fixed point. As with the supercritical bifurcation the limit cycle expands from the fixed point as μ is increased from 0.

If we consider the subcritical Hopf bifurcation in reverse (by moving from positive to negative μ) we start with an unstable limit cycle about a stable fixed point. The limit cycle shrinks as μ decreases until suddenly the fixed point becomes unstable with no nearby stable orbits. This leads to a rapid and dramatic change in the behaviour of the field which can be particularly important in physical applications. This discontinuous change in the behaviour of the field is not present in the supercritical Hopf bifurcation.

Let us represent our field by N real variables $(X_1, X_2, \ldots, X_N) = \vec{X}$ and the spatially uniform stationary field configuration which is to undergo bifurcation

by $(A_1, A_2, \ldots, A_N) = \vec{A}$. The difference between the general field $\vec{X}$ and the specific configuration $\vec{A}$ we will label $\vec{x} = \vec{X} - \vec{A}$. At the Hopf bifurcation a pair of eigenvalues (complex conjugates of each other) of the uniform stationary solution cross the imaginary axis and A loses or gains stability. Call these eigenvalues λ and $\overline{\lambda}$. Since the real parts of λ and $\overline{\lambda}$ are zero at the Hopf bifurcation point, a small perturbation about A of the form of the eigenfunctions corresponding to λ and $\overline{\lambda}$ will neither grow nor decay. Such a perturbation is called neutrally stable.

If λ and $\overline{\lambda}$ are the only eigenvalues crossing the imaginary axis then all other eigenvalues must lie in the left half of the complex plane (have negative real part) because $\vec{A}$ is a stable solution on one side of the bifurcation. Thus all other perturbations will decay exponentially and solutions close to $\vec{A}$ may be approximated using only perturbations of the form of the eigenfunctions corresponding to λ and $\overline{\lambda}$ provided we wait for the fast transients to disappear.

If we write the eigenfunction associated with λ as α_ν and its contribution decays (or grows) as $e^{\lambda t}$, then the eigenfunction associated with $\overline{\lambda}$ is $\overline{\alpha_\nu}$ and its contribution decays as $e^{\overline{\lambda} t}$. At $\mu = 0$ we may write $\lambda = i\omega_0$ since the real part of λ is zero. Since the perturbation must be real (because the components of $\vec{X}$ are real), the general form of the pertubation is

$$x_\nu = W\alpha_\nu e^{\lambda t} + \overline{W}\,\overline{\alpha_\nu} e^{\overline{\lambda} t} \ , \tag{3.1}$$

where W is a complex constant.

When μ is small but not exactly equal to zero, we may assume that the form of the solution remains that of (3.1) with $\lambda = i\omega_0$ provided we let W become a slowly varying function of time. Equivalently, we may assume that the eigenfunctions of λ and $\overline{\lambda}$ remain the dominant contributions to solutions near $\vec{A}$ but that near $\mu = 0$ they vary proportionally to μ so that $\lambda = i\omega_0 + \mu\lambda_1$ where λ_1 is a complex constant. Comparing the results from the two approximations yields the equation

$$\dot{W} = \mu\lambda_1 W \ ,$$

which is accurate to first order in μ provided t does not become too large.

We next wish to consider that W might be a slowly varying function of the spatial variables. In this case we can write λ as a long wavelength (small wave number) expansion:

$$\lambda(k) = i\omega_0 + \mu\lambda_1 - Dk^2 \ .$$

Here D is a complex constant and k is the magnitude of the wave number. The real part of D must be positive since we assumed earlier that the spatially uniform solution (which corresponds to $k = 0$) makes the dominant contribution when $\mu = 0$. If Re $D < 0$ then when $\mu = 0$, $\lambda(k) = i\omega_0 - Dk^2$ which is a number with positive real part for $k \neq 0$ and there would be other, more quickly growing, unstable perturbations.

The effect of the long wavelength expansion is to modify the equation for the rate of change of W with time to include the extra term $D\nabla^2 W$:

$$\dot{W} = \mu\lambda_1 W + D\nabla^2 W \, .$$

We now decide on what nonlinear terms are appropriate to add. Since W is small we will only keep low order terms. Examining equation (3.1) with $\lambda = i\omega_0$ we see that the transformation $W \to We^{i\theta}$, $\theta \in \mathcal{R}$ corresponds to a time translation of the field $t \to t + \frac{\theta}{\omega_0}$. Since the original system is assumed to not be dependent on time explicitly and hence is invariant under such a time translation, the equations for W should be invariant under the transformation $W \to We^{i\theta}$. The lowest order nonlinear terms are W^2, $\overline{W}^2$, $|W|^2$, W^3, $\overline{W}^3$, $|W|^2 W$ and $|W|^2\overline{W}$. Of these only $|W|^2 W$ is invariant under the above transformation of W. Thus the general form of the (cubic) CGLE is

$$\dot{W} = \mu\lambda_1 W + D\nabla^2 W - g_1|W|^2 W \, .$$

The next term which can be included is $|W|^4 W$. Adding this term we obtain the cubic-quintic CGLE

$$\dot{W} = \mu\lambda_1 W + D\nabla^2 W - g_1|W|^2 W - g_2|W|^4 W \, .$$

We include the cubic-quintic CGLE here only for interest sake. The rest of our studies are confined to the cubic equation.

The cubic CGLE above has 3 complex parameters (namely λ_1, D and g_1) and one real parameter (μ). These may be reduced to 2 real parameters by rescaling the spatial variables, time and the amplitude, W.

The rescalings necessary are as follows:

1. Firstly, since $\mathrm{Re}\, D > 0$ we can perform the rescaling $\vec{x} \to \sqrt{\mathrm{Re}\, D}\,\vec{x}$ which results in the transformation of the operator $\nabla^2 \to \frac{1}{\mathrm{Re}\, D}\nabla^2$. After this rescaling the cubic CGLE has the form

$$\frac{\partial W}{\partial t} = \mu\lambda_1 W + \left(1 + i\frac{\mathrm{Im}\, D}{\mathrm{Re}\, D}\right)\nabla^2 W - g_1|W|^2 W \, . \tag{3.2}$$

2. Secondly, if we assume $\mathrm{Re}\, g_1 \neq 0$ then we may make the transformation $W \to \frac{1}{\sqrt{\mathrm{Re}\, g_1}} W$, after which the CGLE becomes

$$\frac{\partial W}{\partial t} = \mu\lambda_1 W + \left(1 + i\frac{\mathrm{Im}\, D}{\mathrm{Re}\, D}\right)\nabla^2 W \pm \left(1 + i\frac{\mathrm{Im}\, g_1}{\mathrm{Re}\, g_1}\right)|W|^2 W \, . \tag{3.3}$$

The $\pm$ sign in front of the last term is introduced as a consequence of the relation $|\sqrt{\mathrm{Re}\, g}|^2 = \pm \mathrm{Re}\, g$.

3. Thirdly, assuming that $\mathrm{Re}\,(\mu\lambda_1) \neq 0$ we can rescale t so that $t \to \frac{1}{\mathrm{Re}\,(\mu\lambda_1)}t$ upon which $\frac{\partial}{\partial t} \to \mathrm{Re}\,(\mu\lambda_1)\frac{\partial}{\partial t}$. This brings the CGLE to the form

$$\begin{aligned}\frac{\partial W}{\partial t} &= \left(1 + i\frac{\mathrm{Im}\,(\mu\lambda_1)}{\mathrm{Re}\,(\mu\lambda_1)}\right)W + \frac{1}{\mathrm{Re}\,(\mu\lambda_1)}\left(1 + i\frac{\mathrm{Im}\,D}{\mathrm{Re}\,D}\right)\nabla^2 W \\ &\quad \pm \frac{1}{\mathrm{Re}\,(\mu\lambda_1)}\left(1 + i\frac{\mathrm{Im}\,g_1}{\mathrm{Re}\,g_1}\right)|W|^2 W\,. \end{aligned} \tag{3.4}$$

4. If $\mathrm{Re}\,(\mu\lambda_1) > 0$ we can remove the factors of $\frac{1}{\mathrm{Re}\,(\mu\lambda_1)}$ with the transformations

$$\begin{aligned}\vec{x} &\to \frac{1}{\sqrt{\mathrm{Re}\,(\mu\lambda_1)}}\vec{x}\,, \\ W &\to \sqrt{\mathrm{Re}\,(\mu\lambda_1)}W\,. \end{aligned} \tag{3.5}$$

If $\mathrm{Re}\,(\mu\lambda_1) < 0$ we can remove factors of $-\frac{1}{\mathrm{Re}\,(\mu\lambda_1)}$ with the transformations

$$\begin{aligned}\vec{x} &\to \frac{1}{\sqrt{-\mathrm{Re}\,(\mu\lambda_1)}}\vec{x}\,, \\ W &\to \sqrt{-\mathrm{Re}\,(\mu\lambda_1)}W\,. \end{aligned} \tag{3.6}$$

Thus we obtain two standard forms for the CGLE

$$\frac{\partial W}{\partial t} = (1 + ic_0)W + (1 + ic_1)\nabla^2 W \pm (1 + ic_2)|W|^2 W \tag{3.7}$$

$$\frac{\partial W}{\partial t} = (1 + ic_0)W - (1 + ic_1)\nabla^2 W \pm (1 + ic_2)|W|^2 W\,, \tag{3.8}$$

where (3.7) is the form which applies when $\mathrm{Re}\,(\mu\lambda_1) > 0$ and (3.8) is the form which applies when $\mathrm{Re}\,(\mu\lambda_1) < 0$. Note that $\mathrm{Re}\,\lambda = \mathrm{Re}\,(\mu\lambda_1)$ so that equation (3.7) applies when the uniform stationary field configuration $\vec{A}$ is unstable, and equation (3.8) applies when $\vec{A}$ is stable. If $\mu > 0$ then equation (3.7) applies to a supercritical Hopf bifurcation and equation (3.8) to a subcritical Hopf bifurcation. If, on the other hand, $\mu < 0$ then equation (3.7) applies to a subcritical Hopf bifurcation and equation (3.8) to a supercritical one. The values of the parameters c_0, c_1 and c_2 in terms of the original parameters are:

$$c_0 = \frac{\mathrm{Im}\,\lambda_1}{\mathrm{Re}\,\lambda_1}\,, \qquad c_1 = \frac{\mathrm{Im}\,D}{\mathrm{Re}\,D}\,, \qquad c_2 = \frac{\mathrm{Im}\,g_1}{\mathrm{Re}\,g_1}\,. \tag{3.9}$$

The parameter c_0 may be removed by the transformation $W \to We^{ic_0 t}$, leaving the CGLE either in the form,

$$\frac{\partial W}{\partial t} = W + (1 + ic_1)\nabla^2 W \pm (1 + ic_2)|W|^2 W\,, \tag{3.10}$$

or in the form,

$$\frac{\partial W}{\partial t} = W - (1 + ic_1)\nabla^2 W \pm (1 + ic_2)|W|^2 W \,, \tag{3.11}$$

depending on whether $\mathrm{Re}\,(\mu\lambda_1) > 0$ (equation (3.10)) or $\mathrm{Re}\,(\mu\lambda_1) < 0$ (equation (3.11)).

In the field of optics (and in chapters 4 and 5 where we have followed the optics convention) the CGLE is written with a factor of i in front of $\frac{\partial W}{\partial t}$. If we multiply the original, unsimplified, form of the CGLE by i we obtain

$$i\frac{\partial W}{\partial t} = i\mu\lambda_1 W + iD\nabla^2 W - ig_1|W|^2 W \,. \tag{3.12}$$

Then after applying the same transformations as those used above in equations (3.2) - (3.8) but with μ, D and g_1 replaced by $i\mu$, iD and ig_1, respectively, we obtain

$$i\frac{\partial W}{\partial t} = (1 + i\tilde{c}_0)W \pm (1 + i\tilde{c}_1)\nabla^2 W \pm (1 + i\tilde{c}_2)|W|^2 W \,. \tag{3.13}$$

In order to apply the necessary transformations we have assumed that $\mathrm{Re}\,(ig_1) \neq 0$ and $\mathrm{Re}\,(i\mu\lambda_1) \neq 0$. One small complication arises in applying the transformations. Previously we started with the transformation $\vec{x} \to \sqrt{\mathrm{Re}\,D}\vec{x}$ since we had earlier required that $\mathrm{Re}\,D > 0$. After multiplying by i we must start either with the transformation $\vec{x} \to \sqrt{\mathrm{Re}\,(iD)}\,\vec{x}$ or $\vec{x} \to \sqrt{-\mathrm{Re}\,(iD)}\,\vec{x}$ since we have placed no constraints on the sign of $\mathrm{Re}\,(iD)$. Note that all four possible combinations of plus and minus signs may arise in equation (3.13).

The constants $\tilde{c}_i$ are given by

$$\begin{aligned}
\tilde{c}_0 &= \frac{\mathrm{Im}\,(i\lambda_1)}{\mathrm{Re}\,(i\lambda_1)} = -\frac{\mathrm{Re}\,\lambda_1}{\mathrm{Im}\,\lambda_1} \,, \\
\tilde{c}_1 &= \frac{\mathrm{Im}\,(iD)}{\mathrm{Re}\,(iD)} = -\frac{\mathrm{Re}\,D}{\mathrm{Im}\,D} \,, \\
\tilde{c}_2 &= \frac{\mathrm{Im}\,(ig_1)}{\mathrm{Re}\,(ig_1)} = -\frac{\mathrm{Re}\,g_1}{\mathrm{Im}\,g_1} \,.
\end{aligned} \tag{3.14}$$

The dependence on $\tilde{c}_0$ cannot be removed using the transformation used previously to remove c_0 since $W \to We^{\tilde{c}_0 t}$ does not, in general, leave $|W|$ invariant. However, the term W can be removed by the transformation $W \to We^{-it}$.

If we let $\tilde{c}_2 = 0$ and change parameters to $\gamma = -\tilde{c}_0$ and $c = -\tilde{c}_1$ then, after making the transformation $W \to \sqrt{2}W$, we obtain from equation (3.13) the undriven limit of the complex Ginburg-Landau equation which we study in chapters 4 and 5. We choose the negative sign in front of both $\nabla^2 W$ and $|W|^2 W$.

Note that the transformations used to obtain equations (3.2) - (3.8) and (3.13) may be applied even after a driving term proportional to $\bar{W}$ has been added to the orginal, unsimplified complex Ginzburg-Landau equation (3.1) since the transformations involve only real rescalings of x, t and W. The result will be the addition of the driving term to the simplified equations (3.7), (3.8) and (3.13).

This concludes the section on the undriven CGLE. We have seen how the CGLE may be constructed for the amplitude of modes excited at the Hopf bifurcation of a stationary configuration of a real vector field. The components of such a vector field might be the velocity potential and surface displacement, as is the case in the hydrodynamics of a fluid surface, or the electric and magnetic fields present in a laser, as is the case in optics. We have also seen how the original parameter set of the cubic Ginzburg-Landau equation, which consists of three complex parameters and one real parameter, may be reduced to a smaller set consisting of only two real parameters. This was done by rescaling time, the spatial variables and the amplitude. We now move on to examine the case when parametric driving is present.

3.2 Bifurcations with parametric driving

In [51] Elphick, Iooss and Tirapegui derive the normal form for the bifurcation (Hopf or saddle-node) of a stationary point of a periodically forced differential equation. They begin with an unforced evolution equation

$$Z_t = \mathcal{F}(\mu, Z) \tag{3.15}$$

where $Z \in \mathcal{R}^n$ and there are m parameters which are combined in the vector $\mu \in \mathcal{R}^m$. The system is assumed to have a critical point at $\mu = \vec{0}$ and that the Jacobian matrix, $\mathcal{L}_{ij} = \frac{\partial \mathcal{F}_i}{\partial Z_j}$, at the critical point has some eigenvalues with real part equal to zero and the rest with real parts strictly less than zero. The eigenvalues with real part equal to zero are the critical eigenvalues and the phase space spanned by their eigenvectors is the critical phase space E_0. The eigenvalues with real parts strictly less than zero are the non-critical eigenvalues and the space spanned by their eigenvectors is the non-critical phase space E_-. The spaces E_0 and E_- are invariant under the action of the operator $\mathcal{L}$ since they are spanned by sets of eigenfunctions of $\mathcal{L}$.

The unforced equation is then perturbed by adding a small periodic driving term which gives

$$Z_t = \mathcal{F}(\mu, Z) + \delta \mathcal{G}(\mu, Z, t)\,. \tag{3.16}$$

Here δ is the amplitude of the forcing and $\mathcal{G}$ is periodic in t with period T. This form of forcing is parametric driving. For example, the forcing present in the Faraday resonance experiment discussed in Chapter 2 is of this form (see equation (2.32)).

Since $\mathcal{F} + \delta\mathcal{G}$ is periodic in t with period T we can write Z as

$$Z = X + Y + \Phi(\mu, \delta, t, X, Y)\,, \tag{3.17}$$

where $X \in \mathrm{E}_0$, $Y \in \mathrm{E}_-$ and Φ is a function of μ, δ, t, X and Y and is periodic in t with period T. The contribution of $Y \in \mathrm{E}_-$ will decay away quickly as t progresses since the real part of all the eigenvalues of the modes spanning Y are less than zero. Thus after a short time we can write to good approximation

$$Z = X + \Phi(\mu, \delta, t, X)\,. \tag{3.18}$$

Substituting the expression for Z (3.18) into (3.16) it is possible to solve for $\frac{\mathrm{d}X}{\mathrm{d}t}$ and obtain

$$X_t = \mathcal{L}X + N(\mu, \delta, t, X) + \text{ higher order terms.} \tag{3.19}$$

Here N is the lowest-degree non-trivial polynomial in X and is periodic in time. The equation (3.19) without the higher order terms is called the normal form of equation (3.16). If N is allowed to be of higher degree that the lowest possible, an extension of the normal form is obtained when the remaining higher order terms are neglected. Such an extension may become applicable in the amplitude of the excited modes grows very large. The extension of the undriven CGLE is cubic-quintic CGLE.

Finding the explicit expression for the normal form requires Taylor expanding $\mathcal{F}$, $\mathcal{G}$, N and Φ in μ, δ and X and then equating powers of these variables. The series of equations resulting from equating powers is then projected firstly onto the non-critical subspace E_- and secondly onto the critical subspace E_0. The equations when projected onto the non-critical phase space may be solved by the method of the Laplace transform. The second set which arise after projection onto the critical phase space may be solved by means of the Fourier transform.

Elphick, Iooss and Tirapegui [51] apply the above technique to both the periodically forced saddle-node bifurcation of a stationary point of (3.16) and to the periodically forced Hopf bifurcation of such a stationary point (that is, the bifurcation of the stationary point to a limit cycle or ring of stationary points). Here "periodically forced bifurcation" refers to the bifurcation of a solution of the periodically forced system (3.16) at a point in the parameter space close to a bifurcation of the corresponding solution to the unforced system (3.15).

In the case of the saddle-node bifurcation the addition of periodic forcing does not alter the bifurcation dynamics significantly and the normal form remains that of an unforced saddle-node bifurcation. For a saddle-node bifurcation the dimension of the critical subspace is one, which is too small to allow the introduction of extra dynamics by the periodic forcing.

The situation is very different for the periodically forced Hopf bifurcation. If the eigenvalues of the marginal modes at the bifurcation point are $\pm i\omega_0$ (i.e. the modes are periodic with frequency ω_0) and the frequency of the periodic driving is ω ($\omega = \frac{2\pi}{T}$) then the ratio $\frac{\omega_0}{\omega}$ plays a crucial role in the dynamics of the bifurcation.

If $\frac{\omega_0}{\omega}$ is an integer then the normal form for the bifurcation remains that of an unforced Hopf bifurcation:

$$A_t = \mu A + a|A|^2 A + \text{ higher order terms}\,. \tag{3.20}$$

If $\frac{\omega_0}{\omega}$ is a rational number $\frac{r}{s}$ (with r and s having no common divisors other than 1) then the time invariance of the original system is broken and, as a result, the invariance of the normal form under complex rotations is broken. The new normal form is

$$A_t = \mu A + a|A|^2 A + \delta^M g_1 \overline{A}^{s-1} + \text{ higher order terms.} \tag{3.21}$$

Here g_1 and M are constants which depend on the exact form of the periodic forcing. This explains why so much theorectical analysis and experimental work are focused on the parameter range $\frac{\omega_0}{\omega} = \frac{1}{2}$. This choice of parameters results in a particularly simple form for the additional term since when $s = 2$, $\overline{A}^{s-1} = \overline{A}$.

Of course, an exact frequency ratio of $\frac{1}{2}$ is not experimentally obtainable. If $\frac{\omega_0}{\omega}$ is close to some rational number so that $\frac{\omega_0}{\omega} = \frac{r}{s} + \gamma$ where γ is some small parameter called the detuning parameter and r and s again have no non-trivial common factors then the resulting normal form is

$$A_t = (\mu + i\omega\gamma)A + a|A|^2 A + \delta^M g_1 \overline{A}^{s-1} + \text{ higher order terms,} \tag{3.22}$$

so the choice of $\frac{\omega_0}{\omega} \approx \frac{1}{2}$ (i.e. $s = 2$) still results in a simple form for the driving terms. The frequency ratio $\frac{\omega_0}{\omega}$ lies close to many rational numbers. Any rational number close to $\frac{\omega_0}{\omega}$ will give a valid normal form, provided $|\gamma| \ll 1$.

Elphick, Iooss and Tirapegui [51] also mention that the breaking of the continuous phase invariance by the addition of parametric driving results in the new system possessing discrete phase invariance under rotations of $\frac{2\pi}{s}$. Thus the commonly occuring π phase difference in the study of periodically driven Hopf bifurcations (for example: [24], [29] and [32]).

3.3 Summary

We have now finished the chapter exploring the manner in which the complex Ginzburg-Landau equation arises in parametrically driven and undriven systems.

In the case of the undriven systems we constructed the complex Ginzburg-Landay equation as the amplitude equation for excited modes near a Hopf bifurcation by consideration of the symmetries present in the original (nonlinear) physical system. We then reduced the number of parameters present in the amplitude equation from 3 complex parameters to 2 (or in some cases 3) real parameters by rescalings of the coordinates and the amplitude.

When considering the amplitude equation of a driven system, we saw that the periodic driving breaks the continuous time-translation symmetry of the physical

system and replaces it with a discrete symmetry, time periodicity, resulting in the addition of a new term to the amplitude equation. This new term depends on the ratio of the frequency of the modes excited at the Hopf bifurcation to the frequency of the periodic driving and is absent when this ratio is an integer. When the ratio is $\frac{1}{2}$ (i.e. the frequency of the forcing is twice that of the excited modes) the additional term is proportional to the complex conjugate of the amplitude.

For completeness, we mention that a more rigorous approach to both sections in this chapter would have been to apply the method of the centre manifold, as was done in [42].

In the next two chapters, chapters 4 and 5, we look for solutions of the parametrically driven complex Ginzburg-Landau by continuing known solutions of its damped-driven NLS limit.

Chapter 4

Pulse-like Solutions to the Parametrically Driven CGLE

4.1 Introduction

In the preceding chapter we saw how the parametrically-driven CGLE may arise in the description of the Hopf bifurcation of a solution of a driven physical system. In this chapter and the next we study a one-dimensional parametrically-driven cubic Ginzburg-Landau equation of the form:

$$i\psi_t + (1 - ic)\psi_{xx} + 2|\psi|^2\psi - (1 - i\gamma)\psi = h\overline{\psi}\,. \tag{4.1}$$

This is the parametrically driven extension of the form which is commonly used in optics (see for example [36]). In (4.1) the parameter h measures the amplitude of the parametric driving, γ the damping and c is the spectral filtering parameter. The effect of non-zero c is to damp out short wavelength oscillations. We will for the most part be interested in solutions which decay to the zero background either as $x \to \infty$ or $x \to -\infty$. If $\gamma < 0$ or $c < 0$ then the zero background solution is unstable. Thus we consider only the case where $\gamma \geq 0$ and $c \geq 0$. In addition, h may be chosen positive without loss of generality since making the transformation $\psi \to i\psi$ is equivalent to changing the sign of h.

The driven CGLE (4.1) possesses focusing nonlinearity and would arise at a subcritical Hopf bifurcation. When (4.1) is *undriven* (i.e. $h = 0$) then *stable* uniform zero and non-zero solutions would not coexist unless a higher-order nonlinear term was added (as was done by Thual and Fauve in [31]). However, when $h > 0$ the parametric driving may play an analogous role to that of a quintic (or higher order) nonlinear term and bring about the existence of stable non-zero uniform solutions in the subcritical region (where the uniform zero background is stable). The uniform background solutions to (4.1) are presented in section 4.2.

In the limit where $c = 0$ equation (4.1) becomes the parametrically driven damped NLS equation, which has explicit time-independent pulse-like solutions

[52] of the form

$$\psi_{\pm}(x,t) = A_{\pm}\,\mathrm{sech}\,(A_{\pm}x)\;e^{-i\theta_{\pm}}\,, \tag{4.2}$$

where A and θ are given by

$$A_{\pm} = \sqrt{1 \pm \sqrt{h^2-\gamma^2}} \quad ; \quad \cos 2\theta_{\pm} = \pm\sqrt{1-\frac{\gamma^2}{h^2}}\,. \tag{4.3}$$

The stability analysis for these two solutions was performed in [52]. The soliton ψ_- was found to be unstable for all h and γ, while ψ_+ is stable over a range of values of h and γ.

The aim of this chapter and the next is to analyze the existence and stability of localised solutions to the Ginzburg-Landau equation (4.1) by continuation from solutions to the damped driven NLS (where $c = 0$) and its undamped variant (where both $c = 0$ and $\gamma = 0$). Chapter 4 deals with pulse solutions while chapter 5 deals with fronts.

In the second section, 4.2, we show that the solutions $\psi_{\pm}$ to the damped driven nonlinear Schrödinger may be continued in c to solutions of the Ginzburg-Landau equation. We also examine the three flat background solutions to the Ginzburg-Landau equation, finding the parameter regions in which they are stable and in which decay to the flat backgrounds may occur.

In the third section, 4.3, we perform an adiabatic analysis on the soliton solutions $\phi_{\pm}$. The parameter c is allowed to be small but nonzero and the parameters A and θ in equation (4.2) are considered to be slowly varying functions of time. Evolution equations which are valid in the $c \ll 1$ parameter region of the driven CGLE are derived for A and θ.

In the fourth section, 4.4, we present the results of the numerical continuation of $\psi_{\pm}$ in c. New solutions to the Ginzburg-Landau equation are obtained. In section 4.5 we numerically analyze the stability of the solutions found in section 4.4 by examining the associated linearised eigenvalue problem.

4.2 Preliminaries

4.2.1 Flat backgrounds

The Ginzburg-Landau equation has 3 stationary flat solutions, namely $\psi = 0$ and $\psi = \phi_{\pm}$, where

$$\phi_{\pm} = \frac{1}{\sqrt{2}}A_{\pm}e^{-i\theta_{\pm}}, \tag{4.4}$$

with $A_{\pm}$ and $\theta_{\pm}$ as in equation (4.3). Note that the solutions $\phi_{\pm}$ are independent of c.

By linearising the stationary Ginzburg-Landau equation about $\psi_{\text{flat}} = \phi_{\pm}$ or 0, we can analyze the stability of the flat backgrounds and determine when decay

to the flat backgrounds can occur. Letting $\psi = \psi_{\text{flat}} + \delta\psi$ gives

$$\mathcal{H}\delta\psi = 0, \tag{4.5}$$

where $\mathcal{H}$ is given by

$$\begin{aligned} \mathcal{H} &= (1 - \partial_{xx})\, I + (c\partial_{xx} - \gamma)\, J \\ &\quad + \begin{pmatrix} h - 6u^2 - 2v^2 & -4uv \\ -4uv & -h - 6v^2 - 2u^2 \end{pmatrix} . \end{aligned} \tag{4.6}$$

Here I is the unit matrix and $J = \begin{pmatrix} 0 & -1 \\ 1 & 0 \end{pmatrix}$. The functions u and v are defined by $u + iv = \phi_\pm$ or 0. The same operator $\mathcal{H}$ arises when linearising about an arbitrary solution $\psi_s = u + iv$.

The operator $\mathcal{H}$ and the operators $L_\pm$ given by (4.27) are related. $\mathcal{H}$ is obtained by linearising the Ginzburg-Landau equation about a solution $u + iv = \psi$ while the operators $L_\pm$ are obtained by linearising the damped driven NLS equation about the solutions $\psi_\pm$. Evaluating $\mathcal{H}$ when $c = 0$ and $\psi = \psi_\pm$ will give $L_\pm$ up to the transformation $\psi = \phi e^{-i\theta_\pm}$ which we have used to bring $L_\pm$ into a standard form.

Assuming a perturbation of the form $\delta\psi = (a+ib)e^{i(\omega t - kx)}$, gives a (complex) matrix equation which has non-trivial solutions if the determinant of the matrix is zero. At this stage we can either solve for ω in terms of k, or set $\omega = 0$ and solve for k. The first will allow us to determine the stability of the flat backgrounds while the second will allow us to determine when decay to the flat backgrounds can occur.

Stability of the flat backgrounds

Solving for ω in terms of k results in the expression

$$i\omega = -(ck^2 + \gamma) \pm i\sqrt{Z}\ , \tag{4.7}$$

where

$$Z = \left(1 - 2A^2 + k^2\right)^2 + A^2\left(A^2 - 2\right) - h^2\ . \tag{4.8}$$

Here A is one of $A_\pm$ or 0 depending on which solution we have linearised about. The flat background is stable if $\text{Re}(i\omega) \leq 0$ for all k and unstable otherwise. In the case of the zero background ($A = 0$) equation (4.7) simplifies considerably. In this case $i\omega$ will have the greatest real part when $k = 0$. Thus the stability of the zero background does not depend on c (as long as $c \geq 0$) and it will be stable when $Z|_{k=0} \geq -\gamma^2$, i.e.

$$h^2 \leq 1 + \gamma^2\ . \tag{4.9}$$

□

Consider now the flat nonzero backgrounds. The $\phi_\pm$ solutions will be stable when either $Z \geq 0$, or when $-(ck^2+\gamma)^2 \leq Z < 0$. These can be combined into a single condition $Z \geq -(ck^2+\gamma)^2$ which must hold for all real k. This condition amounts to the inequality

$$\left(1+c^2\right)s^2 + 2\left(1-2A^2+\gamma c\right)s + 4A^2\left(A^2-1\right) \geq 0 \tag{4.10}$$

where

$$s = k^2\,, \tag{4.11}$$

which must be true for all real k.

Since $A^2 < 1$ for ϕ_-, the inequality (4.10) does not hold for $k=0$ and hence ϕ_- is unstable for all γ, h and c.

□

For ϕ_+ we have $A^2 \geq 1$. Since the coefficient of s^2 in the quadratic on the left hand side of inequality (4.10) is positive the quadratic will be concave up. In addition, the coefficient of s^0 is non-negative thus the real roots (if they exist) of the quadratic in (4.10) will either have the same sign or one of them will be zero. Inequality (4.10) will hold for all real k if it holds for all $s \geq 0$, i.e. when the roots of the quadratic in s are negative, zero, complex, or equal. Since the coefficient of s^2 is positive the sign of the roots (or of the nonzero zero root) depends only on the sign of the coefficient of the term linear in s. The real roots (if they exist) will be negative or zero when

$$c \geq \frac{2A_+^2-1}{\gamma} \equiv c_0 > 0\,. \tag{4.12}$$

If the roots are complex the solution ϕ_+ will be stable, so ϕ_+ is stable whenever c obeys inequality (4.12), regardless of whether or not the roots are real. We now turn to the case when the roots are equal or complex which occurs when the discriminant of quadratic (4.10) is less than or equal to zero. The discriminant will be less than or equal to zero when

$$\left[\gamma^2 - 4A_+^2\left(A_+^2-1\right)\right]c^2 + \left[2\left(1-2A_+^2\right)\gamma\right]c + 1 \leq 0\,. \tag{4.13}$$

[We immediately note that when $c=0$ the solution ϕ_+ is unstable for all h and γ since neither (4.12) nor (4.13) will hold. Setting $c=0$ in (4.12) gives the inequality $0 \geq \frac{1}{\gamma}$ (after using $A_+^2 \geq 1$) while setting $c=0$ in (4.13) gives the inequality $1 \leq 0$, both of which are false.]

The discriminant of the quadratic expression in c (4.13) is equal to

$$4A_+^2\left(A_+^2-1\right)\left(1+\gamma^2\right) \tag{4.14}$$

which is positive, thus the quadratic in (4.13) has real roots:

$$c_\pm = \frac{\left(2A_+^2-1\right)\gamma}{\gamma^2 - 4A_+^2\left(A_+^2-1\right)} \pm \frac{\sqrt{4A_+^2\left(A_+^2-1\right)\left(1+\gamma^2\right)}}{\gamma^2 - 4A_+^2\left(A_+^2-1\right)} \tag{4.15}$$

When $h^2 > \frac{1}{4}\left(\sqrt{1-\gamma^2}-1\right)^2+\gamma^2$, the coefficient of c^2 in the quadratic is negative. Thus the graph of the quadratic is concave down and the quadratic's roots have opposite sign (since the constant part of the quadratic is positive). The ϕ_+ solution is stable for $c \geq c_-$, the positive root of the quadratic, which is given in equation (4.15).

When $h^2 < \frac{1}{4}\left(\sqrt{1+\gamma^2}-1\right)^2+\gamma^2$, the graph of the quadratic is concave up and the quadratic's roots have the same sign (since the constant part of the quadratic is positive). Both the quadratic's roots are positive since the first term in the expression for the roots, equation (4.15), is positive. The ϕ_+ solution is stable only for $c_- \leq c \leq c_+$.

Lastly, when $h^2 = \frac{1}{4}\left(\sqrt{1+\gamma^2}-1\right)^2+\gamma^2$, the coefficient of c^2 is zero and the graph of (4.13) is a straight line. The ϕ_+ solution is stable for $c \geq \frac{1}{2\gamma\left(2A_+^2-1\right)}$.

The 3 cases may be collapsed into one: in the second case c_+ is always greater than c_0 so that, in view of (4.12), the second case reduces to $c \geq c_-$. In the third case $\frac{1}{2\gamma\left(2A_+^2-1\right)}$ is the limit as $h^2 \to \frac{1}{4}\left(\sqrt{1+\gamma^2}-1\right)^2+\gamma^2$ of c_-. So all three cases reduce to the same inequality, provided that the limit of c_- is taken if necessary. Consequently, ϕ_+ is stable when c is greater than the smaller of c_0 and c_-. We will show that $c_- < c_0$.

If $\gamma^2 < 4A_+^2(A_+^2-1)$, as in the first of the three cases above, then $c_- < c_0$ if $4A_+^2(A_+^2-1)(2A_+^2-1)^2 > \gamma^2(1+\gamma^2)$. Using the inequality $\gamma^2 < 4A_+^2(A_+^2-1)$ we can show that

$$\begin{aligned} 4A_+^2(A_+^2-1)(2A_+^2-1)^2 &> \gamma^2(2A_+^2-1)^2 \\ &= \gamma^2\left[4A_+^2(A_+^2-1)+1\right] \\ &> \gamma^2(1+\gamma^2)\,. \end{aligned} \tag{4.16}$$

If, on the otherhand, $\gamma^2 > 4A_+^2(A_+^2-1)$, as in the first of the three cases above, then $c_- < c_0$ if $4A_+^2(A_+^2-1)(2A_+^2-1)^2 < \gamma^2(1+\gamma^2)$. We may prove this by following a similar procedure to that used in (4.16) but in this case the inequality signs will be reversed.

Lastly, if $\gamma^2 = 4A_+^2(A_+^2-1)$, as in the third case above, then $c_- \to \frac{1}{2\gamma(2A_+^2-1)}$. Thus $c_- < c_0$ if $\frac{1}{2} < (2A_+^2-1)^2$, which it is since $A_+^2 \geq 1$.

Résumé

In conclusion, given that h, γ and c are positive, the stability properties of the flat backgrounds are as follows:

- *$\phi = 0$ is stable when $h^2 \leq 1 + \gamma^2$.*
- *ϕ_- is unstable for all h, γ and c.*
- *ϕ_+ is stable when $h^2 \leq 1 + \gamma^2$ and $c \geq c_-$, where c_- is given by (4.15).*

Existence of localised solutions: Decay to the flat backgrounds

If a localised disturbance is to exist on a flat background, it must be possible for a solution to approach the flat background as $x \to \pm\infty$. If such an approach is possible, we say that the solution can decay to the flat background. By setting $\omega = 0$ in equation (4.7) we can solve for k and determine when decay to the solutions $\phi_\pm$ can occur. Setting $\omega = 0$ results in a biquadratic

$$\left(1 + c^2\right) s^2 + 2\left(2A^2 - 1 - \gamma c\right) s + 4A^2\left(A^2 - 1\right) = 0 \tag{4.17}$$

where

$$s = (ik)^2 \,. \tag{4.18}$$

Decay to $\phi_\pm$ will be possible unless $\mathrm{Re}(ik) = 0$ for all four roots which occurs when both roots, $s_{1,2}$, of (4.17) are real and non-positive. Thus decay to $\phi_\pm$ can occur either when the roots of the quadratic (4.17) are complex (the discriminant is less than zero) or when one of the roots is positive. The discriminant of (4.17) is given by

$$\left(2A^2 - 1 - \gamma c\right)^2 - 4A^2\left(A^2 - 1\right)\left(1 + c^2\right) \,. \tag{4.19}$$

For ϕ_- the discriminant is always greater than zero as $A^2 < 1$ making the discriminant a sum of two positive quantities. However, the coefficient of s^2 is positive so the graph of the quadratic is concave up and it then follows that the roots have opposite sign since the constant term in the quadratic is negative. Thus decay to ϕ_- may occur for all h, γ and c.

In the case of ϕ_+ the quadratic (4.17) will have a positive real root when the inequality (4.12) is satisfied but not saturated. This occurs since the biquadratics in equations (4.10) and (4.17) are related by the simple transformation $s \to -s$. Similarly, quadratic (4.17) will have complex roots when the inequality (4.13) is satisfied but not saturated. Thus decay to ϕ_+ can occur when either inequality (4.12) or (4.13) is satisfied but not saturated.

Setting both $A = 0$ and $\omega = 0$ in equation (4.7) we can determine when decay to the zero background can occur. Setting $A = 0$ and $\omega = 0$ gives

$$\left(1 + c^2\right) s^2 - 2\left(1 + \gamma c\right) s - \left(h^2 - \gamma^2\right) = 0 \tag{4.20}$$

where

$$s = (ik)^2 \tag{4.21}$$

As before decay to the flat background will be possible when the quadratic for s has a negative discriminant or a positive root. Since the biquadratic has a positive turning point it has a positive root if the discriminant is non-negative. Thus decay to the zero flat background is possible for all h, γ and c.

Résumé

In summary, given that h, γ and c are positive, decay to the flat backgrounds can occur as follows:

- *Decay can occur to $\psi = 0$ for all h, γ and c.*
- *Decay can occur to ψ_- for all h, γ and c.*
- *Decay can occur to ψ_+ when $h^2 \leq 1 + \gamma^2$ and $c > c_-$.*

4.2.2 Continuability of $\psi_\pm$

We consider $\psi_\pm$ given by equation (4.2) which are stationary solutions to the Ginzburg-Landau equation (4.1) when $c = 0$. We wish to determine whether $\psi_\pm$ can be continued to stationary solution with non-zero c.

We start by substituting $\psi = \phi e^{-i\theta}$ into equation (4.1), restricting ourselves to the case $\psi_t = 0$. Here θ is a constant which we will choose later to simplify our calculations. After applying the transformation, equation (4.1) becomes an equation for ϕ:

$$(1 - ic)\,\phi_{xx} + 2\,|\phi|^2\,\phi - (1 - i\gamma)\,\phi = h\bar{\phi}e^{2i\theta}\,. \tag{4.22}$$

Assuming $c \ll 1$, we expand ϕ in powers of c:

$$\phi = \phi_0 + c\phi_1 + c^2\phi_2 + \ldots \tag{4.23}$$

Having done so we substitute this expansion into equation (4.22) and match like powers of c. Matching the constant terms results in the requirement that ϕ_0 be a solution to equation (4.22). Matching the c^1 terms gives the equation

$$\phi_1'' + 4\,|\phi_0|^2\,\phi_1 + 2\phi_0^2\bar{\phi}_1 - (1 - i\gamma)\,\phi_1 - h\bar{\phi}_1 e^{2i\theta} = i\phi_0'' \tag{4.24}$$

where $'$ indicates a derivative with respect to x. We now choose θ to be θ_+ for ψ_+ and θ_- for ψ_-. This makes ϕ_0 real. Decomposing ϕ_1 as

$$\phi_1 = u + iv\,, \tag{4.25}$$

equation (4.24) becomes

$$L_{\pm}\begin{pmatrix} u \\ v \end{pmatrix} = \begin{pmatrix} 0 \\ -\phi_0'' \end{pmatrix} \tag{4.26}$$

where

$$L_{\pm} = \begin{pmatrix} -\partial_x^2 + 1 - 6\phi_0^2 + h\cos 2\theta_{\pm} & \gamma + h\sin 2\theta_{\pm} \\ -\gamma + h\sin 2\theta_{\pm} & -\partial_x^2 + 1 - 2\phi_0^2 - h\cos 2\theta_{\pm} \end{pmatrix} \tag{4.27}$$

and the plus and minus subscripts indicate whether we are checking the continuability of ψ_+ or ψ_-. Simplifying $L_{\pm}$ using the fact that $\gamma = h\sin 2\theta_{\pm}$ results in

$$L_{\pm} = \begin{pmatrix} -\partial_x^2 + 1 - 6\phi_0^2 + h\cos 2\theta_{\pm} & 2\gamma \\ 0 & -\partial_x^2 + 1 - 2\phi_0^2 - h\cos 2\theta_{\pm} \end{pmatrix}. \tag{4.28}$$

Fredholm's alternative states that equation (4.26) for u and v has bounded solutions if and only if the right-hand side is orthogonal to the kernel of $L_{\pm}^{\dagger}$ (the adjoint of $L_{\pm}$). Thus we need to find the kernel of $L_{\pm}^{\dagger}$ to determine when $\psi_{\pm}$ will be continuable to non-zero c. The kernel of $L_{\pm}^{\dagger}$ is spanned by solutions of

$$L_{\pm}^{\dagger}\begin{pmatrix} a \\ b \end{pmatrix} = 0\,, \tag{4.29}$$

where $L_{\pm}^{\dagger}$ is given by

$$L_{\pm}^{\dagger} = \begin{pmatrix} -\partial_x^2 + 1 - 6\phi_0^2 + h\cos 2\theta_{\pm} & 0 \\ 2\gamma & -\partial_x^2 + 1 - 2\phi_0^2 - h\cos 2\theta_{\pm} \end{pmatrix} \tag{4.30}$$

and may be converted to a more familiar form by changing variables to $\xi = A_{\pm}x$, where we choose A_+ if we are considering ψ_+ and A_- if we are considering ψ_-. After substituting in the value of $\phi_0 = A_{\pm}\mathrm{sech}\,(A_{\pm}x)$, dividing through by $A_{\pm}^2$ and using the fact that $A_{\pm}^2 = 1 + h\cos 2\theta_{\pm}$, equation (4.29) becomes

$$\begin{pmatrix} L_1 & 0 \\ 2\gamma & L_0 - \epsilon_{\pm} \end{pmatrix}\begin{pmatrix} a \\ b \end{pmatrix} = 0\,, \tag{4.31}$$

where

$$\begin{aligned} L_0 &= -\partial_\xi^2 + 1 - 2\mathrm{sech}^2\xi\,, \\ L_1 &= -\partial_\xi^2 + 1 - 6\mathrm{sech}^2\xi \end{aligned}$$

and

$$\epsilon_{\pm} = 2\frac{A_{\pm}^2 - 1}{A_{\pm}^2} = \pm 2\,\frac{\sqrt{h^2 - \gamma^2}}{1 \pm \sqrt{h^2 - \gamma^2}}\,. \tag{4.32}$$

If $(a,b)^T$ satisfies (4.31), then a and b must satisfy the equations

$$L_1 a = 0 \qquad \text{and}$$

$$(L_0 - \epsilon_\pm)\, b = -2\gamma a\,.$$

If $a = 0$ then b is a zero mode of $L_0 - \epsilon_\pm$, and the null vector $(a,b)^T$ exists if and only if $L_0 - \epsilon_\pm$ has a zero mode. If $a \neq 0$ then b may be found provided $L_0 - \epsilon_\pm$ is invertible.

L_1 has only a single zero mode, namely $\partial_\xi\,(\operatorname{sech}\xi)$, and its smallest eigenvalue is -3 which is associated with the eigenvector $\operatorname{sech}^2\xi$. The continuous spectrum of L_1 begins at 1. Thus if a is a zero mode of L_1 it must be a multiple of $\partial_\xi\,(\operatorname{sech}\xi)$.

The smallest eigenvalue of L_0 is 0 which corresponds to the zero mode $\operatorname{sech}\xi$. The continuous spectrum of L_0 starts at 1. The eigenvalues of $(L_0 - \epsilon_\pm)$ are just those of L_0 shifted by an amount $\epsilon_\pm$. Thus $L_0 - \epsilon_\pm$ will be invertible so long as $\epsilon_\pm < 1$ and $\epsilon_\pm \neq 0$. Indeed, ϵ_+ is less than 1 when the zero background of the Ginzburg-Landau is stable ($h^2 - \gamma^2 < 1$) and greater than zero except when $h = \gamma$. For ϵ_- we have that ϵ_- is less than zero except when $h = \gamma$. When $h = \gamma$, $\epsilon_\pm = 0$. Thus $L_0 - \epsilon_\pm$ is invertible except in the special case where $A_\pm^2 = 1$ which is the line $h = \gamma$ in the parameter space on which the solutions $\psi_\pm$ are born (or cease to exist).

For the case $h \neq \gamma$ there is only one zero mode of $L_\pm^\dagger$, namely

$$\begin{pmatrix} a \\ b \end{pmatrix} = \begin{pmatrix} \partial_\xi\,(\operatorname{sech}\xi) \\ -2\,\gamma\,(L_0 - \epsilon_\pm)^{-1}\,\partial_\xi\,(\operatorname{sech}\xi) \end{pmatrix}, \tag{4.33}$$

since in this case $L_0 - \epsilon_\pm$ is invertible which implies that a must be a zero mode of L_1 (since b cannot be a zero mode of $L_0 - \epsilon_\pm$).

For the case $h = \gamma$ there is also only one zero mode of $L_\pm^\dagger$, namely

$$\begin{pmatrix} a \\ b \end{pmatrix} = \begin{pmatrix} 0 \\ \operatorname{sech}\xi \end{pmatrix}, \tag{4.34}$$

since in this case $L_0 - \epsilon_\pm$ is not invertible which implies that $a = 0$ and b is the zero mode of $L_0 - \epsilon_\pm = L_0$.

All that remains is to check that the zero modes, (4.33) and (4.34), for each case are orthogonal to the right hand side of equation (4.26). To this end, we note that in the case $h \neq \gamma$, b is an odd function of ξ (and thus of x) since $\partial_\xi\,(\operatorname{sech}\xi)$ is odd and $(L_0 - \epsilon_\pm)^{-1}$ must map odd functions to odd functions since $(L_0 - \epsilon_\pm)$ maps odd functions to odd functions. We also note that ϕ_0'' is an even function of x. Thus

$$< \begin{pmatrix} 0 \\ -\phi_0'' \end{pmatrix}, \begin{pmatrix} a \\ b \end{pmatrix} > \;= \int_{-\infty}^{\infty} (-\phi_0'' b)\, dx \;=\; 0 \tag{4.35}$$

and the continuability condition for the continuation of $\psi_\pm$ in the parameter c is satisfied when $h \neq \gamma$.

For the case when $h = \gamma$ we have

$$\begin{aligned}
< \begin{pmatrix} 0 \\ -\phi_0'' \end{pmatrix}, \begin{pmatrix} a \\ b \end{pmatrix} > &:= \int_{-\infty}^{\infty} (-\phi_0'' b)\ dx \\
&:= \int_{-\infty}^{\infty} A_{\pm}^3 \mathrm{sech}\,(A_{\pm}x)\left[2\,\mathrm{sech}^2(A_{\pm}x) - 1\right] \mathrm{sech}\,(A_{\pm}x)\ dx \\
&:= \int_{-\infty}^{\infty} (2\,\mathrm{sech}^4 x - \mathrm{sech}^2 x)\ dx \\
&:= \frac{1}{3}\int_{-\infty}^{\infty} \mathrm{sech}^2 x\ dx \\
&\neq 0\,.
\end{aligned}$$

Thus the continuability condition is not satisfied when $h = \gamma$.

As a result we expect to be able to continue the solutions $\psi_{\pm}$ into the parameter region where c is nonzero provided $h \neq \gamma$. This expectation is born out by our results in section 4 4 which presents the outcome of numerically continuing $\psi_{\pm}$ in c.

4.2.3 The $|c| \to \infty$ limits

If we rescale x by performing a change of variables to $X = \frac{x}{\sqrt{c}}$ then equation (4.1) becomes

$$i\psi_t + (\frac{1}{c} - i)\psi_{XX} + 2|\psi|^2\psi - (1 - i\gamma)\psi = h\bar{\psi}\,. \tag{4.36}$$

In the limit where $c \to \infty$ the equation above simplifies to

$$i\psi_t - i\psi_{XX} + 2|\psi|^2\psi - (1 - i\gamma)\psi = h\bar{\psi}\,. \tag{4.37}$$

For large c we expect that the solutions to (4.1) will be solutions of (4.37) which have been stretched (in the x-direction) by a factor of $\sqrt{c}$. When continuing a solution of (4.1) in c, with $c \gg 1$, we thus expect that the dominant change will be a simple stretching of the solution profile.

If, on the other hand, we examine the limit as $c \to -\infty$, then we may change variables to $X = \frac{x}{\sqrt{-c}}$ and arrive at the equation

$$i\psi_t + i\psi_{XX} + 2|\psi|^2\psi - (1 - i\gamma)\psi = h\bar{\psi}\,, \tag{4.38}$$

which is an approximation of (4.1) in this limit. The equation above differs from (4.37) only by sign in front of the $i\psi_{XX}$ term. Thus for large negative c we again expect that the solution profile will be stretched – this time as c is made more negative. However, for large negative c the overall solution profile will be determined by equation (4.38), not (4.37).

4.3 Adiabatic analysis

As we have already mentioned, when $c = 0$ the equation

$$i\psi_t + (1 - ic)\,\psi_{xx} + 2\,|\psi|^2\,\psi - (1 - i\gamma)\psi \;=\; h\overline{\psi} \tag{4.39}$$

admits solutions of the form

$$\psi \;=\; A\,\mathrm{sech}\,(Ax)\,e^{-i\theta}\,, \tag{4.40}$$

where A and θ are constants. For $c \neq 0$ we may find approximate solutions by assuming that ψ remains of the form (4.40) but that A and θ may vary with t. In the limit where $c \to 0$ the approximate solutions will become exact solutions.

When $c = 0$, ψ_t is zero. For small c, ψ_t should thus be small provided ψ (consider as a function of x only) has a form close to that of the $c = 0$ stationary solution. The approximation may fail if c becomes large or if the form of ψ evolves to become far from the $c = 0$ stationary solution.

To obtain an equation for $\dot{A}$ (the derivative of A with respect to t) we multiply (4.39) by $\overline{\psi}$, take the result's complex conjugate and subtract the two, getting the equation

$$\begin{aligned} i\left(\dot{\psi}\overline{\psi} + \dot{\overline{\psi}}\psi\right) + \left(\psi_{xx}\overline{\psi} - \overline{\psi_{xx}}\psi\right) - ic\left(\psi_{xx}\overline{\psi} + \overline{\psi_{xx}}\psi\right) + 2i\gamma\,|\psi|^2 \\ = h\left(\overline{\psi}^2 - \psi^2\right). \end{aligned} \tag{4.41}$$

Substituting the ansatz (4.40) into (4.41), integrating over x and using the boundary conditions $\psi_x \to 0$ as $|x| \to \infty$ results in the equation for $\dot{A}$:

$$\dot{A} \;=\; 2Ah\sin 2\theta - 2\gamma A - 2\tilde{c}A^3\,, \tag{4.42}$$

where the parameter $\tilde{c} = \frac{1}{3}c$.

In order to find a similar equation for $\dot{\theta}$ we multiply (4.39) by $\overline{\psi}$, take the result's complex conjugate and add the two, obtaining the equation

$$\begin{aligned} i\left(\dot{\psi}\overline{\psi} - \dot{\overline{\psi}}\psi\right) + \left(\psi_{xx}\overline{\psi} + \overline{\psi}_{xx}\psi\right) + ic\left(\overline{\psi}_{xx}\psi - \psi_{xx}\overline{\psi}\right) + 4\,|\psi|^4 - 2\,|\psi|^2 \\ = h\left(\overline{\psi}^2 - \psi^2\right). \end{aligned} \tag{4.43}$$

Substituting (4.40) into (4.43), integrating over x and using the boundary conditions $\psi_x \to 0$ as $|x| \to \infty$, results in the equations for $\dot{\theta}$:

$$\dot{\theta} \;=\; h\cos 2\theta + 1 - A^2\,. \tag{4.44}$$

Equations (4.42) and (4.44) form a system of ordinary differential equations for A and θ. The solutions to this system will give us approximate solutions to the Ginzburg-Landau equation. In particular, the stationary points of the system will give us approximate stationary solutions of the Ginzburg-Landau equation.

4.3.1 Stationary points

The stationary points of the system of equations (4.42) and (4.44) occur when $\dot{A} = \dot{\theta} = 0$ which gives the equations

$$h \sin 2\theta = \tilde{c}A^2 + \gamma \,, \tag{4.45}$$

$$h \cos 2\theta = A^2 - 1 \,. \tag{4.46}$$

Squaring both sides of (4.45) and (4.46) and adding gives

$$\left(1 + \tilde{c}^2\right) A^4 + 2\left(\gamma\tilde{c} - 1\right) A^2 + \left(1 + \gamma^2 - h^2\right) = 0 \,, \tag{4.47}$$

a biquadratic for A, which has solutions

$$A^2_{\pm} = \frac{(1 - \gamma\tilde{c}) \pm \sqrt{(1 - \gamma\tilde{c})^2 + (1 + \tilde{c}^2)\left(h^2 - \gamma^2 - 1\right)}}{1 + \tilde{c}^2} \,. \tag{4.48}$$

Using the results above for A we solve for θ and find

$$\theta_{\pm} = \tfrac{1}{2} \cos^{-1} \frac{A^2_{\pm} - 1}{h} \,. \tag{4.49}$$

However, we must still determine when the solutions for A^2 are real and non-negative. We are only interested in the parameter region for which the zero background solution of (4.39) is stable, i.e. $h^2 - \gamma^2 \leq 1$, and will restrict our analysis to this region.

The second term under the square root in (4.48) is negative in the region where the zero background is stable. Thus if $1 - \gamma\tilde{c} \geq 0$ and A^2 is real then both solutions for A^2 given by (4.48) are non-negative. Conversely, if $1 - \gamma\tilde{c} \leq 0$ and A^2 is real then both solutions for A^2 are negative. Since we are interested in finding the parameter region in which A^2 is real, the condition $1 - \gamma\tilde{c} \geq 0$ will give us the subregion where the solutions for A^2 are also non-negative.

What remains to be determined is for which values of c, γ and h the solutions A^2 in (4.48) are real. The solutions A^2 are real if the expression under the square root in (4.48) is positive, namely when

$$\left(h^2 - 1\right)\tilde{c}^2 - 2\gamma\tilde{c} + \left(h^2 - \gamma^2\right) \geq 0 \,. \tag{4.50}$$

The discriminant of the quadratic in $\tilde{c}$ on the left hand side of (4.50) is positive for all h and γ in the parameter region where the zero background is stable. Thus the roots of the quadratic in (4.50) are real and given by

$$\tilde{c}_{\pm} = \frac{\gamma \pm \sqrt{h^2\left(1 + \gamma^2 - h^2\right)}}{h^2 - 1} \,. \tag{4.51}$$

When $h^2 - 1 > 0$, the quadratic (4.50) is concave up and both $\tilde{c}_+$ and $\tilde{c}_-$ have the same sign since the constant term in the quadratic (4.50) is positive. Since $\tilde{c}_+$ is positive, both $\tilde{c}_+$ and $\tilde{c}_-$ are positive. (Alternatively, one can use Viet's theorem: since the coefficient of the linear term is negative and the free term positive, both the sum and the product of the two roots are positive which implies that $\tilde{c}_+ > \tilde{c}_- > 0$). Thus A^2 is real when $\tilde{c} \leq \tilde{c}_-$ or $\tilde{c} \geq \tilde{c}_+$.

When $h^2 - 1 < 0$, the quadratic (4.50) is concave down and the roots have opposite sign since the constant term in the quadratic (4.50) is positive. Thus, in this case, A^2 is real when $\tilde{c}_+ \leq \tilde{c} \leq \tilde{c}_-$.

Lastly when $h^2 - 1 = 0$, the quadratic becomes linear and inequality (4.50) yields the information that A^2 is real when $\tilde{c} \leq \frac{1-\gamma^2}{2\gamma}$. This is the limit (as $h \to 1$) of $\tilde{c}_-$.

We have determined when A^2 is real and when A^2 is non-negative. We must now determine in which region of the parameter space both conditions hold simultaneously. A necessary condition for A^2 to be non-negative is $1 - \gamma\tilde{c} \geq 0$ which may be rewritten as $\tilde{c} \leq \frac{1}{\gamma}$. In order to determine in which part of the parameter space A^2 is both real and non-negative it will be necessary to determine whether $\tilde{c}_\pm$ are greater than or less than $\frac{1}{\gamma}$.

When $h^2 - 1 > 0$, $\tilde{c}_+$ is greater than $\frac{1}{\gamma}$ since replacing the $h^2 - 1$ in the denominator of (4.51) with γ^2 and using the inequality $h^2 - 1 \leq \gamma^2$ (which must hold for the zero solution to be stable) we get $\tilde{c}_+ \geq \frac{1}{\gamma} + \textit{positive terms}$.

When $h^2 - 1 < 0$, $\tilde{c}_+$ is negative since the numerator of (4.51) is positive while the denominator is negative.

When $h^2 - 1 > 0$, $\tilde{c}_-$ is less than $\frac{1}{\gamma}$. We show this as follows:

$$\begin{array}{lrcl}
 & \tilde{c}_- & \leq & \frac{1}{\gamma} \\
\text{amounts to} & \frac{\gamma - \sqrt{h^2(1+\gamma^2-h^2)}}{h^2-1} & \leq & \frac{1}{\gamma} \\
\text{and also} & \gamma^2 - h^2 + 1 & \leq & \gamma\sqrt{h^2\left(1+\gamma^2-h^2\right)} \\
\text{and this} & \gamma^4 + 2\gamma^2\left(1-h^2\right) + \left(1-h^2\right)^2 & \leq & \gamma^2 h^2\left(1+\gamma^2-h^2\right) \\
\text{and this} & \left[\gamma^4 + \left(2-h^2\right)\gamma^2 + \left(1-h^2\right)\right]\left(1-h^2\right) & \leq & 0 \\
\text{and this} & \gamma^4 + \left(2-h^2\right)\gamma^2 + \left(1-h^2\right) & \geq & 0
\end{array} \tag{4.52}$$

We can square both sides of line 3 in (4.52) since both sides of the inequality on line 3 are positive. The roots of the quadratic in γ^2 on the last line of (4.52) are -1 and $h^2 - 1$. Since the coefficient of γ^4 in the quadratic is greater than 0, the graph of the quadratic is concave up, and the equality on the last line of (4.52) will hold when $\gamma^2 \leq -1$ or $\gamma^2 \geq h^2 - 1$. But $\gamma^2 \geq h^2 - 1$ is just the condition for the stability of the zero solution. Thus $\tilde{c}_-$ is less than $\frac{1}{\gamma}$ over the range of parameters in which we are interested.

When $h^2 - 1 < 0$, $\tilde{c}_-$ is again less than $\frac{1}{\gamma}$. This follows by a similar proof to that for the case above when $h^2 - 1 > 0$. Following the same steps as in (4.52) but

making the necessary alterations in direction of the inequalities we arrive again at the same conclusion: $\tilde{c}_- \leq \frac{1}{\gamma}$ if $\gamma^2 \geq h^2 - 1$.

We are now ready to determine the region of the parameter space in which A^2 is both real and non-negative:

- If $h^2 - 1 > 0$ then A^2 is real when $\tilde{c} \leq \tilde{c}_-$ or $\tilde{c} \geq \tilde{c}_+$ and non-negative when $\tilde{c} \leq \frac{1}{\gamma}$. But $\tilde{c}_+ > \frac{1}{\gamma}$ and $\tilde{c}_- \leq \frac{1}{\gamma}$. Thus A^2 is real and non-negative precisely when $\tilde{c} \leq \tilde{c}_-$.

- If $h^2 - 1 < 0$ then A^2 is real when $\tilde{c}_+ \leq \tilde{c} \leq \tilde{c}_-$ and non-negative when $\tilde{c} \leq \frac{1}{\gamma}$. But $\tilde{c}_+ \leq 0$ and $\tilde{c}_- \leq \frac{1}{\gamma}$. Thus, for positive c, A^2 is real and non-negative when $\tilde{c} \leq \tilde{c}_-$. If c may be negative, then A^2 is real and non-negative when $\tilde{c}_+ \leq \tilde{c} \leq \tilde{c}_-$.

- Lastly if $h^2 - 1 = 0$, then A^2 is real when $\tilde{c} \leq \frac{1-\gamma^2}{2\gamma}$ and non-negative when $\tilde{c} \leq \frac{1}{\gamma}$. But $\frac{1-\gamma^2}{2\gamma} < \frac{1}{\gamma}$. Thus A^2 is real and non-negative when $\tilde{c} \leq \frac{1-\gamma^2}{2\gamma}$. Since $\frac{1-\gamma^2}{2\gamma} = \lim_{h \to 1} \tilde{c}_-$ we have that A^2 is real and non-negative when $\tilde{c} \leq \tilde{c}_-$, where it is understood that the limit will be taken if necessary.

Résumé

In conclusion, the condition for the existence of the stationary points (i.e. A^2 is real and non-negative) is that $\tilde{c} \leq \tilde{c}_-$. This condition is valid when the zero background is stable ($h^2 < 1 + \gamma^2$) and h, c and γ are positive. The condition applies to both stationary points.

If we allow c to be negative (as will be necessary in the numerical continuation of $\psi_\pm$ in section 4.4) then both stationary points will exist as long as in addition to the condition $\tilde{c} \leq \tilde{c}_-$ we have that $\tilde{c} \geq \tilde{c}_+$ or $h^2 - 1 \geq 0$.

4.3.2 Stability of the stationary points

The equations for $\dot{A}$ and $\dot{\theta}$ are

$$\dot{A} = 2Ah \sin 2\theta - 2\gamma A - \frac{2}{3} c A^3 \tag{4.53}$$

$$\dot{\theta} = h \cos 2\theta + 1 - A^2 \tag{4.54}$$

Applying the linearisation operator about a stationary point (A_s, θ_s) gives

$$\delta\dot{A} = \left(2h \sin 2\theta_s - 2\gamma - 2cA_s^2\right) \delta A + \left(4hA_s \cos 2\theta_s\right) \delta\theta \tag{4.55}$$

$$\delta\dot{\theta} = \left(-2A_s\right) \delta A + \left(-2h \sin 2\theta_s\right) \delta\theta \,. \tag{4.56}$$

In matrix form this is

$$\begin{pmatrix} \delta\dot{A} \\ \delta\dot{\theta} \end{pmatrix} = 2M \begin{pmatrix} \delta A \\ \delta\theta \end{pmatrix} \tag{4.57}$$

where M is given by

$$M = \begin{pmatrix} h\sin 2\theta_s - \gamma - cA_s^2 & 2hA_s\cos\theta_s \\ -A_s & -h\sin 2\theta_s \end{pmatrix} \tag{4.58}$$

Assuming a time dependence for δA and $\delta\theta$ of the form

$$\begin{pmatrix} \delta A \\ \delta\theta \end{pmatrix} = \begin{pmatrix} a \\ \phi \end{pmatrix} e^{2\lambda t} \tag{4.59}$$

where a and ϕ are independent of t, converts equation (4.57) into an eigenvalue problem

$$2M \begin{pmatrix} \delta A \\ \delta\theta \end{pmatrix} = 2\lambda \begin{pmatrix} \delta A \\ \delta\theta \end{pmatrix} . \tag{4.60}$$

The eigenvalues of M are given by the roots of the characteristic polynomial, $\det(M - \lambda I) = 0$. Here I is the 2×2 identity matrix. Expanding the characteristic polynomial we obtain

$$\lambda^2 + \left(\gamma + cA_s^2\right)\lambda + \left[2hA_s^2\cos 2\theta_s - (h\sin 2\theta_s)\left(h\sin 2\theta_s - \gamma - cA_s^2\right)\right] = 0 , \tag{4.61}$$

which has solutions

$$\begin{aligned} 2\lambda_\pm &= -(\gamma + cA_s^2) \\ &\pm \left[(\gamma + cA_s^2)^2 - 8hA_s^2\cos 2\theta_s + 4h^2\sin^2 2\theta_s - 4(\gamma + cA_s^2)\,h\sin 2\theta_s\right]^{\frac{1}{2}} . \end{aligned} \tag{4.62}$$

The real part of $\lambda_- \leq 0$ so λ_- will not cause the stationary points to become unstable. The real part of λ_+ will be greater than zero if the condition

$$4h^2\sin^2 2\theta_s - 8hA_s^2\cos 2\theta_s - 4\left(\gamma + cA_s^2\right)h\sin 2\theta_s > 0 \tag{4.63}$$

holds, since this condition will make the terms inside the square brackets in (4.62) greater than $\gamma + cA_s^2$. Conversely, if condition (4.63) does not hold, then the real part of λ_+ will be less than zero since the terms inside the square brackets in (4.62) will be less than $\gamma + cA_s^2$. Simplifying (4.63) we find that a stationary points is stable if and only if

$$A_s^2 \geq \frac{1 - \gamma\tilde{c}}{1 + \tilde{c}^2} . \tag{4.64}$$

Comparing this with the expressions for the stationary points $A_\pm$ in (4.48) we find that A_+ is always stable while A_- is always unstable.

4.3.3 Summary of the adiabatic results

The adiabatic equations have two stationary points (A_+, θ_+) and (A_-, θ_-). If $c > 0$ then the stationary points exist in the parameter region $c \leq 3\tilde{c}_-$. If $c < 0$, the stationary points exist in the region $3\tilde{c}_+ \leq c \leq 3\tilde{c}_-$ if $h^2 - 1 < 0$ and in the region $c \leq 3\tilde{c}_-$ if $h^2 - 1 > 0$. The constants $\tilde{c}_\pm$ are given in (4.51) and depend only on h and γ. The $A_\pm$ are given by (4.48). The $\theta_\pm$ are determined from the corresponding $A_\pm$ using

$$\theta_\pm = \tfrac{1}{2} \cos^{-1} \frac{A_\pm^2 - 1}{h} . \tag{4.65}$$

The stationary point (A_+, θ_+) is always stable for $c > 0$ (when $c < 0$ the zero background is unstable) while the stationary point (A_-, θ_-) is always unstable.

4.4 Continuation of $\psi_\pm$

After completing the adiabatic analysis of the soliton solution $\psi = A\text{sech}\,(Ax)e^{i\theta}$ we are ready to proceed to the continuation of ψ_+ and ψ_-. We expect that the results of the adiabatic analysis will agree with those of the continuation, at least in the parameter range where the adiabatic analysis is valid, namely $c \ll 1$.

4.4.1 Numerical tool: AUTO97

The continuation of ψ_+ and ψ_- was performed using the AUTO97 software package [6].

The software package AUTO97 is capable of continuing solutions to first-order ordinary differential equations of the form

$$\frac{\mathrm{d}\vec{u}}{\mathrm{d}t} - \vec{f}\,(\vec{u}(t), \mu, \lambda) = 0 , \quad t \in [0, 1] \tag{4.66}$$

where $\vec{u}(t)$ and $\vec{f}$ are $\in \Re^n$, $\lambda \in \Re$ and $\mu \in \Re^{n_\mu}$. The parameter in which the solution is continued is λ (the parameter we use in our continuation of $\psi_\pm$ is c). The vector μ contains the other parameters. The system may be subject to n_b boundary conditions,

$$b\,(\vec{u}(0), \vec{u}(1), \mu, \lambda) = 0 , \quad b \in \Re^{n_b} , \tag{4.67}$$

and to n_q integral constraints,

$$\int_0^1 q\,(\vec{u}(s), \mu, \lambda)\ \mathrm{d}s = 0 , \quad q \in \Re^{n_q} . \tag{4.68}$$

For the problem to be formally well-posed, $n_\mu = n_b + n_q - n$ must be greater than zero. The mathematical details of the functioning of AUTO97 can be found in [53] and [54].

The second-order differential equation we are continuing is not in the form (4.66). Firstly, AUTO97 requires that the t-interval be $[0, 1]$. However, we would like our x-interval to approximate the range $(-\infty, \infty)$ so that the localised solutions have space to decay to the flat backgrounds. After choosing our x-interval (for example $[-100, 100]$) we must thus translate and scale x (calling the new variable t) to give us an interval from $[0, 1]$. Secondly, we must convert our equation from second-order to first-order at the expense of adding a new complex variable $\phi = \psi_x$ and making our system four-dimensional ($n = 4$) instead of two. In addition, the solutions we are continuing (ψ_+ and ψ_-) not only remain solutions when translated in x and but also continue to satisfy our boundary conditions after such translations. The result of this is that, even with the imposed boundary conditions, our solutions are part of a continuous family of solutions. In order to select a particular one of this family of translated solutions for continuation we need to add an additional constraint. Since ψ_+ and ψ_- are symmetric about $x = 0$ we may restrict ourselves to solutions which are even in x. Later (in chapter 5) we will continue solutions which are not symmetric. In these non-symmetric cases we must use a different method to select an individual member from the family of solutions. Our approach is to impose a special integral condition

$$\int_0^1 \vec{u}(t) \cdot \left(\frac{\mathrm{d}\vec{u}}{\mathrm{d}t}\right)_{k-1} (t)\, \mathrm{d}t = 0\,. \tag{4.69}$$

Here the dot product is the Euclidean dot product in $\Re^n$. The subscript $k-1$ indicates that the derivative of u is evaluated at the previous numerical step. This integral condition selects the solution whose position, σ, relative to some reference solution, $\vec{u}(t)$, minimises the function

$$g(\sigma) = \int_0^1 |\vec{u}(t+\sigma) - \vec{u}_{k-1}(t)|^2\, \mathrm{d}t\,. \tag{4.70}$$

The effect is to make the position of the solution found at the next step of the continuation as close to that of the previous solution as possible. The norm here is the Euclidean norm in $\Re^n$, i.e. $|\vec{u}(t)|^2 = \vec{u}(t) \cdot \vec{u}(t)$.

4.4.2 Continuation of ψ_+

The results of the continuation of the soliton ψ_+ are shown in Figure 4.1. The ψ_+ solution of the parametrically driven damped NLS equation corresponds to the lower of the two points where the graph crosses the $c = 0$ axis. We fixed $\gamma = 0.5$ and $h = 0.8$.

For $\gamma = 0.5$ and $h = 0.8$, we have $\tilde{c}_- = 0.347$ and $\tilde{c}_+ = -3.12$. Recall from the adiabatic analysis that the stationary points exist when $c \geq 3\tilde{c}_+$ and $c \leq 3\tilde{c}_-$ when $h^2 - 1 < 0$ (as is the case here). The constants $\tilde{c}_\pm$ are given by equation (4.51). Therefore, for these h and γ the stationary points found in the adiabatic

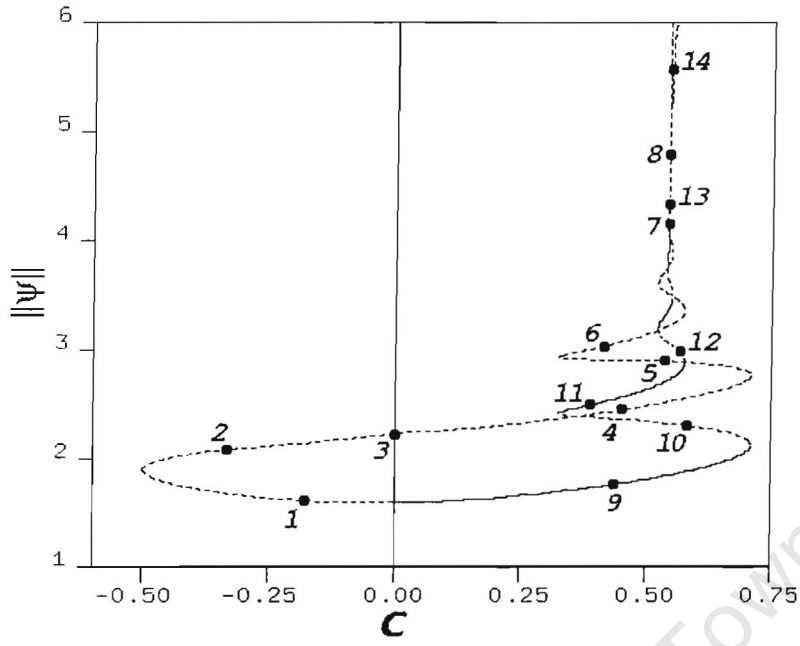

Figure 4.1: *Bifurcation diagram for ψ_+ when $h = 0.8$ and $\gamma = 0.5$. The Sobolev norm $||\psi||^2 = \int_{-\infty}^{\infty} \left(|\psi|^2 + |\psi_x|^2\right) dx$ is plotted against c (the filtering parameter). Stable (unstable) branches are shown as solid (dashed) lines. Points 1-8 mark solutions on the branch found by initially continuing into the region $c < 0$. Points 9-14 mark solutions on the branch found by initially continuing into the region $c > 0$. Near the end of the branch ($||\psi|| > 5$) the lateral humps encounter the boundaries of the numerical system causing the branch to bend away from vertical.*

analysis exist when c is less 1.04 and greater than -9.37. The adiabatic analysis predicts that the branch obtained by continuing from ψ_+ will remain stable (for $c > 0$) and that the branch obtained by continuing from ψ_- will remain unstable. For positive c less than 0.7 the results of the continuation of $\psi_\pm$ using AUTO agree with the adiabatic analysis. For $c < 0$ all branches are unstable, as we expect, since the zero background is unstable for negative c. When c becomes large the adiabatic analysis is no longer applicable and we see that the branch from ψ_+ turns back and becomes unstable, while the branch from ψ_- continues to exist well past the region of existence predicted by the adiabatic analysis.

As we continue from ψ_+ into the region $c < 0$, the solution develops into a three-hump state, with the three humps close together. Continuing past the turning point (i.e. proceeding to the top branch in the $c < 0$ region), the three humps move apart and reshape to give us a bound state of three solitons once we return to $c = 0$. This bound state, called $\psi_{(-+-)}$, which consists of two ψ_- solitons bound to either side of a ψ_+ soliton, is a solution of the parametrically driven NLS equation and found previously in [55].

Crossing over into the $c > 0$ region, we reach a series of turning points. Each turning results in the creation of another hump at the centre of the solution. These additional humps may merge if the turning points are close together. Eventually only a large single composite hump and the two lateral humps from the $\psi_{(-+-)}$ solution are clearly distinguishable. Near the end of the branch ($||\psi|| > 5$) the lateral humps encounter the boundaries of the numerical system causing the branch to bend away from vertical.

Moving away from ψ_+ (the lower intersection point on the $c = 0$ axis) into the $c > 0$ region, we find that the solution gradually changes its shape, becoming two-humped after passing through the turning point near $c = 0.7$. It then enters a region where additional humps are added through a series of turning points (saddle-node bifurcations). As before (on the branch found by continuing $\psi_{(-+-)}$ to $c > 0$), a stage is reached when the central humps merge but, in this case, the two lateral humps are absent.

It is worthwhile noting that although the imaginary part of the solution becomes double-humped as we approach the turning point near between points 9 and 10, the magnitude of the solution remains single humped until we pass through the turning point near 11.

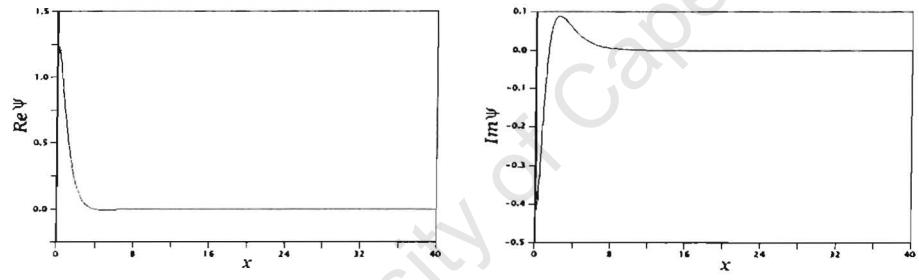

Figure 4.2: *Solution at point 1 in Figure 4.1. Here* $c = -0.23$ *and* $||\psi|| = 1.63$.

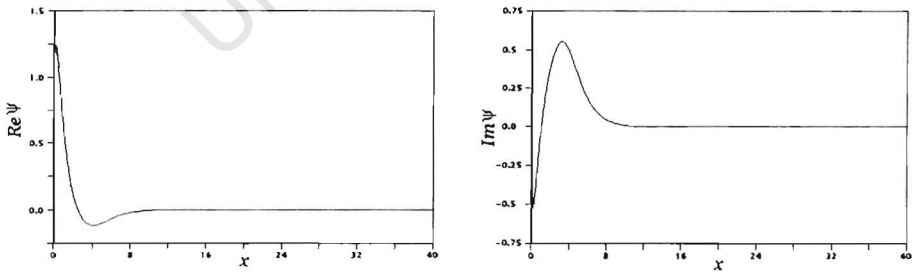

Figure 4.3: *Solution at point 2 in Figure 4.1. Here* $c = -0.30$ *and* $||\psi|| = 2.10$.

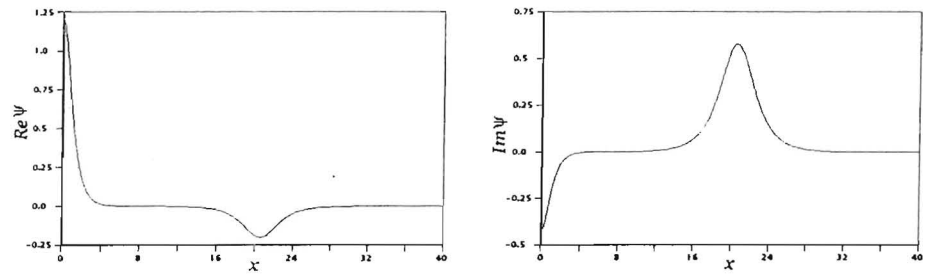

Figure 4.4: *Solution at point 3 in Figure 4.1. Here* $c = 0.00$ *and* $||\psi|| = 2.24$.

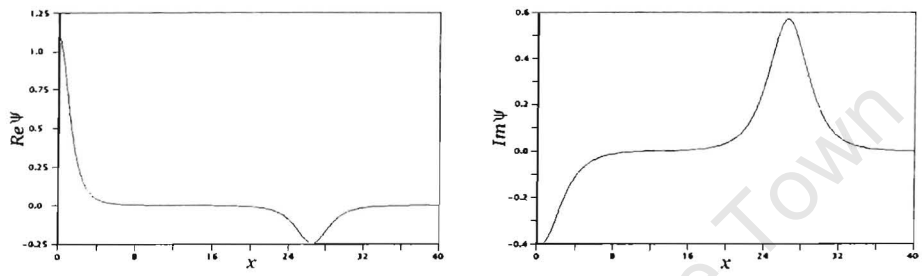

Figure 4.5: *Solution at point 4 in Figure 4.1. Here* $c = 0.40$ *and* $||\psi|| = 2.41$.

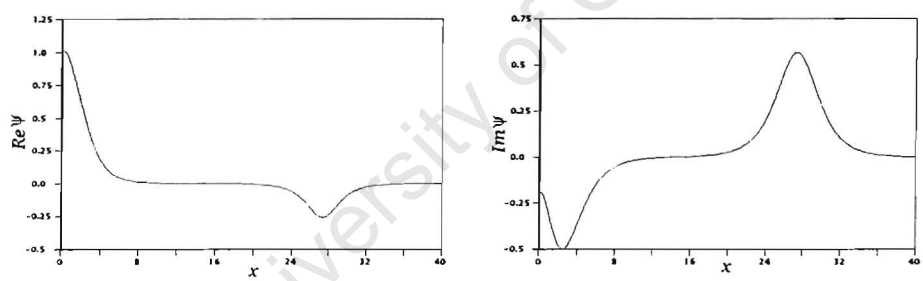

Figure 4.6: *Solution at point 5 in Figure 4.1. Here* $c = 0.55$ *and* $||\psi|| = 2.81$.

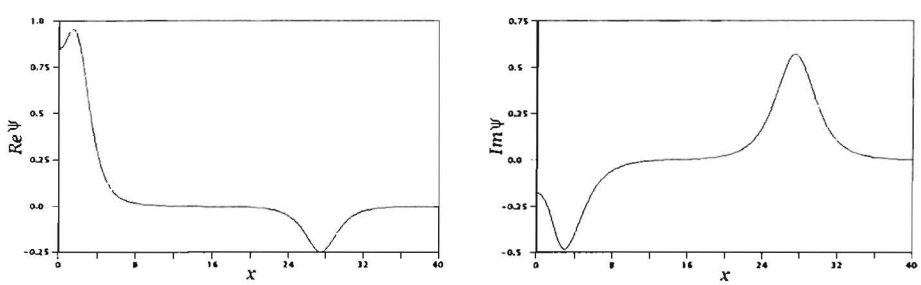

Figure 4.7: *Solution at point 6 in Figure 4.1. Here* $c = 0.44$ *and* $||\psi|| = 3.06$.

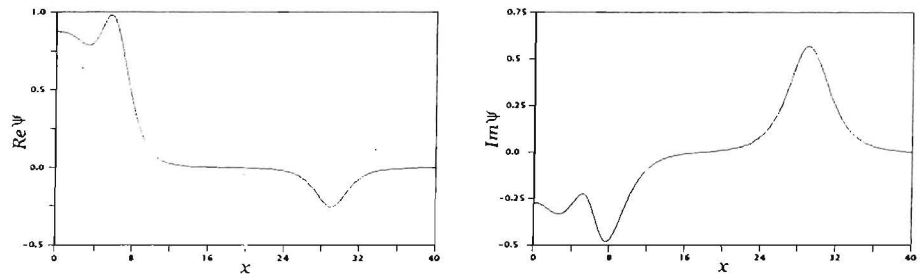

Figure 4.8: *Solution at point 7 in Figure 4.1. Here* $c = 0.54$ *and* $||\psi|| = 4.10$.

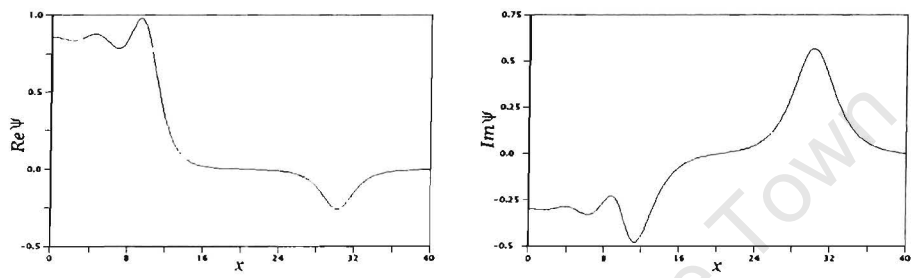

Figure 4.9: *Solution at point 8 in Figure 4.1. Here* $c = 0.54$ *and* $||\psi|| = 4.76$.

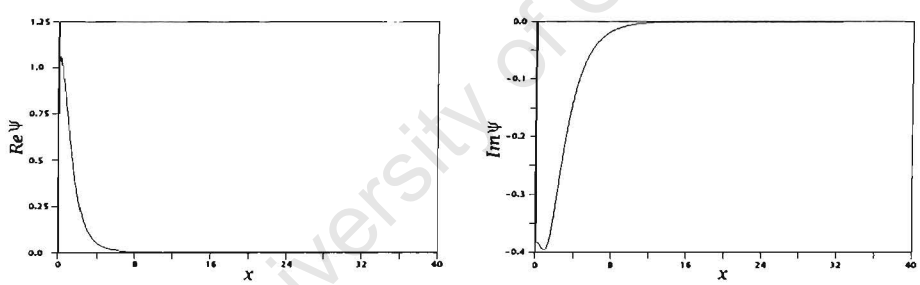

Figure 4.10: *Solution at point 9 in Figure 4.1. Here* $c = 0.48$ *and* $||\psi|| = 1.79$.

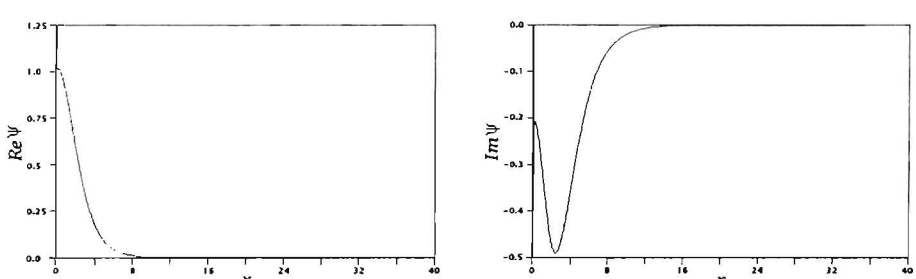

Figure 4.11: *Solution at point 10 in Figure 4.1. Here* $c = 0.60$ *and* $||\psi|| = 2.29$.

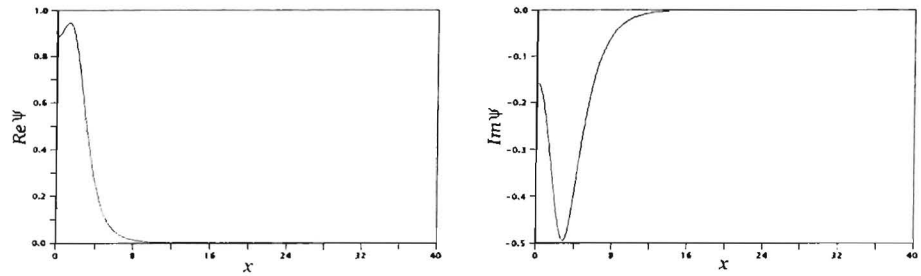

Figure 4.12: *Solution at point 11 in Figure 4.1. Here* $c = 0.40$ *and* $||\psi|| = 2.51$.

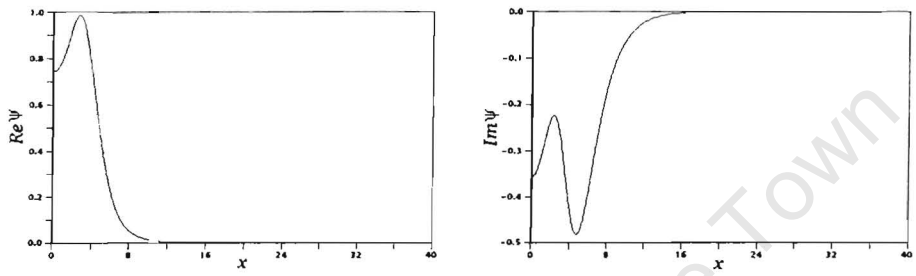

Figure 4.13: *Solution at point 12 in Figure 4.1. Here* $c = 0.55$ *and* $||\psi|| = 3.03$.

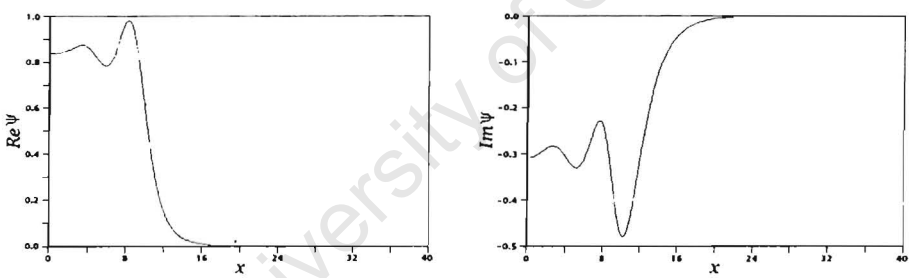

Figure 4.14: *Solution at point 13 in Figure 4.1. Here* $c = 0.54$ *and* $||\psi|| = 4.24$.

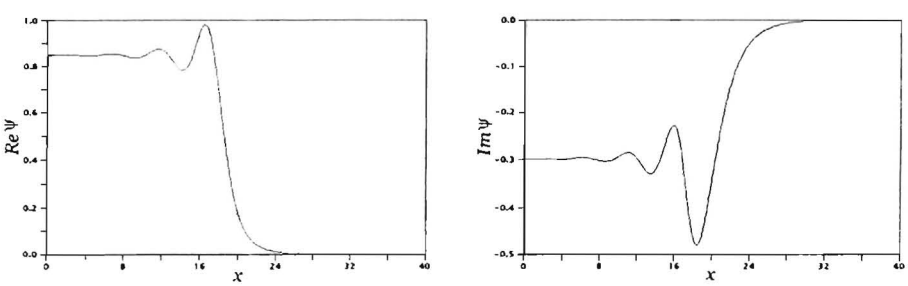

Figure 4.15: *Solution at point 14 in Figure 4.1. Here* $c = 0.54$ *and* $||\psi|| = 5.61$.

4.4.3 Continuation of ψ_-

We now consider the continuation of ψ_- which is shown in Figure 4.16. The parameters γ and h where again fixed at $\gamma = 0.5$ and $h = 0.8$. As we move along the branch into the $c < 0$ region the single hump of the ψ_- soliton splits in two forming a double hump. The double humped solution then simply broadens as c is decreased. Continuing ψ_- into the $c > 0$ region results only in the broadening of the central hump. This broadening is (in both cases) a simple stretching of the solution profile as predicted by our analysis of the large c limit of (4.1) in section 4.2.3.

The question then arises as to what the final shapes of the double hump and single hump solutions will be as $c \to -\infty$ and $c \to +\infty$ respectively. In other words, which solution of (4.38) is approximated by the rescaled double hump when $c \to -\infty$ and which solution of (4.37) is approximated by the rescaled singled hump when $c \to +\infty$. We may take our solutions of (4.1) for large $|c|$ as first approximations to solutions of (4.37) or (4.38). Then, using the same method used to correct approximate solutions during numerical continuation, we may correct these approximations until we arrive at numerical solutions for (4.37) and (4.38). The solution of (4.38) which the rescaled double hump tends as $c \to -\infty$ to is shown in the left-hand plot in Figure 4.19. The solution of (4.37) which the rescaled single hump tends as $c \to +\infty$ to is shown in the right-hand plot in Figure 4.19.

Note that although the adiabatic analysis predicts the existence of the ψ_- solution branch for small (positive) c, it also predicts that this branch will meet the ψ_+ branch in a saddle-node bifurcation for a finite value of c. This is in qualitative disagreement with what was observed numerically. These two results are reconciled in section 4.6.

4.5 Stability analysis

Given a solution, $\psi_s = u + iv$, to the Ginzburg-Landau equation we test it for stability by adding a small perturbation of the form

$$\delta\psi(x,t) = [\delta u(x) + i\delta v(x)]\, e^{\lambda t}\,, \tag{4.71}$$

where δu and δv are real and λ may be complex, and linearising in $\delta\psi$. This gives an eigenvalue problem of the form

$$\mathcal{H}\begin{pmatrix} \delta u \\ \delta v \end{pmatrix} = \lambda J \begin{pmatrix} \delta u \\ \delta v \end{pmatrix}\,, \tag{4.72}$$

where $\mathcal{H}$ and J are as in equation (4.6).

We solve the above eigenvalue problem by expanding δu, u, δv and v in the Fourier series on the interval $\left[-\frac{L}{2}, \frac{L}{2}\right]$. Truncating the series converts the problem

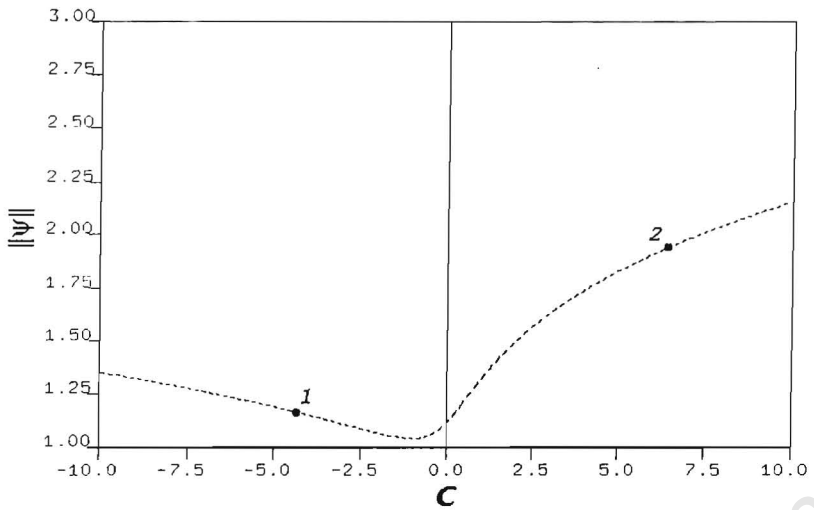

Figure 4.16: *Bifurcation diagram for ψ_- when $h = 0.8$ and $\gamma = 0.5$. The Sobolev norm $||\psi||^2 = \int_{-\infty}^{\infty} \left(|\psi|^2 + |\psi_x|^2\right) dx$ is plotted against c (the filtering parameter). Both branches are unstable.*

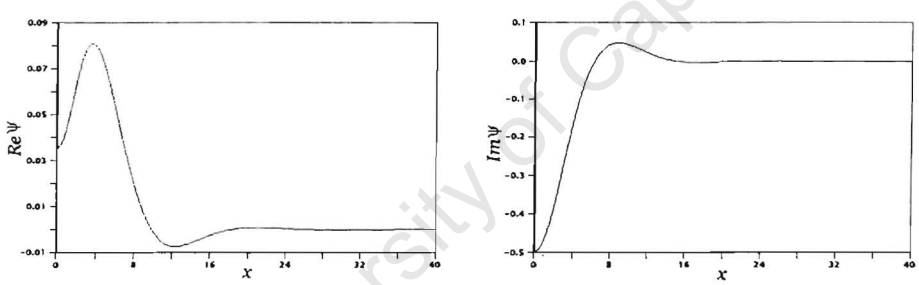

Figure 4.17: *Solution at point 1 in Figure 4.16. Here $c = -3.56$ and $||\psi|| = 1.13$.*

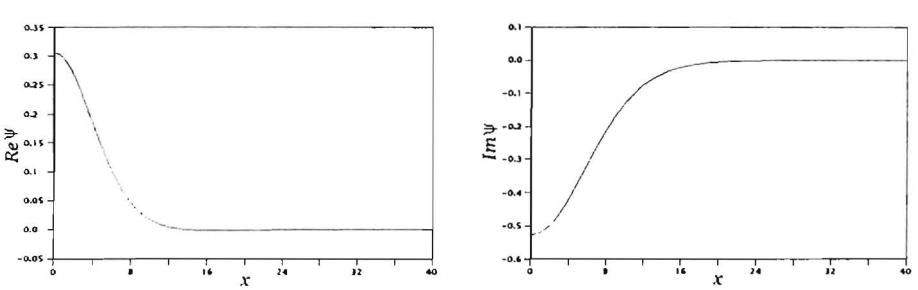

Figure 4.18: *Solution at point 2 in Figure 4.16. Here $c = 5.89$ and $||\psi|| = 1.90$.*

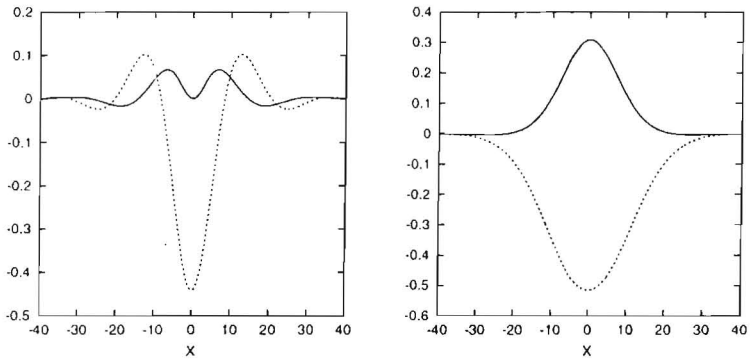

Figure 4.19: *On the left we have the solution of equation (4.38) which when rescaled gives the limit that the double hump solution shown in Figure 4.17 tends to as $c \to -\infty$. On the right we have the solution of equation (4.37) which when rescaled gives the limit that the single hump solution shown in Figure 4.18 tends to as $c \to +\infty$. The real part of ψ is denoted by a solid line and the imaginary part by a dashed line in both plots.*

to one of finding the eigenvalues (λ) of a large (but finite) complex square matrix. We truncated the series to 300 Fourier modes on the interval $[-28, 28]$.

The continuation of the NLS soliton ψ_+, for $h = 0.8$ and $\gamma = 0.5$, is shown in Figure 4.1. Continuing ψ_+ into the region $c < 0$ results in an immediate loss of stability since the zero background is unstable for $c < 0$. The $\psi_{(-+-)}$ solution of the NLS equation (the top intersection with the $c = 0$ line in Figure 4.1) is found to be unstable in agreement with [55]. The instability of the $\psi_{(-+-)}$ solution is caused by a pair of degenerate real eigenvalues. Each of these two eigenvalues is associated with one of the lateral ψ_- pulses of the $\psi_{(-+-)}$ solution. The instability of ψ_- is caused by a single real eigenvalue which is greater than zero. When the solution branch crosses over into the $c > 0$, the two unstable real eigenvalues from the two lateral pulses become the only eigenvalues with positive real parts. At the next turning point they are joined by a third positive real eigenvalue. This third eigenvalue then crosses the imaginary axis at each successive turning point. The magnitude of the third eigenvalue's excursions from zero decrease as we move further along the branch. The solution remains unstable overall as a result of the positive real eigenvalues from the two lateral ψ_- pulses. These results are in agreement with the adiabatic analysis since the solutions are unstable while $|c| \ll 1$.

While continuing ψ_+ into the region $c > 0$ the branch remains stable until the first turning point. Again this is in agreement with the results of the adiabatic analysis. It then becomes unstable and alternates stability at each successive turning point as a single real eigenvalue moves back and forth across the imaginary axis. As the magnitude of the changes in c between successive turning points decreases, so do the changes in the magnitude of the eigenvalue responsible for the instability.

The bifurcation diagram for ψ_-, for $h = 0.8$ and $\gamma = 0.5$, is shown in Figure

4.16. The solutions found by continuation in c from ψ_- are all found to be unstable. This agrees with the adiabatic analysis of ψ_-. In addition, when ψ_- is continued into the region $c > 0$ the instability of the solution branch results from a single (positive) real eigenvalue. This was expected since the instability of ψ_-, itself, results from a single (positive) real eigenvalue as mentioned above.

4.6 Existence region of the pulse-like solutions on the hc-plane

As we mentioned in section 4.4.3, there is a certain discrepancy between the adiabatic analysis and numerical continuation. Numerically, the ψ_- soliton was found to be continuable all the way to $c = +\infty$ whereas the adiabatic approach predicted the existence of a turning point at $c = 3\tilde{c}_2$, where the ψ_- should have merged with the ψ_+ branch. As for the ψ_+ solution, we found that it turns into a pulse with the double-humped imaginary part (and not into the ψ_- branch as suggested by the adiabatic approximation.) In order to shed some light on the possible source of the discrepancy we performed the numerical continuation of the pulse ψ_- in h, for several fixed values of c. Here, by the ψ_- we mean the pulse solution which results from the continuation of the Schrödinger ψ_- soliton to positive c, for some fixed large value of h (in our case for $h = 0.8$.) Having obtained this starting-point solution for several values of c, we then continued it in h, from $h = 0.8$ to smaller h. The stability of the arising solutions was examined by computing eigenvalues of the operator (4.6) at sample values of h.

In each case considered, the ψ_- branch was found to turn into the ψ_+ solution as h reached the threshold value $h_{\rm cr} = h_{\rm cr}(\gamma, c)$. (That is, for $h > h_{\rm cr}$ there are two branches of solutions whereas for $h < h_{\rm cr}$, there is none; see Fig.4.20(a)). The entire ψ_- branch is unstable; the single positive real eigenvalue moves to the negative semiaxis as the branch is continued past the turning point. Continuing the arising ψ_+ branch to larger h, we reach another turning point at $h = h_2$, where the ψ_+ solution transforms into a pulse with the double-humped imaginary part. The values $h_{\rm cr}$ and h_2 are shown in Fig.4.20(b), as functions of c (for the fixed $\gamma = 0.5$). As $c \to \infty$, the difference $h_2 - h_{\rm cr}$ decreases but remains nonzero. We verified this by computing $h_{\rm cr}$ and h_2 for equation (4.37) which pertains to $c = \infty$. In the same plot we display the function $c_- = 3\tilde{c}_-(h, \gamma)$ (see equation 4.51) which gives the adiabatic approximation to the curve $h_{\rm cr}(c)$. Note that for small c, there is a good agreement between numerical and approximate values but as c grows, the two curves diverge.

Continuing the ψ_+ branch past the second turning point, the solution adds another hump in the middle of the pulse, turns back again, adds another one, and so on. (See Fig.4.20(a)). A long plateau developes in the middle of the pulse, just like when it was continued in c. Similarly to the c-continuation, the turning

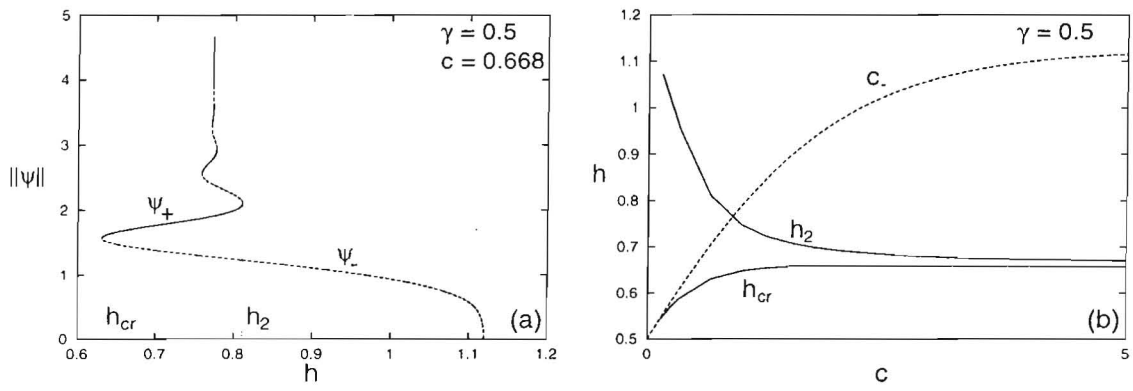

Figure 4.20: *(a) The Sobolev norm of the solitary wave solution as a function of the driving strength h. The solid and dashed lines indicate stable and unstable branches, respectively. (b) The pulse existence region on the (c, h)-plane. Two pulse solutions, ψ_+ and ψ_-, are born as h exceeds the value $h_{cr}(c)$ depicted by the lower solid line. The upper solid curve gives the upper boundary of the ψ_+-pulse's existence domain, $h_2(c)$. Also shown is the adiabatic approximation to the saddle-node bifurcation curve, $c_- = 3\tilde{c}_-$ from Eq.(4.51) (dashed line).*

points on the h-axis separate regions of stability from regions of instability, with the instability being caused by a single positive real eigenvalue (which moves through $\lambda = 0$ at the turning points.)

From figure 4.20(b) it is clear why the saddle-node bifurcation point where the ψ_+ and ψ_- solutions would merge, did not appear in Fig. 4.1 or Fig. 4.16. The reason is that Fig. 4.1 or Fig. 4.16 were plotted for a relatively large value of h ($h = 0.8$) whereas according to Fig. 4.20(b), a horisontal line $h = \text{const}$ with $h > 0.660$ can have no intersections with the saddle-node curve $h_{cr}(c)$. (Here all the numbers are for $\gamma = 0.5$.) The same Fig. 4.20(b) explains what semed to be a discrepancy between the adiabatic analysis and the numerical continuation of the soliton ψ_- in c. The numerical result that seemed to contradict the adiabatics was that for $h = 0.8$, ψ_- could be continued without bounds. It is now obvious from Fig. 4.20(b) that the unbounded continuation is only possible for h greater than 0.660. Continuing the ψ_- soliton to positive c for h *smaller* than 0.660, the branch turns back (already as the ψ_+ pulse) after hitting the lower solid curve in Fig. 4.20(b). Therefore, the pattern arising for h close to γ actually *is* in qualitative agreement with the adiabatic analysis, which was expected to be valid precisely for small c or, equivalently, for small $h - \gamma$ differences.

4.7 Summary

At the beginning of this chapter we introduced ψ_+ and ψ_-, two localised solutions of the damped-driven NLS equation. By adding the spectral filtering term, $-ic\psi_{xx}$,

to the damped-driven NLS equation we arrived at a parametrically driven CGLE:

$$i\psi_t + (1 - ic)\psi_{xx} + 2|\psi|^2\psi - (1 - i\gamma)\psi = h\overline{\psi}\,, \tag{4.73}$$

of which ψ_+ and ψ_- are solutions when $c = 0$. It was upon this equation that we focused our studies.

In the first part of the preliminaries section we examined the three flat background solutions of (4.73), namely $\psi = \phi_\pm$ and $\psi = 0$. By linearising (4.73) about each of the flat backgrounds we were able to determine the parameter regions wherein each of the backgrounds is stable and where decay to each of the flat backgrounds could occur. Given that h, γ and c are positive, we concluded that:

- $\psi = 0$ is stable when $h^2 \leq 1 + \gamma^2$.
- ϕ_- is unstable for all h, γ and c.
- ϕ_+ is stable when $h^2 \leq 1 + \gamma^2$ and $c \geq c_-$.

Decay can occur to $\psi = 0$ and ϕ_- for all h, γ and c. Decay can occur to ϕ_+ when ϕ_+ is stable and $c > c_-$. In the later part of the preliminaries section we showed that $\psi_\pm$ could be continued in c and we ended with a brief discussion of the $c \to \infty$ limit of (4.73).

In the next section, 4.3, we moved on to perform an adiabatic analysis of ψ_+ and ψ_-, valid when $|c| \ll 1$. When c becomes non-zero, solutions of the same form as ψ_+ and ψ_-, but with the constants A and θ replaced by slowly varying functions of time, were assumed to exist. A system of first order differential equations were found for A and θ. A pair of stationary points of this system were located. These points yield approximate stationary solutions of the driven complex Ginzburg-Landay equation. The stationary points were found to exist when $\tilde{c} \leq \tilde{c}_-$ and either $\tilde{c} \geq \tilde{c}_+$ or $h^2 - 1 \geq 0$, provided that h and γ are postive and the zero background solution is stable (i.e. $h^2 < 1 + \gamma^2$). Next the stability of the two stationary points was analysed. We found that the stationary point (A_+, θ_+) is stable for all $c > 0$ and that (A_-, θ_-) is always unstable.

The solutions ψ_+ and ψ_- were then continued in c numerically. The values of h and γ were fixed equal to 0.8 and 0.5 respectively. For $|c| \ll 1$ the results of the numerical continuation were found to agree with those of the adiabatic analysis. However, the adiabatic analysis predicted that the ψ_+ and ψ_- branches should merge at $\tilde{c} = \tilde{c}_-(h, \gamma)$. This merging of the two branches was not observed. A more complete understanding of the relationship was obtained by continuing solutions from the ψ_- towards smaller values of h. It was found that at $h = h_{cr}(c, \gamma)$ the ψ_- branch turned at a saddle-node bifurcation and eventually reached the ψ_+ branch. The maximum value of $h_{cr}(c, 0.5)$ was found to be approximately 0.660. If h is fixed greater than this maximum value, as we did in our earlier continuations, then the ψ_+ and ψ_- branches obtained by continuing in c do not merge. Instead, the psi_- branch may be continued indefinitely in c while the ψ_+ branch eventually

becomes a branch of neutrally stable bound fronts. The bound fronts are further analysed in chapter 5.

Returning now to the continuation of ψ_+ in c: When ψ_+ was continued into the region $c < 0$, we found a branch of unstable solutions. After turning back towards the $c = 0$ axis, the solutions on the branch became triple-humped and at $c = 0$ we found a previously known stationary solution of the damped-driven NLS equation, $\psi_{(-+-)}$. The branch then crossed over into the $c > 0$ region, where humps were added to the center of the solution at each of a series of turning points. Eventually, only a large single composite hump and the two lateral humps present in $\psi_{(-+-)}$ remained. Continuing ψ_+ into the region $c > 0$ we found a branch of solutions that was initially stable. Stability was lost when the branch turned back towards the $c = 0$ axis. At this point the solutions also became double-humped. As on the branch found by continuing $\psi_{(-+-)}$ into the $c > 0$ region, this branch then passed through a series of turning points at each of which a hump was added to the centre of the solution. After passing through many turning points we were left with a single composite pulse. In this case, no lateral humps were present.

All solutions obtained through the continuation of ψ_- were found to be unstable. Continuing ψ_- into the region $c < 0$ resulted in the splitting of the single hump of ψ_- and the formation of a double-humped solution. Moving further along this branch, the double-humped solution simply broadened as c was decreased. Continuing ψ_- towards postive c resulted only in the broadening of the pulse. The continuation of ψ_- covered the range $-10 < c < 10$.

Chapter 5

Front-like solutions to the driven Ginzburg-Landau equation

5.1 A new kink solution of the undamped driven NLS equation

The driven undamped NLS equation has the form

$$i\psi_t + \psi_{xx} + 2|\psi|^2\psi - \psi = h\bar{\psi}\,. \tag{5.1}$$

A similar equation was studied in [56] and [57] but with a minus sign in front of the nonlinearity and without the factor of i in front of the time derivative. If we look for stationary solutions the factor of i in front of the time derivative will not affect the results. We therefore try an ansatz similar to a stationary solution given in [56] and [57]:

$$\psi = A\tanh(kx) + iB\,\mathrm{sech}(kx)\ , \tag{5.2}$$

where A, B and k are constants. Splitting the NLS equation into its real and imaginary parts with $\psi = u + iv$ we obtain the equations

$$\begin{aligned} u_{xx} + 2\left(u^2+v^2\right)u - u &= hu\,, \\ v_{xx} + 2\left(u^2+v^2\right)v - v &= -hv\,. \end{aligned} \tag{5.3}$$

By substituting the ansatz (5.2) into (5.3) and then using the equality $\tanh^2(kx) = 1 - \mathrm{sech}^2(kx)$ to eliminate $\tanh^2(kx)$ we get the two equations

$$\begin{aligned} \left(-2k^2 - 2A^2 + 2B^2\right)\mathrm{sech}^2(kx) + 2A^2 - 1 - h &= 0 \\ \left(-2k^2 - 2A^2 + 2B^2\right)\mathrm{sech}^2(kx) + k^2 + 2A^2 - 1 + h &= 0\,, \end{aligned} \tag{5.4}$$

which must be satisfied for all x. Thus the coefficients of $\mathrm{sech}^2(kx)$ and $\mathrm{sech}^0(kx)$ in each of the two equations (5.4) must separately be zero. Setting all the coefficients

to zero yields a system of 3 algebraic equations,

$$-k^2 - A^2 + B^2 = 0\,, \quad 2A^2 - 1 = h \text{ and } \quad k^2 + 2A^2 - 1 = -h\,, \tag{5.5}$$

for A, B and k. Solving this system of equations we find

$$A^2 = \tfrac{1}{2}(h+1)\,, \quad B^2 = \tfrac{1}{2}(1-3h) \text{ and } \quad k^2 = -2h\,. \tag{5.6}$$

Since A^2, B^2 and k^2 must all be positive, the solutions (5.6) only exist when $-1 \leq h \leq 0$. However, switching the real and imaginary parts of the ansatz (5.2) has the same effect as changing the sign of h in (5.1). If we do both simultaneously, effectively changing the sign of h twice, then the equation (5.1) is left invariant and we have a new solution

$$v = A\,\mathrm{sech}\,(kx) + iB\tanh(kx)\,, \tag{5.7}$$

with

$$\begin{aligned} A^2 &= \tfrac{1}{2}(1+3h) \\ B^2 &= \tfrac{1}{2}(1-h) \\ k^2 &= 2h\,, \end{aligned} \tag{5.8}$$

which exists when $0 \leq h \leq 1$.

This solution may be incorporated into the scheme of [58] since u and v satisfy $u^2 + v^2 = C_1 + C_2 u^2$. It was missed in [58] since the possibility of including a constant term C_1 on the right-hand side was not considered.

5.2 Noncontinuability of the kink to nonzero γ (for $c = 0$)

We have found a new kink solution for the driven NLS equation and we now wish to determine if this solution can be continued to the damped ($\gamma \neq 0$) driven NLS equation (c will be fixed equal to 0 at this stage). In order to do so we expand the field ψ in powers of γ,

$$\psi = \psi_0 + \gamma\psi_1 + \gamma^2\psi_2 + \dots\,, \tag{5.9}$$

and substitute this expression into the damped driven NLS equation,

$$\psi_{xx} + 2|\psi|^2\psi - (1 - i\gamma)\psi = h\bar{\psi}\,. \tag{5.10}$$

Equating coefficients of powers of γ gives an equation for each power of γ. The equation for γ^0 terms requires that ψ_0 be a solution of the driven nonlinear Schrödinger equation. By decomposing ψ_0 and ψ_1 as

$$\psi_0 = u + iv\,; \quad \psi_1 = u_1 + iv_1\,, \tag{5.11}$$

the equation for the γ^1 terms becomes

$$L \begin{pmatrix} u_1 \\ v_1 \end{pmatrix} = \begin{pmatrix} v \\ -u \end{pmatrix} \tag{5.12}$$

where $L = \mathcal{H}|_{c=0,\gamma=0}$ and $\mathcal{H}$ is the operator obtained by linearising the CGLE about ψ_0 and is given in (4.6).

Fredholm's alternative states that equation (5.12) has bounded solutions if and only if the right-hand side is orthogonal to the kernel of $L^\dagger$. Since L is a real symmetric differential operator, we have $L = L^\dagger$. L has the null eigenvector

$$\begin{pmatrix} u_x \\ v_x \end{pmatrix}$$

due to the translational symmetry of the damped driven NLS equation.

Thus we arrive at the continuability condition

$$\int_{-\infty}^{\infty} (vu_x - uv_x)\, dx \;=\; 0\,. \tag{5.13}$$

Evaluating this condition for the kink solution $\psi = A\,\mathrm{sech}\,(kx) + iB\tanh\,(kx)$ we find

$$\int_{-\infty}^{\infty} (vu_x - uv_x)\, dx \tag{5.14}$$

$$= \int_{-\infty}^{\infty} \left[-ABk\,\mathrm{sech}(kx)\tanh^2(kx) \quad - ABk\,\mathrm{sech}^3(kx)\right] dx \tag{5.15}$$

$$= -ABk \int_{-\infty}^{\infty} \mathrm{sech}(kx)\, dx \tag{5.16}$$

$$\neq 0. \tag{5.17}$$

So the kink solution is not continuable unless one or more of A, B and k is zero.

5.3 Continuation of the kink in the parameters c and γ simultaneously

5.3.1 Continuability condition

Having discovered that the new kink solution cannot be continued in γ we now wish to determine if the kink solution can be continued simultaneously in both c and γ by picking a suitable curve in the (c, γ)-plane along which to continue. We attempt to continue in a single parameter ϵ which parameterises the line along which we wish to continue. c and γ are given by

$$c = c_1\epsilon + c_2\epsilon^2 + \ldots \quad ; \quad \gamma = \gamma_1\epsilon + \gamma_2\epsilon^2 + \ldots \quad . \tag{5.18}$$

We expand the field ψ in powers of ϵ,

$$\psi = \psi_0 + \epsilon\psi_1 + \epsilon^2\psi_2 + \dots \,, \tag{5.19}$$

and substitute this expression into the Ginzburg-Landau equation,

$$(1 - ic)\,\psi_{xx} + 2\,|\psi|^2\,\psi - (1 - i\gamma)\,\psi \;=\; h\bar{\psi}\,. \tag{5.20}$$

Equating coefficients of powers of ϵ gives an equation for each power of ϵ. The equation for ϵ^0 terms requires that ψ_0 be a solution of the driven NLS equation. By decomposing ψ_0 and ψ_1 as

$$\psi_0 = u + iv\,; \quad \psi_1 = u_1 + iv_1\,, \tag{5.21}$$

the equation for the ϵ^1 terms becomes

$$L\begin{pmatrix} u_1 \\ v_1 \end{pmatrix} = \begin{pmatrix} -c_1 v_{xx} + \gamma_1 v \\ c_1 u_{xx} - \gamma_1 u \end{pmatrix} \tag{5.22}$$

where $L = \mathcal{H}|_{c=0,\gamma=0}$ and $\mathcal{H}$ is the operator obtained by linearising the CGLE about ψ_0 and is given in (4.6).

Fredholm's alternative states that equation (5.22) has bounded solutions if and only if the right-hand side is orthogonal to the kernel of $L^\dagger$. Since L is a real symmetric differential operator, we have $L = L^\dagger$. The problem then becomes finding the kernel of L. Every zero mode of the driven NLS equation generates an element of the kernel of L The driven NLS has only one known zero mode, namely translation in x. The translational zero mode generates the kernel element

$$\begin{pmatrix} u_x \\ v_x \end{pmatrix}. \tag{5.23}$$

Demanding that the right-hand side of (5.22) be orthogonal to the kernel of $L^\dagger$ leads to the continuability condition

$$\int_{-\infty}^{\infty} \left\{(c_1 v_{xx} - \gamma_1 v)\,u_x - (c_1 u_{xx} - \gamma_1 u)\,v_x\right\} dx \;=\; 0 \tag{5.24}$$

which is satisfied by the kink solutions (5.2) and (5.7) when

$$\frac{c_1}{\gamma_1} = -\frac{\int_{-\infty}^{\infty} \operatorname{sech}(kx)dx}{k^2 \int_{-\infty}^{\infty} \operatorname{sech}^3(kx)dx}\,. \tag{5.25}$$

Here k is given by (5.6) for the kink solution (5.2) and by (5.8) for the kink solution (5.7). Using the relationship $\operatorname{sech}^2(kx) = 1 - \tanh^2(kx)$ and integrating by parts we find that

$$\int_{-\infty}^{\infty} \operatorname{sech}^3(kx)dx = \frac{1}{2}\int_{-\infty}^{\infty} \operatorname{sech}(kx)dx\,. \tag{5.26}$$

Substituting (5.26) into the continuability condition (5.25) gives

$$\frac{c_1}{\gamma_1} = -\frac{2}{k^2} = \frac{1}{h} \tag{5.27}$$

for the kink solution (5.2) and

$$\frac{c_1}{\gamma_1} = -\frac{2}{k^2} = -\frac{1}{h} \tag{5.28}$$

for the kink solution (5.7).

Thus we expect to be able to continue the new kink solution (5.2) along a curve in the (c, γ)-plane which has a tangent with slope h at the origin and the solution (5.7) along a curve with slope $(-h)$ at the origin. Since k^2 is positive, both curves will have a tangent with negative slope at the origin and continuation will only be possible to a region where the signs of c and γ differ. So one of c or γ will be negative. In the parameter region $c < 0$ or $\gamma < 0$ the zero background solution is unstable. It is, however, possible that the branch of solutions will turn back towards positive c and γ at some stage. The numerical continuation of the kink solution (5.7) in the parameters c and γ is presented in section 5.4.

5.3.2 Asymptotic analysis of the first order perturbations

We now wish to study the behaviour of the first order perturbations $\psi_1 = u_1 + iv_1$ as $x \to \pm\infty$ so that we can compare the behaviour with that seen in the numerical continuation of the kink solution. We will show that the solution is oscillatory as $x \to \pm\infty$.

The equation satisfied by the first order perturbations is (5.22). The solution which we are continuing is (5.7). Taking the limit of (5.22) as $x \to \pm\infty$ we obtain the equation

$$\begin{pmatrix} -\partial_x^2 + 1 + h - 2B^2 & 0 \\ 0 & -\partial_x^2 + 1 - h - 6B^2 \end{pmatrix} \begin{pmatrix} u_1^{(\pm)} \\ v_1^{(\pm)} \end{pmatrix} = \begin{pmatrix} \mp B\gamma_1 \\ 0 \end{pmatrix} . \tag{5.29}$$

Here B is given by $B^2 = \frac{1}{2}(1-h)$ (see equation (5.8)) and the sign in front of B on the right hand side depends on whether we are looking at the behaviour as $x \to \infty$ (the $-$ sign) or as $x \to -\infty$) the $+$ sign. The functions $u_1^{(\pm)}$ and $v_1^{(\pm)}$ are the asymptotic limits, as $x \to \pm\infty$, of u_1 and v_1 respectively. We will choose B to be the positive square root of $\frac{1}{2}(1-h)$ as this is the value of B to be used in the numerical continuation of the kink solution.

Substituting the $B = \sqrt{\frac{1}{2}(1-h)}$ into (5.29) we get the equations

$$\begin{aligned} \left(2h - \partial_x^2\right) u_1^{(\pm)} &= \mp\sqrt{\frac{1-h}{2}}\,\gamma_1 \\ \left(2h - 2 - \partial_x^2\right) v_1^{(\pm)} &= 0\,, \end{aligned} \tag{5.30}$$

which are two linear, uncoupled differential equations with constant coefficients and have the general solutions

$$\begin{aligned} u_1^{(\pm)} &= \mp\frac{\gamma_1}{2h}\sqrt{\frac{1-h}{2}} + \alpha_1^{(\pm)}e^{-\sqrt{2h}x} + \alpha_2^{(\pm)}e^{+\sqrt{2h}x} \\ v_1^{(\pm)} &= \beta_1^{(\pm)}e^{-\sqrt{2(h-1)}x} + \beta_2^{(\pm)}e^{+\sqrt{2(h-1)}x}\,. \end{aligned} \tag{5.31}$$

Here $\alpha_1^{(\pm)}, \alpha_2^{(\pm)}, \beta_1^{(\pm)}$ and $\beta_2^{(\pm)}$ are all complex constants. The condition that $u_1^{(\pm)}$ and $v_1^{(\pm)}$ be real imposes the constraints that $\alpha_1^{(\pm)}$ and $\alpha_2^{(\pm)}$ be real and that $\beta_1^{(\pm)} = \overline{\beta_2^{(\pm)}}$.

Since $h \geq 0$, both exponents in the general solution for $u_1^{(\pm)}$ are real. Thus, in order for u_1 to be bounded as $x \to \pm\infty$, we must have $\alpha_2^{(+)} = 0$ and $\alpha_1^{(-)} = 0$. This means that u_1 decays exponentially to a constant (the first term in the expression for $u_1^{(+)}$) as $x \to \infty$ and to minus the same constant as $x \to -\infty$. The perturbation to the real part of the solution (5.7) is ϵu_1. Since γ_1 is defined by $\gamma = \epsilon\gamma_1 + \epsilon^2\gamma_2 + \ldots$, the limit as $x \to \pm\infty$ of the perturbation added to the real part of (5.7) will be

$$\epsilon\left(\mp\frac{\gamma_1}{2h}\sqrt{\frac{1-h}{2}}\right) \simeq \mp\frac{\gamma}{2h}\sqrt{\frac{1-h}{2}}\,, \tag{5.32}$$

to first order in ϵ.

Since $h \leq 1$ both exponents in the general solution for $v_1^{(\pm)}$ are imaginary. Thus v_1 becomes oscillatory as $x \to \pm\infty$.

5.4 Results of the numerical continuation of the kink in c and γ

The AUTO97 software package [6] was used to continue the kink solution in c and γ simultaneously. The value of the parameter h was fixed at $h = 0.8$. Initially c and γ were both zero. The x-interval used for the continuation of the solution was $[-40, 40]$. The boundary conditions imposed were that $\psi_x(40) = \psi_x(-40) = 0$.

The bifurcation diagram for the continuation is shown in Figure 5.1. The solution branch forms a closed loop. The initial kink solution for $c = \gamma = 0$ is shown in Figure 5.2.

Continuing towards positive c the imaginary part of the solution develops ripples, resulting in a kink over an oscillatory background, as predicted by the asymptotic analysis in the previous section. See Figure 5.3. The change in the asymptotic value of the real part of the solution that is predicted by the asymptotic analysis, is not yet visible in Figure 5.3. To first order in ϵ, equation (5.32) gives the perturbation of the real part about zero to be ± 0.006957 as $x \to \pm\infty$, which is too small a correction to be visible on the graph.

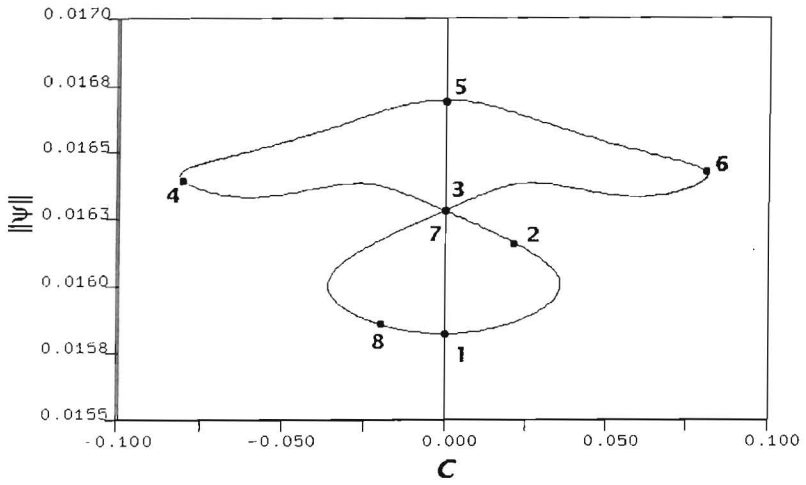

Figure 5.1: *Bifurcation diagram for the kink solution when* $h = 0.8$. *The norm* $||\psi||^2 = \int_{-\infty}^{\infty} |\psi_x|^2 \, dx$ *is plotted against* c *(the filtering parameter). Graphs of the solutions at points 1-8 are shown on the pages which follow.*

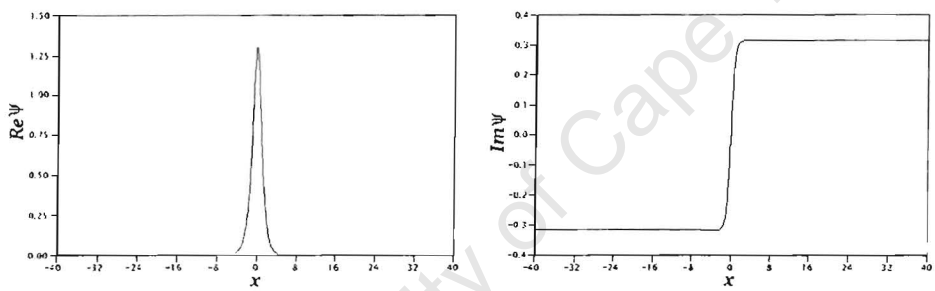

Figure 5.2: *Solution at point 1 in Figure 5.1. Here* $c = 0$, $\gamma = 0$ *and* $||\psi|| = 0.01582$.

Continuing further along the branch we cross the $c = 0$ axis at solution 3 which is shown in Figure 5.4. γ has also returned to zero. Solution 3 is related to solution 7 by the discrete symmetry transformation $\psi \to -\psi$.

At solution 4 the size of the perturbation of the real part of the solution has grown large enough to be visible in Figure 5.5. The asymptotic analysis predicts that the real part of the solution will tend to ∓ 0.0154 as $x \to \pm\infty$ (to first order in ϵ). The oscillations in the imaginary part of the solution have grown considerably.

At solution 5, c and γ are again zero. The perturbation to the real part of the solution has decreased to zero as expected from our analysis. Moving along the solution branch to solution 6 the perturbation to the real part grows again. However, it is now the limit $x \to -\infty$ which is negative and the limit $x \to \infty$ which is positive due to the change of sign of γ. As mentioned previously, solution 7 differs from solution 3 only by a change of sign. As we move along the branch

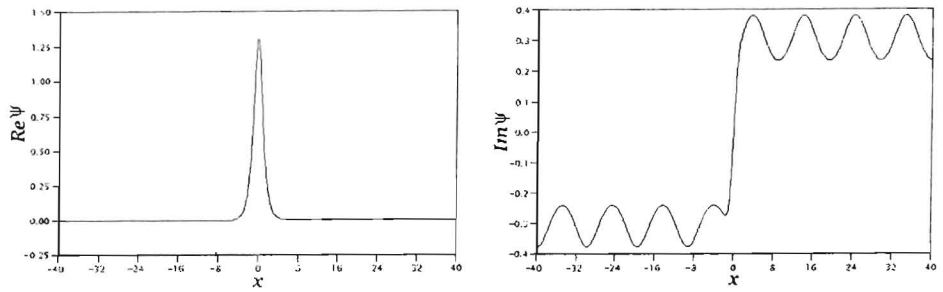

Figure 5.3: *Solution at point 2 in Figure 5.1. Here* $c = 0.0200$, $\gamma = -0.0159$ *and* $||\psi|| = 0.01617$.

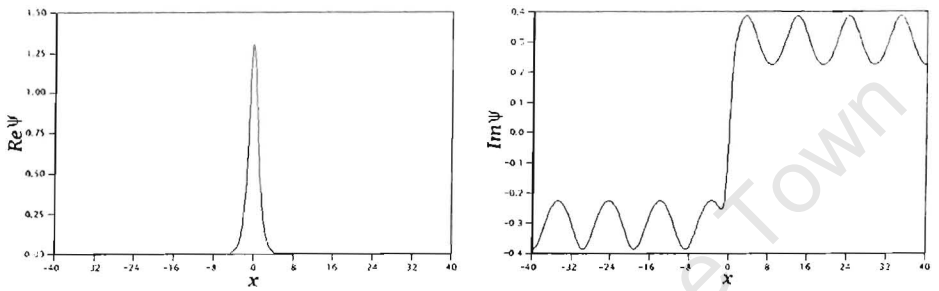

Figure 5.4: *Solution at point 3 in Figure 5.1. Here* $c = 0$, $\gamma = 0$ *and* $||\psi|| = 0.01639$.

past solution 8 (see Figure 5.9) the magnitude of the oscillations in the imaginary part of the solution decreases until it becomes zero once we return to solution 1.

Figure 5.10 shows a plot of γ against c obtained from the simultaneous continuation in c and γ. From the continuability condition (5.28) we expect that for small c and γ this plot will give a straight line through the point $c = 0, \gamma = 0$ with slope $-\frac{1}{h}$. This is, indeed, the case. The central portion of the line looks thicker due to the overlaying of the (c, γ) points from the smaller loop in the bifurcation diagram, Figure 5.1, upon the points from the larger loop.

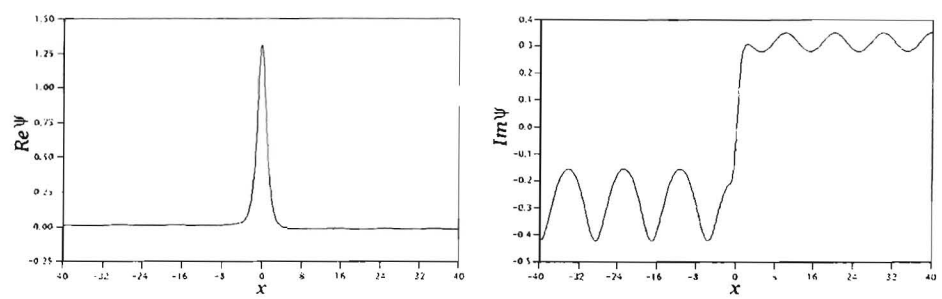

Figure 5.5: *Solution at point 4 in Figure 5.1. Here* $c = -0.0800$, $\gamma = 0.0629$ *and* $||\psi|| = 0.01639$.

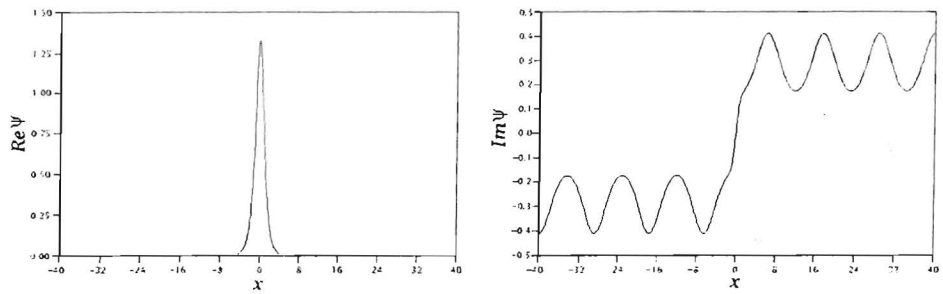

Figure 5.6: *Solution at point 5 in Figure 5.1. Here* $c = 0$, $\gamma = 0$ *and* $||\psi|| = 0.01670$.

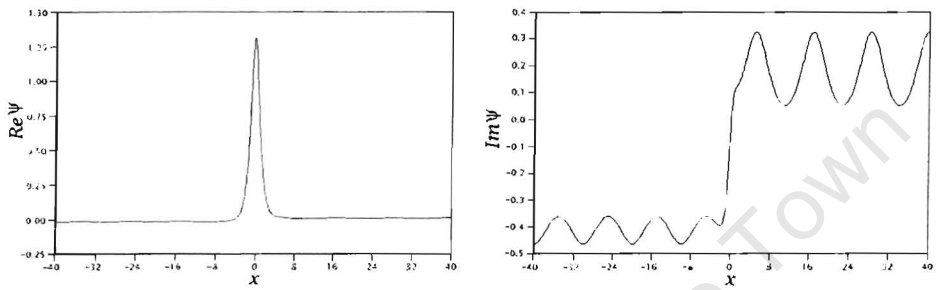

Figure 5.7: *Solution at point 6 in Figure 5.1. Here* $c = 0.0800$, $\gamma = -0.0628$ *and* $||\psi|| = 0.01643$.

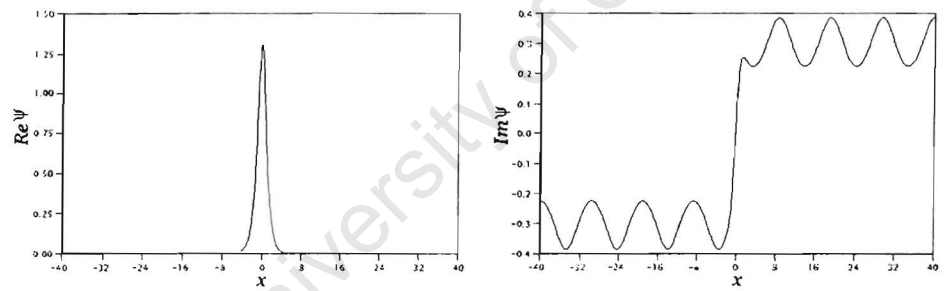

Figure 5.8: *Solution at point 7 in Figure 5.1. Here* $c = 0$, $\gamma = 0$ *and* $||\psi|| = 0.01628$.

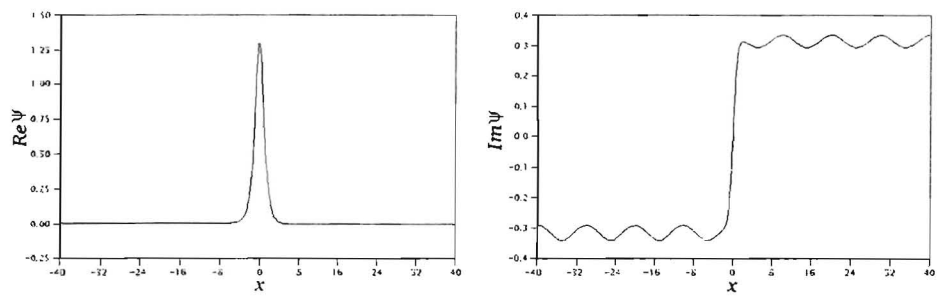

Figure 5.9: *Solution at point 8 in Figure 5.1. Here* $c = -0.0200$, $\gamma = 0.0160$ *and* $||\psi|| = 0.01586$.

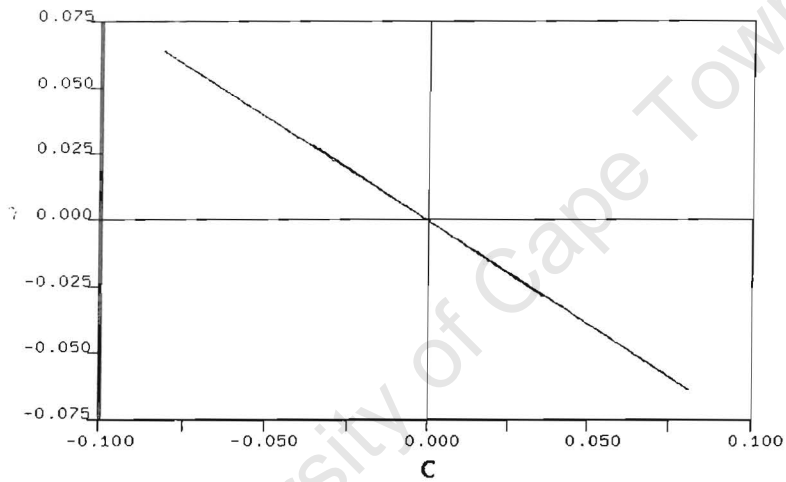

Figure 5.10: *A plot of γ against c.*

5.5 Continuation of the kink to non-zero velocity (for $\gamma = c = 0$)

We also wish to determine if the kink solution we have obtained can be continued to a solution travelling with non-zero velocity. Starting from the driven Schrödinger equation

$$i\psi_t + \psi_{xx} + 2|\psi|^2\psi - \psi = h\bar{\psi} \tag{5.33}$$

we find that a solution, $\psi(\xi)$, which depends only on $\xi = x + Vt$ obeys the equation

$$iV\psi_\xi + \psi_{\xi\xi} + 2|\psi|^2\psi - \psi = h\bar{\psi} \tag{5.34}$$

If we assume that V is small we may expand ψ in powers of V,

$$\psi = \psi_0 + V\psi_1 + V^2\psi_2 + \ldots, \tag{5.35}$$

and substitute this expansion into (5.34). Equating coefficients of powers of V gives an equation for each power of V. The equation for the V^0 terms requires that ψ_0 be a solution to (5.34) when $V = 0$. (This is true for the kink solution.) The equation for the V^1 terms is

$$i\psi_{0\xi} + \psi_{1\xi\xi} + 2\left[\psi_0^2\bar{\psi}_1 + 2|\psi_0|^2\psi_1\right] - \psi_1 = h\bar{\psi}_1\,. \tag{5.36}$$

By decomposing ψ_0 and ψ_1 into their real and imaginary parts,

$$\psi_0 = u + iv \quad ; \quad \psi_1 = u_1 + v_1\,, \tag{5.37}$$

the equation for the V^1 terms, (5.36), may be written as

$$L\begin{pmatrix} u_1 \\ v_1 \end{pmatrix} = \begin{pmatrix} -v_\xi \\ u_\xi \end{pmatrix} \tag{5.38}$$

where $L = \mathcal{H}|_{c=0,\gamma=0}$ and $\mathcal{H}$ is the operator obtained by linearising the CGLE about ψ_0 and is given in (4.6). A slight modification has to be made to L, namely that all occurences of x should be replaced with ξ.

Fredholm's alternative states that equation (5.38) has bounded solutions if and only if the right-hand side is orthogonal to the kernel of $L^\dagger$. Since L is a real symmetric differential operator, L is self-adjoint. The problem then becomes finding the kernel of L. Every zero mode of the driven NLS equation generates an element of the kernel of L. The only known zero mode is translation in ξ. The translational zero mode generates the kernel element

$$\begin{pmatrix} u_\xi \\ v_\xi \end{pmatrix}. \tag{5.39}$$

Demanding that the right-hand side of (5.38) be orthogonal to the kernel of $L^\dagger$ leads to a continuability condition,

$$\int_{-\infty}^{\infty} (u_\xi v_\xi - v_\xi u_\xi)\,\mathrm{d}x = 0\,, \tag{5.40}$$

which is identically satisfied.

We conclude that any stationary solution of the driven NLS equation (including the kink solution we have obtained) may be continued in the velocity, V, to a uniformly translating solution of the same equation. The only proviso is that the translational zero mode should be the only zero mode of the solution. If there are other zero modes then the vector on the right hand side of equation (5.38) will have to be orthogonal to those modes too.

5.6 Results of the numeric continuation of the kink to non-zero velocity

In section 5.5 we determined that the kink solution was continuable in the velocity, V. We thus proceeded to continue the kink (in V) using the AUTO97 software package [6]. This will allow us to compare the continuation of our kink solution to the continuations performed in [7] which also continued solutions of the undamped driven NLS equation in the parameter V. The value of h was fixed equal to 0.8. c and γ were fixed equal to zero. The x-interval used for the continuation was $[-40, 40]$. The boundary conditions imposed were $\psi_x(40) = \psi_x(-40) = 0$.

The bifurcation diagram for the continuation is shown in Figure 5.11 and the kink solution from which we start the continuation, in Figure 5.12.

As we increase V, the imaginary part of the background solutions, on both the left- and right-hand side of the kink, become oscillatory in space (as can be seen in Figures 5.13 and 5.14). The flat backgrounds on either side of the kink have become travelling waves which move with the same velocity as the kink itself. The solution in Figure 5.14 is close to a turning point in the solution branch.

As the solution branch passes back across the $V = 0$ axis we reach the almost stationary solution shown in Figure 5.15. This solution may be considered a kink connecting two almost stationary wave trains.

Moving further along the solution branch the magnitude of the travelling waves increases, as may be seen in Figures 5.16 and 5.17, and the peaks and troughs of the travelling waves cease to be symmetric. By the time we reach the solution shown in Figure 5.18 the travelling waves have become a series of pulses. Since these pulses contribute only to the imaginary part of the solution, they appear to be ψ_- pulses. The height of the pulses, which is approximately that of a ψ_- pulse, confirms this hypothesis. (The height of a ψ_- pulse is approximately 0.447 when $h = 0.8$ and $\gamma = 0$.) To the right of the kink we have $+\psi_-$ pulses. On the left we have $-\psi_-$ pulses.

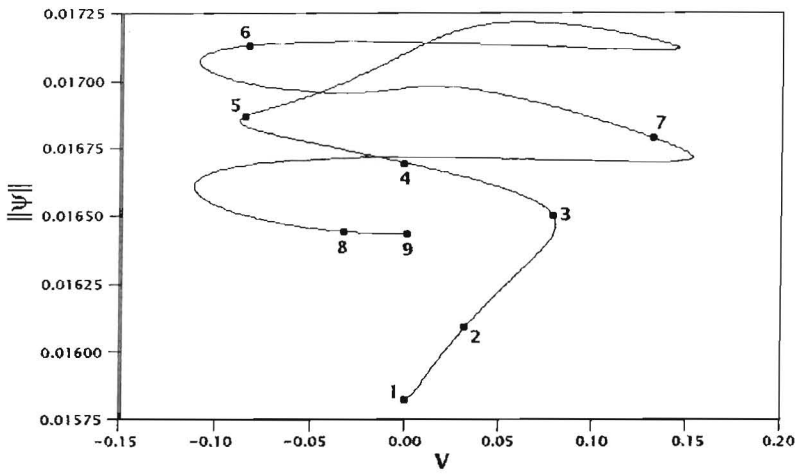

Figure 5.11: *Bifurcation diagram for the kink solution when* $h = 0.8$. *The derivative norm* $||\psi||^2 = \int_{-\infty}^{\infty} |\psi_x|^2 \, dx$ *is plotted against* V *(the velocity). Graphs of the solutions at points 1-9 are shown on the pages which follow.*

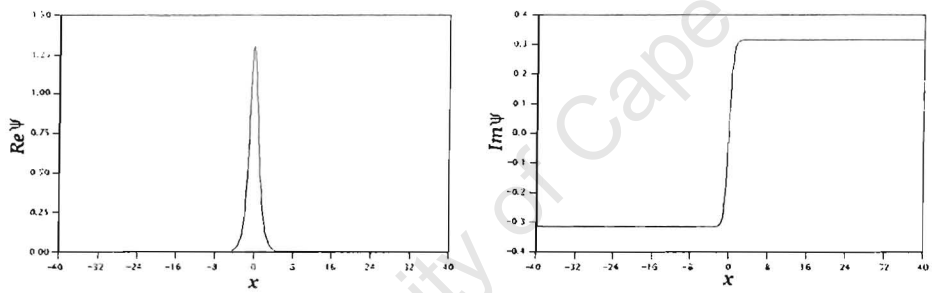

Figure 5.12: *Solution at point 1 in Figure 5.11. Here* $V = 0.00$ *and* $||\psi|| = 0.0158$.

Continuing further we find the amplitude of the kink in the imaginary part of the solution diminishing. The solution in Figure 5.19 has only a small kink between the two pulses and is qualitatively similar to the complex of two twist solutions shown in Figure 5(b) of [7].

In [7] it is conjectured that this complex, which becomes the solution shown in Figure 5.20 as $V \to 0$, exists right up to $V = 0$. However, the authors of [7] encounter the same problem we do here: The separation distance between the two pulses in the imaginary part of the solution goes to infinity as $V \to 0$ and the solution cannot be continued all the way to $V = 0$ without extending at least one of the boundaries of the x-interval used in the continuation out to infinity.

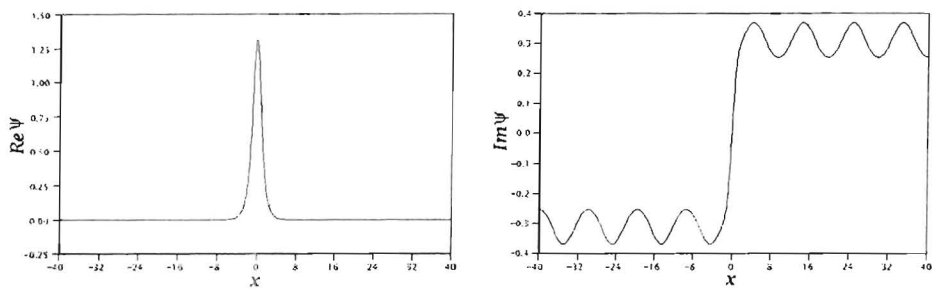

Figure 5.13: *Solution at point 2 in Figure 5.11. Here* $V = 0.0306$ *and* $||\psi|| = 0.0161$.

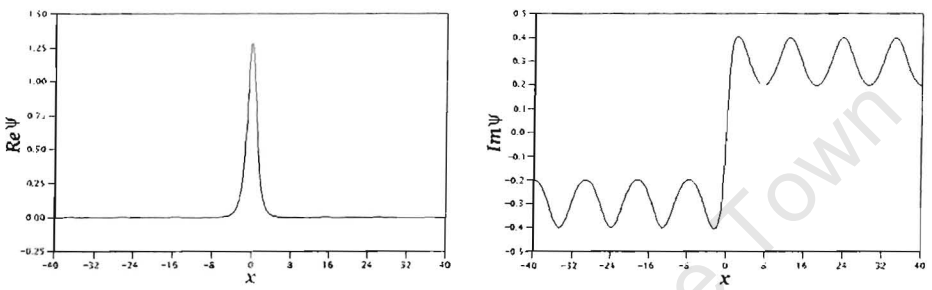

Figure 5.14: *Solution at point 3 in Figure 5.11. Here* $V = 0.0800$ *and* $||\psi|| = 0.0165$.

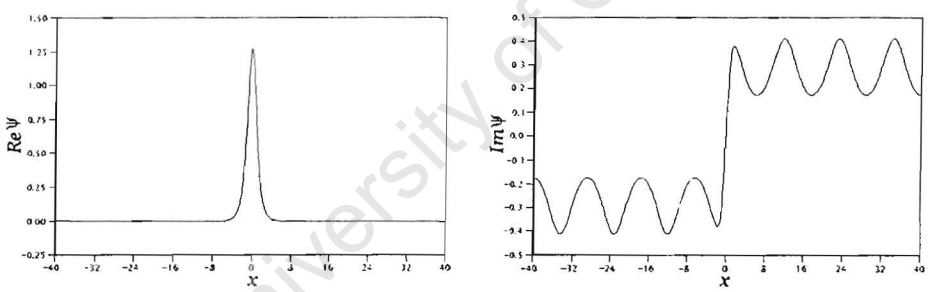

Figure 5.15: *Solution at point 4 in Figure 5.11. Here* $V = -0.0001$ *and* $||\psi|| = 0.0167$.

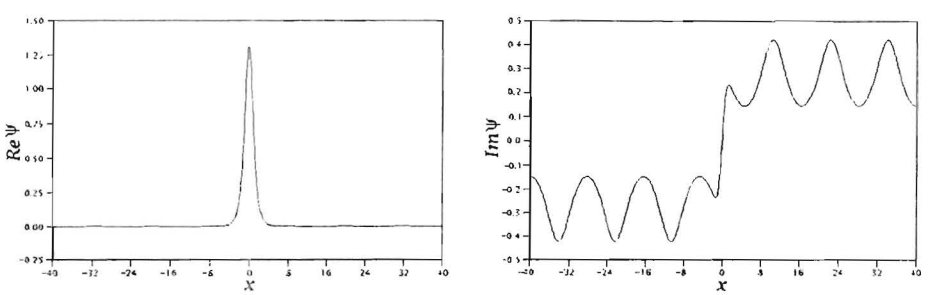

Figure 5.16: *Solution at point 5 in Figure 5.11. Here* $V = -0.0873$ *and* $||\psi|| = 0.0169$.

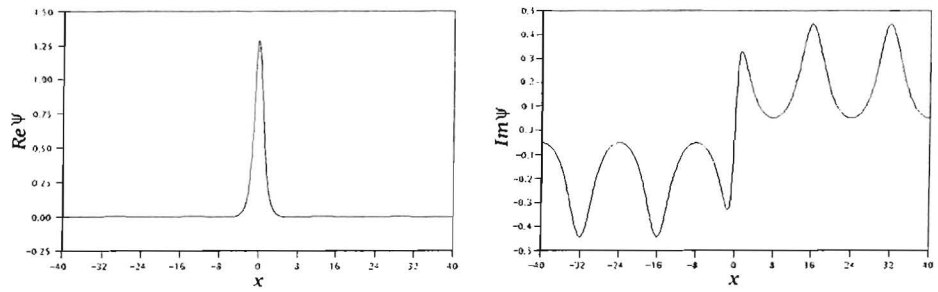

Figure 5.17: *Solution at point 6 in Figure 5.11. Here* $V = -0.0860$ *and* $||\psi|| = 0.0171$.

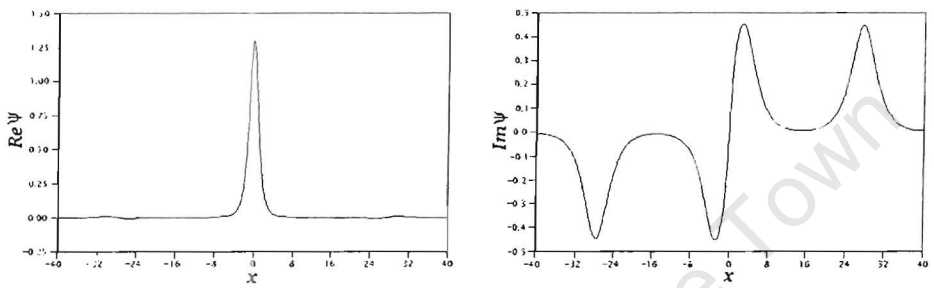

Figure 5.18: *Solution at point 7 in Figure 5.11. Here* $V = 0.139$ *and* $||\psi|| = 0.0168$.

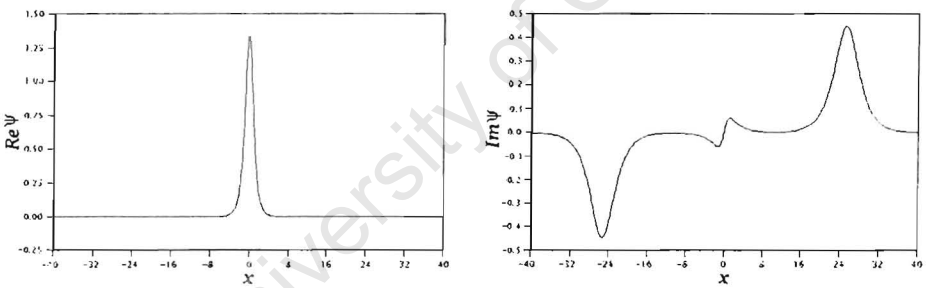

Figure 5.19: *Solution at point 8 in Figure 5.11. Here* $V = -0.0375$ *and* $||\psi|| = 0.0164$.

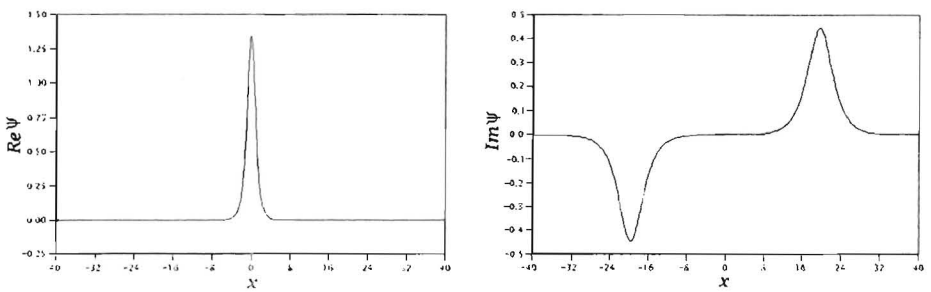

Figure 5.20: *Solution at point 9 in Figure 5.1. Here* $V = 0.0001$ *and* $||\psi|| = 0.0164$.

5.7 Results of the numerical continuation in c and γ of the broad multihumped solution

The broad multihumped solution shown in Figure 4.15, which was obtained numerically through the continuation of the ψ_+ solution of the NLS equation, appears to be a bound pair of fronts, interpolating between the zero background solution and the flat solution ϕ_+. In order to examine these fronts more closely we isolated the right hand front and attempted to continue it separately. The flat regions on either side of the isolated front were then extended by adding sections of the appropriate flat background.

The AUTO97 software package [6] was used to continue the right-hand front solution in c and γ simultaneously. The parameter h was fixed at $h = 0.8$. Initially c was 0.541 and γ was 0.5. The x interval over which the solution was sought was $[-40, 80]$. At the left-hand boundary we imposed the condition $\psi_x = 0$ while on the right we imposed the condition $\psi = 0$. We could not fix the value of ψ at the left-hand boundary since the value of the non-zero flat background, ψ_+, changes with γ. The norm used was the integral of $(|\psi|^2 + |\psi_x|^2)$ over the interval $[-40, 80]$. Although this norm diverges as the left-hand boundary of the interval tends to negative infinity, it poses no problems numerically since our interval has a fixed finite size and allows easier comparison with the Sobolev norm used in chapter 4.

The bifurcation diagram obtained through the continuation is shown in Figure 5.21. An enlargement of the section where $c < 0.6$ is shown in Figure 5.22. Since we are continuing in γ and c simultaneously, a graph of γ against c obtained during the continuation is shown in Figure 5.23. An enlargement corresponding to that in Figure 5.22 is shown in Figure 5.24.

Near $c = 0.323$ the norm has a maximum. For $c > 0.323$ the solution norm decreases uniformly as we move along the solution branch away from the maximum. While the norm is decreasing, the value of γ is increasing. The effects of increasing c are clearly visible in Figures 5.25-5.30: the greater the spectral filtering, the smoother the front's decay to ϕ_+. For large c one can notice the broadening of the solution profile which we expect from our analysis of the $c \to \infty$ limit. Compare, for example, the profiles of the solutions at point 3 (see Figure 5.27) and point 6 (see Figure 5.30).

Decay to the zero flat background is possible for all positive h, γ and c but we know from our discussion of the flat backgrounds in chapter 4 that decay to ϕ_+ is only possible when $c > c_-$. For this reason we have superimposed a plot of c_- against γ (for $h = 0.8$) on the graph in Figure 5.24. When the solution branch lies to the right of the c_- graph, decay to ϕ_+ is possible (and ϕ_+ is stable). When the solution branch lies to the left of the c_- graph, decay to ϕ_+ cannot occur (and ϕ_+ is unstable). At the point where the solution branch and the graph of c_- cross, the rate of decay to ϕ_+ is zero.

As we move away from the maximum of the norm at $c = 0.323$ into the region

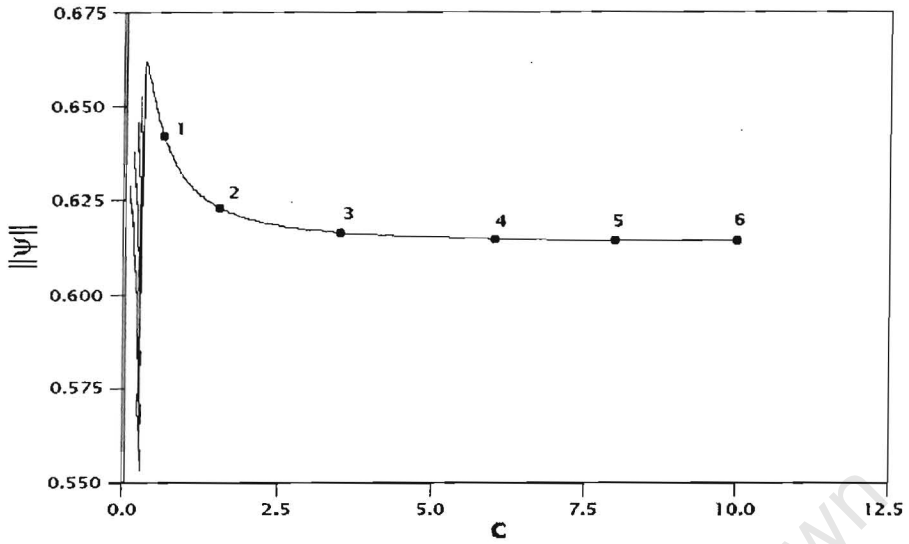

Figure 5.21: *Bifurcation diagram for the front solution when* $h = 0.8$. *The norm* $||\psi||^2 = \int_{-40}^{80} \left(|\psi|^2 + |\psi_x|^2\right) dx$ *is plotted against* c *(the filtering parameter). Graphs of the solutions at points 1-6 are shown on the pages which follow.*

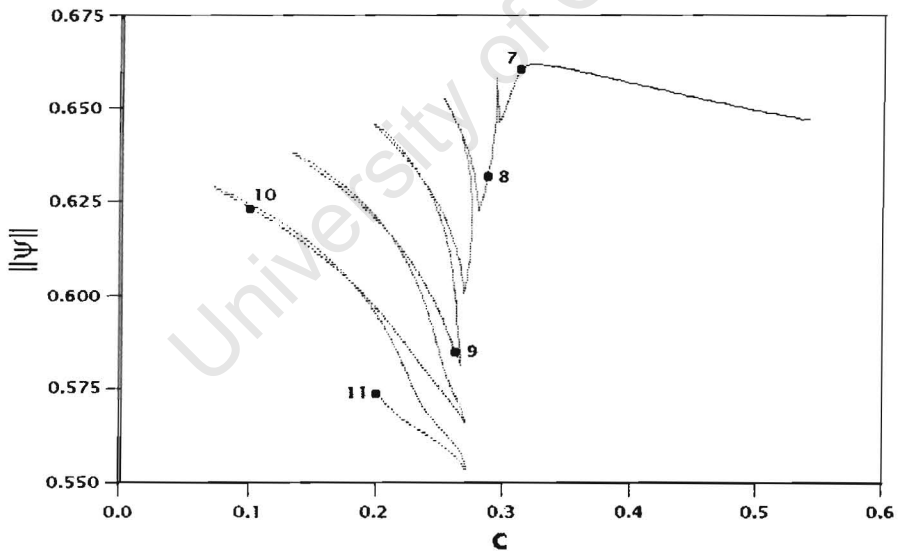

Figure 5.22: *Enlargement of the bifurcation diagram, for the front solution when* $h = 0.8$, *showing the region* $c < 0.6$. *The norm* $||\psi||^2 = \int_{-40}^{80} \left(|\psi|^2 + |\psi_x|^2\right) dx$ *is plotted against* c *(the filtering parameter). Graphs of the solutions at points 7-11 are shown on the pages which follow. Solid lines indicate stable solutions, while dotted lines indicate unstable solutions.*

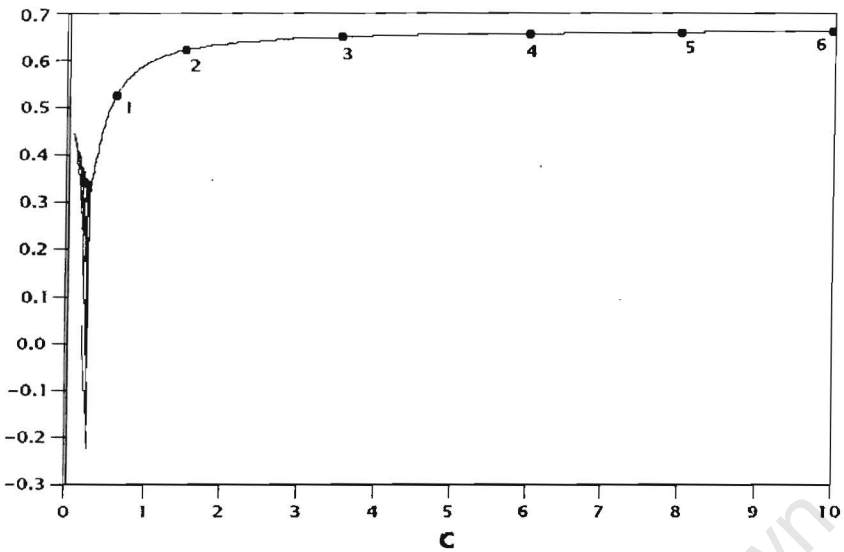

Figure 5.23: *Plot of γ against c obtained during the continuation of the front solution when $h = 0.8$. An enlargement of the region $c < 0.6$ is shown in Figure 5.24 below. Points 1-6 are the same as in the bifurcation diagram, Figure 5.21. Graphs of the solutions at the points 1-6 may be found on the pages which follow.*

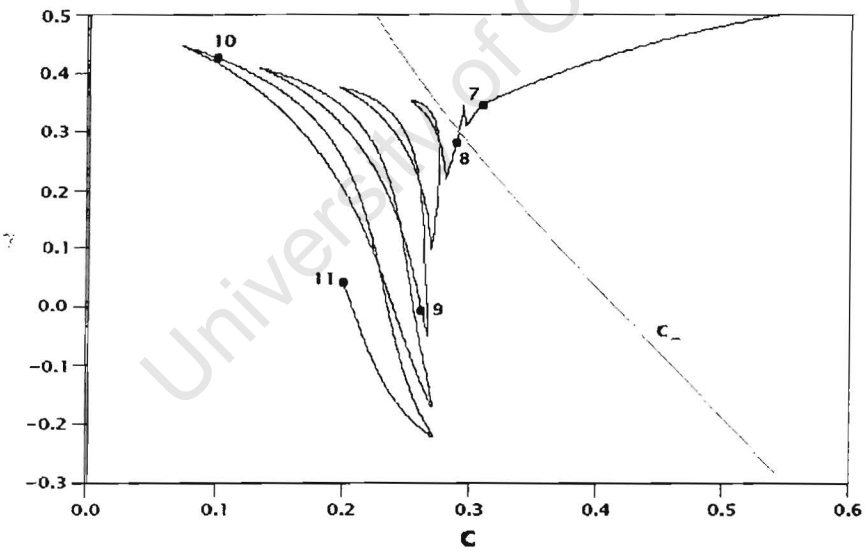

Figure 5.24: *Enlargement of the plot of γ against c obtained during the continuation of the front solution, showing the region $c < 0.6$. The grey line is a graph of γ against c_-. The point at which the two graphs cross is the point where decay rate to the flat background ϕ_+ becomes zero. Points 7-11 are the same as in the enlargement of bifurcation diagram, Figure 5.22. Graphs of the solutions at points 1-6 may be found on the pages which follow.*

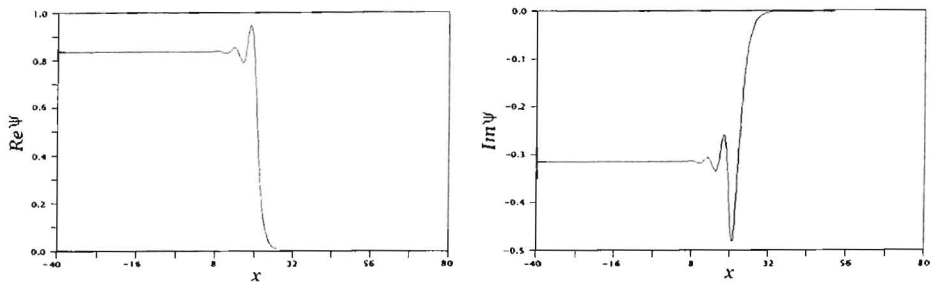

Figure 5.25: *Solution at point 1 in Figure 5.21. Here* $c = 0.622$, $\gamma = 0.528$ *and* $||\psi|| = 0.642$.

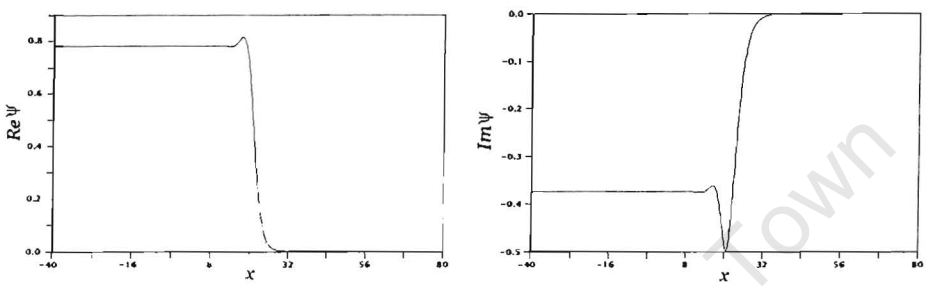

Figure 5.26: *Solution at point 2 in Figure 5.21. Here* $c = 1.51$, $\gamma = 0.623$ *and* $||\psi|| = 0.623$.

where $c < 0.323$ we approach the c_- curve in Figure 5.24. Indeed, the solution at point 7 (shown in Figure 5.31) decays only slowly to ϕ_+. At point 8 the solution branch has just crossed the c_- curve and we can see in Figure 5.32 that the front no longer decays to ϕ_+. The solution at point 8 is a front which interpolates between an oscillatory background on the left and the zero background on the right. As we move further into the $c < 0.323$ region, the solution branch passes through a series of sharp turning points. Similar sharp turns may be seen in the graph of γ against c. While moving along the solution branch the magnitude of the oscillations in the background to the left of the front fluctuates. This fluctuation is more pronounced in the imaginary part of the solution. See Figures 5.33-5.35. Numerical boundary effects due to the constraint $\psi_x = 0$ which is imposed at the left-hand side of the interval may be seen in these three figures. However, the effects disappear from the oscillatory background well before the front is reached.

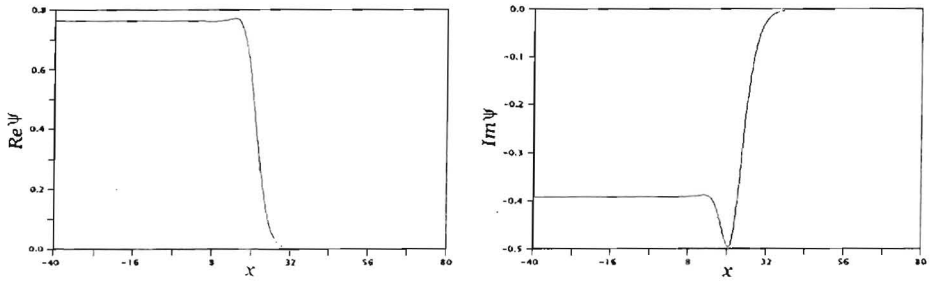

Figure 5.27: *Solution at point 3 in Figure 5.21. Here* $c = 3.51$, $\gamma = 0.650$ *and* $||\psi|| = 0.617$.

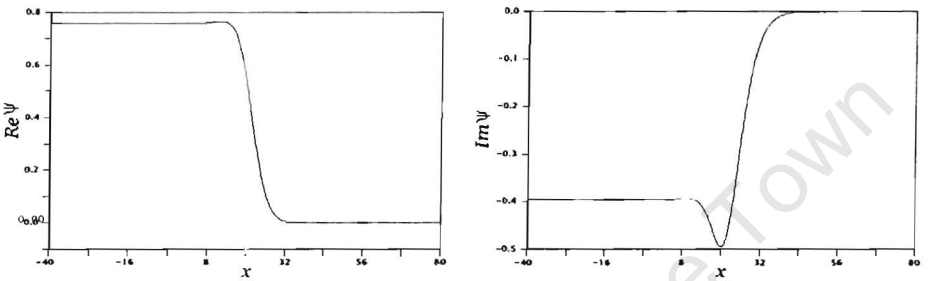

Figure 5.28: *Solution at point 4 in Figure 5.21. Here* $c = 6.01$, $\gamma = 0.657$ *and* $||\psi|| = 0.615$.

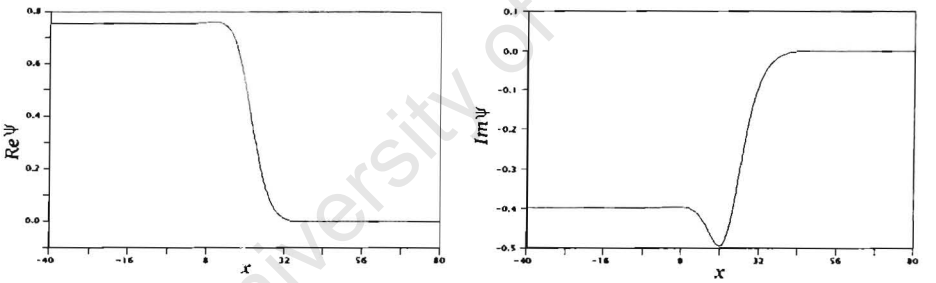

Figure 5.29: *Solution at point 5 in Figure 5.21. Here* $c = 8.01$, $\gamma = 0.660$ *and* $||\psi|| = 0.615$.

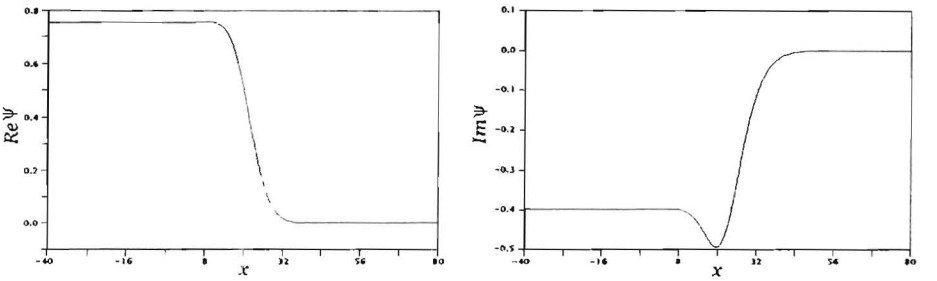

Figure 5.30: *Solution at point 6 in Figure 5.21. Here* $c = 10.0$, $\gamma = 0.661$ *and* $||\psi|| = 0.614$.

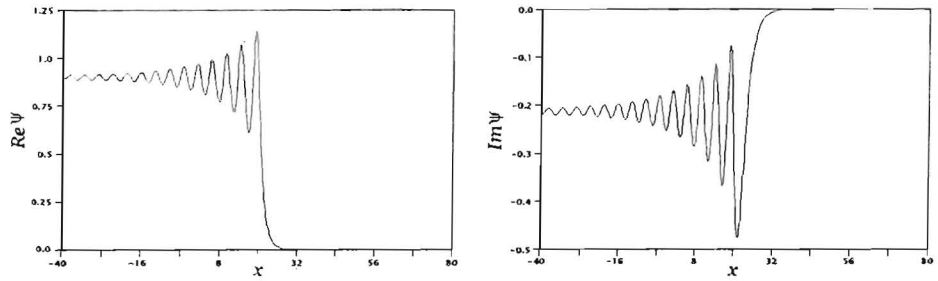

Figure 5.31: *Solution at point 7 in Figure 5.22. Here* $c = 0.318$, $\gamma = 0.357$ *and* $||\psi|| = 0.662$.

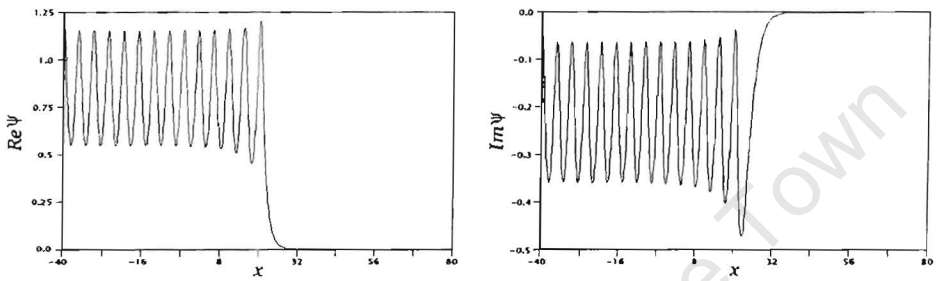

Figure 5.32: *Solution at point 8 in Figure 5.22. Here* $c = 0.290$, $\gamma = 0.297$ *and* $||\psi|| = 0.637$.

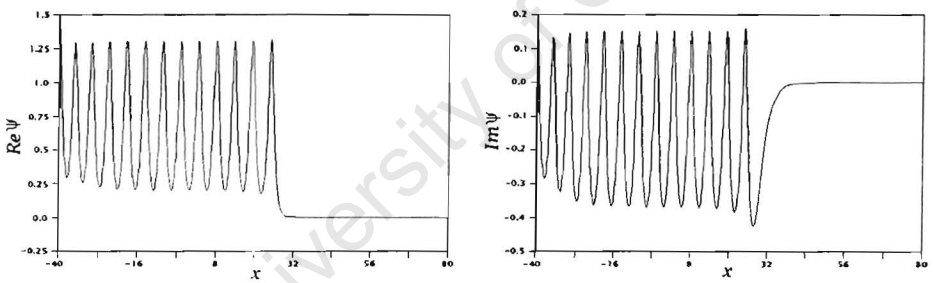

Figure 5.33: *Solution at point 9 in Figure 5.22. Here* $c = 0.263$, $\gamma = -0.016$ *and* $||\psi|| = 0.585$.

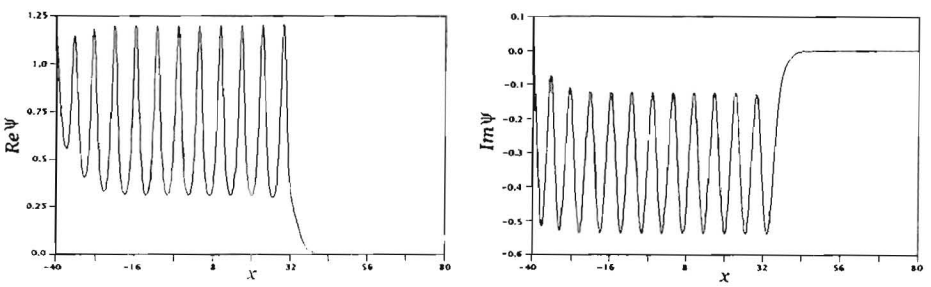

Figure 5.34: *Solution at point 10 in Figure 5.22. Here* $c = 0.100$, $\gamma = 0.418$ *and* $||\psi|| = 0.623$.

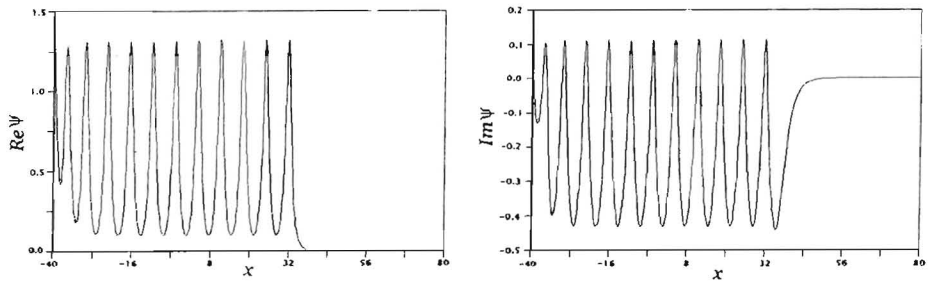

Figure 5.35: *Solution at point 11 in Figure 5.22. Here* $c = 0.200$, $\gamma = 0.040$ *and* $||\psi|| = 0.574$.

5.8 Stability analysis of the numerically obtained front solutions

We numerically tested the stability of the front solutions obtained by continuation in section 5.7. As in section 4.5 we tested the stability by adding a small perturbation of the form

$$\delta\psi(x,t) = [\delta u(x) + i\delta v(x)]\, e^{\lambda t}\,, \tag{5.41}$$

to a given solution ψ_s and linearising the CGLE in $\delta\psi$ to obtain an eigenvalue problem of the form

$$\mathcal{H}\begin{pmatrix} \delta u \\ \delta v \end{pmatrix} = \lambda J \begin{pmatrix} \delta u \\ \delta v \end{pmatrix}, \tag{5.42}$$

where $\mathcal{H}$ and J are as in equation (4.6).

In order to solve the eigenvalue problem numerically we expanded δu, u, δv in the Fourier series on the interval $[-40, 80]$ and truncated the series to a finite number of terms to convert the problem to one of finding the eigenvalues, λ, of a complex square matrix. The number of Fourier coefficients to which the series was truncated varied from 200 to 300 and was chosen to ensure that the numerical value obtained for the zero eigenvalue resulting from the translational invariance of the complex Ginzburg-Landau equation had a magnitude of less than 10^{-3}.

As mentioned previously, the graph of γ against c_- shown in Figure 5.24 divides the numerically obtained solution branch, found during the continuation, into two halves. When $c > c_-$, that is to the right of the graph of γ against c_-, the decay rate to the flat background ϕ_+ is positive (so decay to ϕ_+ is possible) and ϕ_+ is stable. When $c < c_-$, that is to the left of the graph of γ against c_-, decay to ϕ_+ is not possible and ϕ_+ is unstable. Note that although ϕ_+ is unstable when $c < c_-$, this does not allow us to predict that the front will be unstable when $c < c_-$ because in this region the front decays (on the left) to a oscillatory solution and not the flat background ϕ_+.

Despite the fact that for $c < c_-$ the front decays to an oscillatory background and not ϕ_+, the stability of the numerically obtained fronts presents a similar (but not identical) picture to that of the stability of the flat backgrounds.

For large c the numerically obtained fronts are found to be stable and the eigenvalue with largest real part (excluding the zero eigenvalue due to the translational invariance) is the eigenvalue from the continous spectrum of ϕ_+ with $k = 0$. The real part of this eigenvalue is less than zero for $c > c_-$ and may its value may be calculated for given c, γ and h using equation (4.7).

As we approach the maximum of the norm just to the right of point 7 in Figure 5.22 the continuous spectrum of ϕ_+ ceases to supply the eigenvalue with largest real part. As the maximum is passed the numerically obtained fronts become unstable as a single real eigenvalue crosses the imaginary axis. This real eigenvalue is not part of the spectrum of ϕ_+ since ϕ_+ is still stable. Neither is it part of the spectrum of the zero background since that is also stable. It seems most likely that the instability results from the oscillations about ϕ_+. The fronts remain unstable for the rest of the solution branch.

It is worthwhile noting that for some of the front solutions found we have $\gamma < 0$. Because, in our analysis of the stability of the flat backgrounds in chapter 4, we assumed that $\gamma \geq 0$, we must now extend that stability analysis to the case where $\gamma < 0$. In will only be necessary to extend the stability analysis for the $\phi = 0$ flat background. It can been seen from equations (4.7) and (4.8) that when $\gamma < 0$ and $h^2 < 1$, $\phi = 0$ is unstable against perturbations with $k = 0$. So, for the regions of the continuation where $\gamma < 0$ we have an instability in the flat background forming the right asymptote of the front solutions. Thus we expect the fronts in this region to be unstable and this is, indeed, the result obtained via the numerical stability analysis.

5.9 Summary

At the beginning of Chapter 5 we found an analytic kink solution to the driven undamped NLS equation. We then showed this kink solution could not be continued in the parameters γ or c separately, but only in both simultaneously. For small non-zero c and γ it was determined that a plot of γ against c should have a slope of $-\frac{1}{h}$. An asymptotic analysis of the behaviour of the first-order perturbations which would arise in such a continuation was performed. It was found that the real part of the perturbation would tend to a constant as $x \to \infty$ and minus the same constant as $x \to -\infty$ and that the imaginary part of the perturbation would become oscillatory as $x \to \pm\infty$. Consequently, the front would become a localised solution on a stationary oscillatory background, rather than on a flat background, as soon as c and γ were made non-zero. A numerical continuation of the kink to nonzero c and γ was performed with $h = 0.8$. The resulting solution branch formed a closed loop and a plot of γ against c did, indeed, have a slope of $-\frac{1}{h}$. The fronts obtained were over oscillatory backgrounds, as expected.

In section 5.5 we determined that the kink solution is also continuable to a solution moving with constant, non-zero velocity. The numerical continuation

to non-zero velocity was performed in section 5.6. Other solutions to the driven-undamped NLS equation were continued to solutions with non-zero velocity in [7]. Continuing the kink solution to non-zero velocity gave a branch of solutions which were initially kinks over oscillatory backgrounds, similar to those seen in the continuation to non-zero c and γ. However, after the background oscillations have become sufficiently large, a series of pulses were formed. The pulses in this series were identified as moving ψ_- pulses as they contributed only to the imaginary part of the solution and had a height similar to that of a ψ_- pulse. Near the end of the solution branch we encountered an almost stationary complex of two pulses on either side of small kink which is qualitatively similar to a complex of two twist solitons reported in [7]. However, as in [7], we fail to continue this complex to a stationary solution as the separation between the two pulses grows rapidly as the velocity tends to zero.

At the end of Chapter 5 we isolated one of the fronts making up the composite pulse found in during the continuation of ψ_+ in Chapter 4 and continued it in c and γ simultaneously. The stability of these continued fronts was then analysed. The value of h was fixed equal to 0.8 and initially c was 0.541 and γ was 0.5. Continuing towards larger c we found that the oscillations in the front about the non-zero flat background were damped out as c was increased. Continuing away from $c = 0.541$ to smaller c the magnitude of the oscillations increases until c becomes larger than a critical value, c_-, for which decay to the non-zero flat background becomes impossible. For c smaller than c_- the front becomes one which connects an oscillatory background to the zero background. The fronts connecting the non-zero flat background to the zero background are all found to be stable, except for some fronts close to the point where decay to the non-zero flat background becomes impossible. The fronts over the oscillatory background were found to be unstable.

Conclusion

The focus of this thesis was the obtaining of localised solutions of the parametrically driven CGLE through the continuation of known solutions from its parametrically-driven damped NLS limit and the examination of the stability of the obtained solutions.

After introducing and motivating our approach in the early part of the thesis we looked at two applications of the driven CGLE, namely optical parametric oscillators and ferromagnets. Optical parametric oscillators are an active topic of both theoretical and experimental research and have a number of important applications. Ferromagnets, although less of an active research topic, have been extensively studied and have important applications. The introduction then went on to briefly cover a series of theoretical topics all related to our work. The first of these topics was a comparison of the variational limits of the driven and undriven CGLEs. We saw that while localised stationary kinks and pulses are common in the variational limit of the *driven* CGLE they occur only for special values of the parameters of the *undriven* CGLE. Travelling fronts are, however, common in both cases. The second topic was the spatial forcing of a periodic pattern which adds an additional term, similar to that introduced by parametric driving, to the CGLE. The third topic was two interesting known solutions of the undriven CGLE. The two solutions were a composite pulse (consisting of two fronts bound to either side of a source of plane waves) and a moving pulse (consisting of a front bound to a non-composite pulse). They were introduced because they have a number of features in common with the composite pulse we obtained during our continuation of the soliton ψ_+ in chapter 4. We concluded that our composite pulse consisted of two bound fronts after further examination of the solution at the end of chapter 5. The final topic in the series was a known analytic solution of the damped-undriven NLS equation. This known solution is a possible starting point for further continuations which might extend our study of the NLS limit of the driven and undriven CGLEs.

For the duration of chapter 2 we turned our attention to the Faraday resonance experiment. A brief description of the experimental setup and the history of the experiment was followed by a derivation of the equations governing the surface of the periodically driven fluid. Starting from Euler's equation for an incompressible fluid with neglibile velocity we derived the necessary equations for the fluid surface and the velocity potential. The derived equations were then linearised

and the boundary conditions discussed. The last section of chapter 2 was spent discussing the linearised equations. The linear partial differential equations obtained earlier were reduced to a Floquet problem and the long time behaviour of its solutions was found to depend only on the eigenvalues of a constant matrix.

We next turned to look, in chapter 3, at the manner in which the driven and undriven complex Ginzburg-Landay equations arise as amplitude equations for the excited modes of a nonlinear system near a Hopf bifurcation of a solution of that system. When dealing with the undriven system we made use of the symmetries of the system to motivate the construction of amplitude equation. The important symmetries were the translations of the space and time variables. The amplitude of the excited modes was also allowed to vary slowly in space, which introduced spatial derivatives into the amplitude equation. In the examination of the driven system we saw that a different set of symmetries resulted in a modified amplitude equation. The symmetry broken by the parametric driving is that of time translation. Instead of this broken symmetry, the system now has a discrete symmetry - time periodicity. The dimension of the critical subspace (the number of excited modes) at the Hopf bifurcation is important. The Hopf bifurcation has two linearly independent excited modes which allows additional dynamics to enter the amplitude equation. In the case of the saddle node bifurcation, at which only one mode becomes critical, the amplitude equation is the same whether the system is periodically forced or not.

In Chapter 4 we showed that the known pulse solutions to the driven damped NLS equation, ψ_+ and ψ_-, found in [52] could be continued to the driven CGLE and performed this continuation by varying the filtering parameter, c. In order to better understand the results of this numerical continuation, we performed an adiabatic analysis of the ψ_+ and ψ_- solutions (valid when $|c| \ll 1$) and examined the stability of the flat background solutions of the driven CGLE. We also found the parameter regions where decay to each of the flat backgrounds is possible. Only in these regions can localised solutions exist on the flat backgrounds. The results of the adiabatic analysis showed that the solutions obtained through the continuation of ψ_+ should be stable when $c > 0$, at least for small c. In addition, the adiabatic analysis predicted that, for small c, the continuation of ψ_- would yield only unstable solutions. These predictions agreed with the numerical results. The numerical continuation of ψ_+ obtained the previously known triple pulse solution found (also numerically) in [55] and gave rise to an interesting composite pulse solution similar to those found in [36]. Continuing ψ_+ towards negative c yielded a branch of unstable solutions which turned back towards the $c = 0$ axis. At this turning point the solutions became triple-humped and began to resemble the triple pulse $\psi_{(-+-)}$. Upon reaching $c = 0$ the solution $\psi_{(-+-)}$ was obtained. Continuing this branch across into the $c > 0$ region did not result in the solutions gaining stability but a series of turning points each added a hump to the center of the triple-pulse resulting, eventually, in a central composite pulse with a lateral pulse

on each side. The continuation of ψ_+ towards positive c gave a branch of solution which were stable until the branch turned back towards the $c = 0$ axis. At this turning point the solutions became double-humped. Without reaching the $c = 0$ axis the branch then passed through a series of turning points. As with the earlier branch (obtained by continuing $\psi_{(-+-)}$ towards postive c), each of these turning points contributed an additional hump to the centre of the pulse, resulting in the formation of a composite hump, similar that obtained on the earlier branch, but without the lateral humps. The stability of this new composite pulse without lateral humps was found to alternate at each of the turning points as the result of a single real eigenvalue repeatedly crossing the imaginary axis. The continuation of ψ_- showed the broadening of the pulse solution as c was increased from zero and the splitting of the pulse into a double-humped solution was c was decreased. Decreasing c further resulted in the broadening of the double-humped solution. This broadening of the solution was expected from our earlier analysis of the large c limit of the driven CGLE. No turning points were found and the solutions remained unstable all the way along the solution branch.

The adiabatic analysis of the ψ_+ and ψ_- solution branches for small c had suggested that they should merge in a saddle-node bifurcation for finite c. Although the adiabatic analysis was not expected to accurately predict even such qualitative behaviour for non-small c, we were nevertheless puzzled by the discrepancy. The adiabatic analysis did predict that for h close to γ the ψ_- and ψ_+ branches would merge when $c \ll 1$. By continuing solutions from the ψ_- branch towards smaller h, the saddle-node bifurcation point was located and continuing further (now towards larger h) the ψ_+ branch was re-obtained. The critical value of h at which the bifurcation occurs, $h_{cr}(c, \gamma)$ was found to drop below the value predicted by the adiabatic analysis as c was increased. Our original continuations in c (with $h = 0.8$ and $\gamma = 0.5$) did not encountered this bifurcation since for $\gamma = 0.5$, the maximum value of h_{cr} is approximately 0.660.

In Chapter 5, the final chapter, we studied fronts. At the beginning of the chapter we introduced an analytic kink solution of the driven undamped NLS equation. This kink could not be continued in c or γ separately, but was continued into the two simultaneously. The continuation of the kink in c and γ gave rise to kink solutions of the driven CGLE which connected oscillatory backgrounds, as was expected from the asymptotic analysis of the first-order perturbations arising in the continuation. A plot of γ against c obtained during the continuation did indeed have a slope of $-\frac{1}{h}$ near the origin as was predicted by the continuability condition derived earlier. We then turned to examine the possiblity of continuing the kink to a solution moving with non-zero velocity, as was done for other solutions of the driven undamped NLS equation by the authors of [7]. This yielded moving kinks over oscillatory backgrounds. In this case the oscillatory backgrounds represent plane travelling waves with the same velocity as the front. Continuing further along the branch of solutions, the oscillatory background eventually became a

series of ψ_- pulses and finally an almost stationary solution consisting of a pulse on either side of a small kink, which was similar to a complex of two twist solitons found in [7]. This solution could not be continued to a stationary solution since the separation distance between the two pulses appears to go to infinity as the velocity goes to zero.

In the latter part of chapter 5 we took the multi-humped composite pulse solution obtained by continuing ψ_+ and separated out the right-hand front. We did this by taking the right-half of the pulse and adding a section of the flat background ϕ_+ to the left of it. We continued this constructed front in c and γ simultaneously. Increasing c from its initial value resulted in a branch of stable fronts connecting ϕ_+ and $\psi = 0$. These stable fronts displayed fewer oscillations near the ϕ_+ background as c was increased. Upon decreasing c from its initial value, we found that the oscillations in the front about the ϕ_+ background increased. As c was decreased further, the fronts along this branch became unstable and soon afterwards, decay to ϕ_+ became impossible and the fronts became solutions over an oscillatory background on the left and the zero background on the right.

One possible extension of our work in chapters 4 and 5 would be to repeat everything we have done for a larger region of the parameter space. A meaningful exploration of the parameter space would take significantly more computing power than I had available. Some of the continuations performed took a couple of hours on my desktop machine and the stability analysis of solutions found in Chapter 4 about two days to run. Nevertheless, such an exploration should be feasible.

Another possibility for extending our work is to continue the solution to the zero driving limit of (4.1) which was found in [39] and mentioned in section 1.4.4 of the introduction. The first step would be check analytically that such a continuation is possible.

A third possible extension is suggested by the work of Cruz-Pacheco and Luce in [59]. These authors have used the Melnikov method to study solitary waves solutions of the undriven CGLE near its NLS limit. It might be possible to adapt these methods to the driven CGLE.

Bibliography

[1] V. L. Ginzburg and L. D. Landau, Zh. Eksp. Teor. Fiz. 20 (1950) p. 1064

[2] H. B. Nielsen and P. Olesen, Nucl. Phys. B, 61 (1973) p. 45

[3] V. E. Zakharov and A. B. Shabat, Sov. Phys. J.E.T.P. 34 (1972) p. 62

[4] P. D. Lax, Comm. Pure Appl. Math. 21 (1968) p. 467

[5] C. S. Gardner, J. M. Greene, M. D. Kruskal and R. M. Miura, Phys. Rev. Lett. 19 (1967) p. 1095

[6] E. J. Doedel, X. J. Wang and T. F. Fairgrieve, *AUTO 94: Software for continuation and bifurcation in ordinary differential equations*, Applied Mathematics Reports, California Institute of Technology

[7] I. V. Barashenkov, E. V. Zemlyanaya and M. Bär, Phys. Rev. E 64 (2001)

[8] M. Faraday, Philos. Trans. R. Soc. London 121 (1831) p. 299

[9] W. van Saarloos and P. C. Hohenberg, Physica D 56 (1992) p. 303

[10] Chapter entitled *Solitons of the CGLE* by N. Akhmediev and A. Ankiewicz in *Spatial Solitons*, edited by S. Trillo and W.E. Torruellas, 1st Edition (Springer, Berlin) 2001, p. 311

[11] M. C. Cross and P. C. Hohenberg, Rev. Mod. Phys. 65 (1993) p. 851

[12] C. Elphick and E. Meron, Phys. Rev. A 40 (1989) p. 3226

[13] J. Wu, R. Keolian and I Rudnick, Phys. Rev. Lett. 52 (1984) p. 1421

[14] J. Larraza and S. Putterman, J. Fluid Mech. 148 (1984) p. 443

[15] J. W. Miles, J. Fluid Mech., 148 (1984) p. 451

[16] S. Douady, J. Fluid Mech., 221 (1990) p. 383

[17] A. Meccozzi, J.D. Moores, H.A. Haus and Y. Lai, Opt. Letters 16 (1991) p. 1841

[18] K. Stewartson and J T. Stuart, J. Fluid Mech. 48 (1971) p. 529

[19] P. Kolodner, D. Bensimon and C.M. Surko, Phys. Rev. Lett. 60 (1988) p. 1723

[20] EKSPLA Ltd., http://www.ekspla.com/, Savanoriu Av. 231, LT-2028 Vilnius, Lithuania

[21] K. Staliunas, Phys. Rev. Lett. 81 (1998) p. 81

[22] S. Longhi and A. Geraci, Phys. Rev. A 54 (1996) p. 4581

[23] S. Longhi, J. Mod. Opt. 43 (1996) p. 1089

[24] S. Trillo, M. Haelterman and A. Sheppard, Optics Lett. 22 (1997) p. 970

[25] G-L. Oppo, A. J. Scroggie and W. J. Firth, Phys. Rev. E 63 (2001)

[26] S. Longhi, Phys. Rev. E 53 (1996) p. 5520

[27] D. E. Pelinovsky, Yu. A. Stepanyants and Yu. S. Kivshar, Phys. Rev. E 51 (1995) p. 5016

[28] Electrodynamics of Continuous Media, Landau and Lifshitz Course of Theoretical Physics, 2nd edition (Pergamon Press, London) 1984, Chapter 5

[29] P. Coullet, J. Lega and Y. Pomeau, Europhys. Lett. 15 (1991) p. 211

[30] Y. Pomeau, Physica D 23 (1986) p. 3

[31] O. Thual and S. Fauve, J. Phys. France 49 (1988) p. 1829

[32] D. V. Skryabin, A. Yulin, D. Michaelis, W. J. Firth, G.-L. Oppo, U. Peschel and F. Lederer, Phys. Rev. E 64 (2001)

[33] P. Coullet, Phys. Rev. Lett. 56 (1986) p. 724

[34] O. M. Braun and Y. S. Kivshar, Phys. Rep. 306 (1998)

[35] M. Lowe and J. Gollub, Phys. Rev. A 31 (1985) p. 3893

[36] V.V. Afanasjev, N. Akmediev and J.M Soto-Crespo, Phys. Rev. E 53 (1996) p. 1931-1939

[37] J. D. Moores, Opt. Commun. 96 (1993) p. 65

[38] W. van Saarloos and P. C. Hohenberg, Phys. Rev. Lett. 64 (1990) p. 749

[39] N. R. Pereira and L. Stenflo, Physics of Fluids 20 (1977) p. 1733

[40] N. R. Pereira, Physics of Fluids 20 (1977) p. 1735

[41] T.B. Benjamin and F. Ursell, Proc. Roy. Soc. London, Ser. A 225 (1954) p. 505

[42] E. Meron and I Procaccia, Phys. Rev. A 34 (1986) p. 3221

[43] L. Matthiessen, Ann. Phys. (Leipzig) 134 (1868) p. 107

[44] L. Matthiessen, Ann. Phys. (Leipzig) 141 (1870) p. 375

[45] Lord Rayleigh, Philos. Mag. 16 (1883) p. 50

[46] Lord Rayleigh, Philos. Mag. 15 (1883) p. 235

[47] D. Astruc and S. Fauve, IUTAM Symposium on Free Surface Flows (2001) p. 39

[48] L. D. Landau and E. M. Lifshitz, Fluid Mechanics, Pergamon Press, p. 16

[49] L. D. Landau and E. M. Lifshitz, Fluid Mechanics, Pergamon Press, p. 230

[50] H. Mori and Y. Kuramoto, Dissipative Structures and Chaos, Springer, Chapter 2

[51] C. Elphick, G. Iooss and E. Tirapegui, Phys. Lett. A 120 (1987) p. 459

[52] I. V. Barashenkov, M. M. Bogdan, V. I. Korobov, Europhys. Lett. 15 (1991) p. 113

[53] E. Doedel, H. B. Keller and J. P. Kernevez. Int. J. Bifurcation and Chaos 1 (1991) p. 493

[54] E. Doedel, H. B. Keller and J. P. Kernevez, Int. J. Bifurcation and Chaos 1 (1991) p. 745

[55] I. V. Barashenkov and E. V. Zemlyanaya, Phys. Rev. Lett. 83 (1999) p. 2568

[56] P. Coullet, J. Lega, B. Houchmanzadeh and J. Lajzerowicz, Phys. Rev. Lett. 65 (1990) p. 1352

[57] C. Elphick, A. Hagberg, B.A. Malomed and E. Meron, Phys. Lett. A (1997) p. 33

[58] I.V. Barashenkov, E.V. Zemlyanaya and M. Bär, report nlin.PS/0010008 (unpublished)

[59] G. Cruz-Pacheco and B. P. Luce, Phys. Lett. A 236 (1997) p. 391